Control of Radiated Noise from Fluid-Loaded Stiffened Structures

by

Daniel Martins

under the supervision of

Dr. Mahmoud Karimi (principal supervisor)
A/Prof. Laurent Maxit (co-supervisor)
Prof. Ray Kirby (co-supervisor)

A thesis submitted in total fulfillment for the degree of Doctor of Philosophy

in the
Centre for Audio, Acoustics and Vibration
School of Mechanical and Mechatronic Engineering
Faculty of Engineering and Information Technology
The University of Technology Sydney

Submission date: 23 October 2024

Certificate of Original Authorship

I, Daniel Martins, declare that this thesis is submitted in fulfilment of the requirements for the award of Doctor of Philosophy (C02018), in the School of Mechanical and Mechatronic Engineering at the University of Technology Sydney.

This thesis is wholly my own work unless otherwise referenced or acknowledged. In addition, I certify that all information sources and literature used are indicated in the thesis.

This document has not been submitted for qualifications at any other academic institution.

This research is supported by the Australian Government Research Training Program.

Signed: Production Note:
Signature removed prior to publication.

Date: 18/10/2024

Abstract

Periodically stiffened structures are widely used in many engineering applications, including aeronautics, marine, and rail systems. In these structures, so called Bloch-Floquet (BF) waves are generated due to the interaction between flexural waves in the host structure and flexural/torsional waves in the stiffeners. These waves are a primary source of undesirable noise and vibrations when a stiffened structure is excited by a force. Hence, this work aims to understand the propagation of BF waves and their contribution to the radiated sound power by utilising non-negative intensity (NNI) technique. Additionally, a passive control technique based on the acoustic black holes (ABHs) is developed to control vibroacoustic responses of fluid-loaded stiffened plates. This has been achieved by incorporating ABHs into stiffeners and by analysing their effects on the propagation of BF waves.

An analytical model is used to evaluate the vibroacoustic responses of a three-dimensional fluid-loaded infinite stiffened plate subjected to point force excitation. This model, is formulated in the wavenumber domain, allowing efficient simulations. The NNI, which is also expressed in the wavenumber domain, has been derived, and NNI maps show that when the excitation frequency is within a radiating BF passband, the intensity is concentrated at the stiffener's position. Further, the research explores the integration of ABHs as stiffeners in the fluid-loaded infinite plate while maintaining the host structure's integrity, to mitigate the propagation of BF waves. A semi-analytical model in the wavenumber domain is developed to predict the forced vibroacoustic response of a two-dimensional fluid-loaded infinite plate with ABH stiffeners. This model incorporates the translational and rotational dynamic stiffnesses of the stiffeners, estimated using the Finite element method, and couples these with the fluid-loaded plate's analytical formulation. The results indicate substantial reductions in mean quadratic velocity and radiated sound power when using ABH stiffeners.

Finally, an experimental study compares the vibrational response of two finite stiffened beams with ABH and rectangular stiffeners, providing empirical data to confirm the effectiveness of the proposed passive control method and the theoretical and numerical findings in practice for the case in air. The damping effect caused by the addition of damping layers is compared for both stiffeners, considering the stiffeners without damping layers, with viscoelastic damping layers and constrained viscoelastic damping layers. The combined analytical, numerical, and experimental approaches underscore the potential of ABH stiffeners to mitigate the vibroacoustic response in stiffened structures.

List of Publications

Most of the work presented in this thesis has been published or submitted for publication in journals and conference proceedings. The following list of articles includes works that have been completed during the timeframe of the thesis:

Journal publications

1. **Daniel Martins**, Mahmoud Karimi, Laurent Maxit, and Ray Kirby. "Non-negative intensity for a heavy fluid-loaded stiffened plate". In: *Journal of Sound and Vibration* 566. 2023

2. **Daniel Martins**, Mahmoud Karimi, and Laurent Maxit. "Semi-analytical formulation to predict the vibroacoustic response of a fluid-loaded plate with ABH stiffeners". In: *Thin-Walled Structures* 112539. 2024.

3. **Daniel Martins**, Mahmoud Karimi, and Laurent Maxit. "Vibration Analysis of Beams Coupled with Evenly Spaced Acoustic Black Hole Pillars: Experimental and Numerical Insights". In: *Mechanical Systems and Signal Processing* (Under review).

Peer-reviewed Conference proceedings

1. **Daniel Martins**, Mahmoud Karimi, and Laurent Maxit. "Vibroacoustic response of a heavy fluid loaded plate with ABH stiffeners". In: *Acoustics 2023 Sydney.* Sydney, Australia, 4-8 December, 2023.

2. **Daniel Martins**, Mahmoud Karimi, and Laurent Maxit. "Vibroacoustic response of a heavy fluid loaded plate with ABH stiffeners". In: *Journal of Physics: Conference Series.* Accepted (2024). Presented in: *RASD 2024 (XIVth International Conference on Recent Advances in Structural Dynamics).* Southampton, United Kingdom, 1-3 July, 2024.

3. **Daniel Martins**, Mahmoud Karimi, and Laurent Maxit. "Experimental vibration analysis of a beam with ABH stiffeners". In: *Acoustics 2024.* Gold Coast, Australia, 6-8 November, 2024.

Acknowledgements

This work was completed during a time of significant challenges, including the global pandemic, the early days of my marriage, and a major transition to a new country. In light of these experiences, I would like to take a moment to express my heartfelt gratitude to those who have shaped both my research and personal growth along the way. I am especially grateful to God for placing these remarkable people in my life, whose support and guidance have helped me reach this point in my journey.

I would like to express my deepest gratitude to my primary supervisor, Dr. Mahmoud Karimi, whose expertise, guidance, and consistent encouragement have been invaluable throughout my research journey. His profound insights and constructive feedback were instrumental in shaping the direction and quality of this work. I am immensely grateful for his unwavering support and mentorship. I also greatly appreciate his efforts in fostering a collaborative and supportive environment, frequently bringing the team together to celebrate each achievement along the way. I extend my heartfelt thanks to A/Prof. Laurent Maxit for his thoughtful advice and assistance during the progression of this thesis. His critical perspectives and specialised knowledge have significantly enhanced the depth of my research.

I would like to extend special thanks to my colleagues and the research team at CAAV, particularly Jamie Kha, Hesam Abtahi, Huong Cao, and Paul Williams, for their invaluable discussions, moral support, and shared expertise throughout the development of this thesis. Their camaraderie has made this journey not only productive but also enjoyable.

I am deeply grateful to my wife, Ana, for her unwavering encouragement and patience, which kept me motivated and focused during the most challenging times. Her love and support ensured that I maintained the focus necessary for such an extensive research project, while also reminding me of the importance of life beyond work. I also extend my thanks to my parents and friends, whose support provided the perfect balance between work and leisure, helping me maintain perspective throughout this journey.

Finally, I would like to acknowledge the authors of the significant works that laid the foundation for this research. Their pioneering contributions in the field of vibroacoustics have inspired much of the work presented here.

Contents

List of Figures

List of Tables

Abbreviations

2D	**T**wo-**D**imensional
3D	**T**hree-**D**imensional
ACLD	**A**ctive **C**onstrained **L**ayer **D**amping
ABH	**A**coustic **B**lack **H**ole
B&K	**B**rüel & **K**jær
BEM	**B**oundary **E**lement **M**ethod
BF	**B**loch-**F**loquet
CAA	**C**ircunferential **A**dmittance **A**pproach
CTF	**C**ondensed **T**ransfer **F**unction
CVL	**C**onstrained **V**iscoelastic **L**ayer
DAF	**D**ifuse **A**coustic **F**ield
DAQ	**D**ata **A**c**Q**uisition
DVA	**D**ynamic **V**ibration **A**bsorber
FE	**F**inite **E**lement
FEM	**F**inite **E**lement **M**ethod
FFT	**F**ast **F**ourier **T**ransform
FRF	**F**requency **R**esponse **F**unction
GEM	**G**aussian **E**xpansion **M**ethod
GENAH	**GE**neralized **N**ear-field **A**coustic **H**olography
IDFT	**I**nverse **D**iscrete **F**ourier **T**ransform
IFFT	**I**nverse **F**ast **F**ourier **T**ransform
NAH	**N**ear-field **A**coustic **H**olography
NNI	**N**on-**N**egative **I**ntensity
PML	**P**erfect **M**atched **L**ayer
RBD	**R**esonant **B**eam **D**amper

SSI	**S**uper**S**onic **Intensity**
SVD	**S**ingle **V**alue **D**ecomposition
TBL	**T**urbulent **B**oundary **L**ayer
UTS	**U**niversity of **T**echnology **S**ydney
VL	**V**iscoelastic **L**ayer
WGA	**W**aveguide **A**bsorber

Symbols

A_s	cross section area of the stiffener
c_f	sound speed in the fluid
d	distance between stiffeners
D	flexural rigidity of the plate
e	exponential function
E	Young's modulus
E_s	Young's modulus of the stiffeners
F_0	point force
$f_\mathrm{cut\text{-}on}$	cut-on frequency of the ABH
F_s	force distributions related to the interaction between the plate and the n^th stiffener
FL	fluid loading contribution
G_s	Coulomb's modulus of the stiffeners
h	thickness
I_0	stiffener's moment of inertia in relation to the contact point
I_x	stiffener's moment of inertia along the x-axis
I_y	stiffener's moment of inertia along the y-axis
I_V^N	NNI in terms of velocity
I_P^N	NNI in terms of pressure
j	imaginary unit
J_s	torsion constant
k_f	acoustic wavenumber
k_x	wavenumber in the direction x
k_y	wavenumber in the direction y
$\mathbf{k}$	vector of wavenumbers
L	length

M_{s}	moment distributions related to the interaction between the plate and the n^{th} stiffener
n	stiffener number
O_{s}	3D torsional dynamic stiffness
p	wall pressure due to the fluid loading
$\widetilde{P_0}$	spectral displacement of the plate without the stiffeners
$\widetilde{P}$	spectral displacement of the plate with the stiffeners
t	time
$\mathrm{T_n}$	transmissibility in relation to the n stiffener
T_{s}	torsional dynamic stiffeness of the stiffener
v	plate's velocity
$\widetilde{V}$	spectral velocity of the plate
w_n	displacement of the plate at the n^{th}stiffener
W_{s}	displacement of the stiffener
$\widetilde{W_0}$	spectral displacement of the plate without the stiffeners
$\widetilde{W}$	spectral displacement of the plate with stiffeners
x_0	excitation position
(x, y, z)	rectangular or Cartesian coordinates
Z	fluid-loaded plate dynamic stiffeness
Z_{s}	flexural dynamic stiffeness of the stiffener
Γ	stiffeners effect on the plate vibrations
δ	Dirac delta function
ϵ	tolerance
η	loss factor
θ	rotation of the stiffener
ν	Poisson's ratio
Π_P	sound power in terms of pressure
Π_V	sound power in terms of velocity
Π_L	sound power considering a finite length L
ρ_{f}	density of the fluid
ρ_{p}	density of the plate
ρ_{s}	density of the stiffeners
ω	excitation frequency

Ω_a	acoustic circle
Ω_f	half space occupied by the fluid
*	complex conjugate
∇	Nabla operator
$\mathbb{Z}$	integer

Chapter 1

Introduction

1.1 Research Motivation

The vibroacoustic analysis of periodically stiffened structures is essential for various engineering applications. It is known that with the introduction of periodically spaced stiffeners into the structure, Bloch-Floquet (BF) waves are generated due to the interaction of the flexural waves of the host structure with the flexural/torsional waves of the stiffeners. If these stiffeners are periodically spaced, the wave interaction will produce predictable passbands associated with higher vibration levels [15]. It has been reported in the literature that the radiating BF passbands are related to undesirable noise in the far-field [65, 68]. Understanding and mitigating the impact of BF waves is crucial for improving the performance and durability of stiffened structures. Consequently, there is a need to develop solutions that effectively reduce the adverse effects of the propagation and radiation of BF waves while preserving the structural integrity and maintaining the static stiffness of the system, ensuring that the host structure's is not compromised.

1.1.1 Aims and Objectives

The primary aim of this thesis is to extend the understanding of BF wave generation and propagation in fluid-loaded periodically stiffened plates, and their radiation to the far field. Additionally, this research aims to mitigate the vibroacoustic response of these structures.

Objectives:

- Analytically study the vibroacoustic behaviour of the fluid-loaded stiffened plate to predict and understand the vibroacoustic behaviour of periodically stiffened plates. Utilising NNI maps, identify the regions on the vibrating plate that most contribute to radiated sound power, offering deeper insights into BF wave propagation and interaction mechanisms. The proposed analytical model aim to provide efficient and broad-frequency range analysis, overcoming the limitations of the acoustic intensity.

- Develop a semi-analytical model for fluid-loaded plates with ABH stiffeners. This novel approach combines the dynamic stiffness of the stiffeners, obtained using FEM, with analytical modelling for the heavy fluid-loaded plate, resulting in enhanced computational efficiency and broad-frequency range analysis.

- Analyse the effect of ABH stiffeners on noise and vibration mitigation from a fluid-loaded stiffened plate under force excitation. Evaluating the effectiveness of ABHs using FEM simulations and developed semi-analytical model.

- Demonstrate the effectiveness of ABH stiffeners through experiments. Confirm the effectiveness of the passive control approach by conducting experiments using a finite beam with ABH stiffeners. The empirical data support the theoretical and numerical findings, ensuring that the proposed approaches are both practical and effective.

1.2 Thesis overview

The remainder of the thesis is structured in the following manner:

Chapter 2: Literature Review

This chapter provides an extensive review of the existing literature on the vibroacoustic behaviour of stiffened structures and various methods to identify and control these responses. It begins by exploring the vibroacoustic characteristics of stiffened structures, dividing the discussion into plate-like and cylinder-like structures. The focus then shifts

to methods for identifying surface contributions to the radiated sound power, with detailed consideration of near-field acoustic holography and intensity-based methods, such as supersonic acoustic intensity and non-negative intensity techniques. The chapter concludes by examining control methods for vibroacoustic responses, emphasising acoustic black holes (ABHs), and distinguishing between embedded ABHs and those designed as attached vibration dampers.

Chapter 3: Non-negative intensity for a heavy fluid-loaded stiffened plate

This chapter details the use of the NNI to analyse a three-dimensional (3D) heavy fluid-loaded stiffened plate subjected to a point force. An analytical model is developed in the wavenumber domain to facilitate efficient simulations of vibroacoustic responses and NNI maps. The study investigates the impact of Bloch–Floquet waves, particularly their role in creating passbands and stopbands, on the vibroacoustic behaviour of the plate. Through a detailed parametric study, the chapter compares the responses of both stiffened and unstiffened structures under different excitations positions. Key findings highlight the effects of different excitation locations, material damping, and the interactions between the plate and stiffeners. The insights gained from this analysis contribute to a deeper understanding of acoustic radiation in stiffened structures, showing that the acoustic energy is dispersed in the normal direction to the stiffeners within the BF radiating bands.

Chapter 4: Semi-analytical formulation for vibroacoustic response of a heavy fluid-loaded plate with ABH stiffeners

This chapter presents a semi-analytical model for predicting the vibroacoustic response of a heavy fluid-loaded plate with ABH stiffeners. The model is developed in the wavenumber domain to facilitate efficient computation of the system's response, integrating translational and rotational dynamic stiffnesses of the stiffeners obtained via FEM simulations. These dynamic properties are coupled with the analytical formulation of the fluid-loaded plate to accurately predict spectral displacement and radiated pressure. The effectiveness of ABH stiffeners in mitigating vibroacoustic responses, compared to conventional rectangular stiffeners, is examined through parametric study. This includes the impact of damping layers, stiffener spacing, and frequency range on the system's behaviour. The study also investigates the influence of BF waves in creating passbands and stopbands, and how ABH stiffeners can reduce these effects. Verification through

FEM simulations in COMSOL Multiphysics™ demonstrates the model's accuracy and computational efficiency. Key findings show significant reductions in mean quadratic velocity and radiated sound power using ABH stiffeners, particularly within identified passbands, highlighting their potential for noise reduction in fluid-loaded plates.

Chapter 5: Experimental and numerical analysis of a finite beam with ABH stiffeners

This chapter presents the experimental analysis of two finite stiffened beams, with rectangular stiffeners and with ABH stiffeners. The ABH stiffeners are designed to have the same area and moment of inertia at the contact point with the beam, resulting in the same mass and static stiffness. The two stiffened beams were suspended by strings at each end to mimic a free-free boundary condition. An impact force is applied at two different positions, on the stiffener and in between two stiffeners. Three different cases are considered for the two excitation points. Stiffeners without damping layers, with viscoelastic layers and with constrained viscoelastic layers. The addition of damping to both systems is analysed, and the results show that damping is more effective in the beam with ABH stiffeners than in the beam with rectangular stiffeners. The comparison of the vibrational responses of both stiffened beams shows that replacing traditional rectangular stiffeners with ABH stiffeners can lead to lower vibration levels.

1.3 Contribution to research

The main contributions of this thesis include the following:

1. The understanding of the vibroacoustic behaviour in periodically stiffened plates subjected to heavy fluid loading is extended, by analysing the generation and propagation of BF waves using NNI. An analytical model of the NNI in the wavenumber domain is proposed. The analytical approach enables fast and efficient calculations of the vibroacoustic responses and NNI maps. The methodology allows for the identification and analysis of BF waves, showing their significant contribution to radiated sound power within its passbands. Parametric studies compare the effects of different excitation positions and frequencies, providing insights into energy distribution and radiation efficiency. Additionally, the influence of structural damping on the acoustic energy distribution is explored using NNI, demonstrating

that increased damping reduces both NNI and sound power primarily in passbands. By employing NNI maps, critical surface regions contributing to radiated sound power are identified, offering clear visualisations of localised sound radiation areas, particularly in the presence of BF waves. The comparative analysis of stiffened and unstiffened plates further elucidates the impact of stiffeners on vibroacoustic behaviour, contributing to the broader understanding and potential applications of NNI in complex stiffened structures.

2. A semi-analytical model is developed, combining analytical and numerical methods to predict the vibroacoustic response of a heavy fluid-loaded plate with ABH stiffeners. The model considers the dynamic stiffnesses of the stiffeners using FEM, which are then integrated into the analytical expressions for the fluid-loaded stiffened plate, which are formulated directly in the wavenumber domain. This approach enhances computational efficiency compared to FEM and allows altering the stiffener shapes with ease, since the dynamic stiffnesses is obtained using a single stiffener.

3. To mitigate vibrations and radiated noise, it is proposed to replace conventional rectangular stiffeners with ABH stiffeners in a heavy fluid-loaded infinite stiffened plate. The stiffeners are designed with the same cross-sectional area and moment of inertia at the contact point, which leads to the the same mass and static stiffness ensuring a "fair" comparison. It is demonstrated that ABH stiffeners can significantly reduce the vibroacoustic response of the plate compared to conventional stiffeners.

4. An experimental study is made on two finite stiffened beams with rectangular stiffeners ABH stiffeners. The addition of traditional viscoelastic layer damping and constrained viscoelastic layer damping on the stiffeners are compared in terms of the vibrational response of the beam. The study provides a comprehensive comparison of the effectiveness of these configurations against traditional rectangular stiffeners in mitigating vibration. The findings underscore the potential advantages of ABH stiffeners as a replacement for rectangular stiffeners for passive vibration control of stiffened structures.

Chapter 2

Literature Review

This literature review is divided into three primary sections, each addressing a crucial aspect of vibroacoustic research on stiffened structures. The first section (2.1) explores the vibroacoustic responses of stiffened structures, starting with plate-like structures (2.1.1) and moving on to cylinder-like structures (2.1.2). This section covers significant advancements in modeling these structures under various excitations, both deterministic and stochastic.

The second section (2.2) focuses on methods for identifying surface contributions to the acoustic radiation and vibrational energy. This includes near-field acoustic holography (2.2.1) and various intensity-based methods, such as supersonic acoustic intensity (2.2.2.1) and non-negative intensity (2.2.2.2). These methods are essential for accurately determining how different surface components contribute to the overall sound power.

The third section (2.3) reviews techniques for controlling vibroacoustic responses. It begins with a brief introduction on passive and active control strategies, followed by the innovative use of ABHs (2.3.1). This part is further divided into discussions on embedded ABHs (2.3.1.1) and those used as attached vibration dampers (2.3.1.2). The effectiveness of ABHs in mitigating noise and vibrations is critically evaluated. This comprehensive review identifies gaps in the current research and suggests future directions, particularly the potential of ABHs as attached vibration dampers in fluid-loaded systems.

2.1 Vibroacoustic responses of stiffened structures

The work by Brillouin [6] is among the earliest studies on periodic structures. He investigated wave propagation in periodic media, drawing analogies between electrical and mechanical systems, and demonstrated the potential for band-pass filters in periodic mechanical systems. The characteristics of such systems enable them to function as mechanical wave filters, by creating passbands and stopbands of wave propagation [3]. A comprehensive review of early works on periodic structures can be found in Ref. [72].

Periodic structures have been extensively studied and utilised in various engineering applications, including aircraft fuselages, trains, and marine vessels. Examples of aircraft fuselage section models are presented in Fig. 2.1, illustrating the use of stiffeners in various practical applications. The prediction and analysis of structural vibration and structure-borne sound are crucial for these systems. Many of these applications are stiffened structures, leading to studies that mimic real-world conditions with different geometries and boundary conditions. Here works on periodic structures are divided into two categories, plate-like and cylinder-like structures.

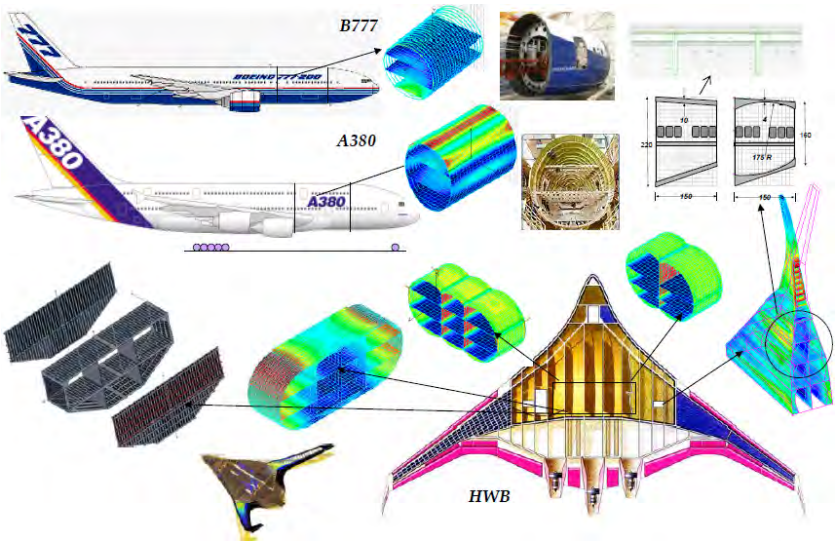

FIGURE 2.1: Aircraft fuselage section models with periodic stiffeners. From Fig. 5 in Ref. [83].

2.1.1 Plate-like structures

One of the first investigations on plate-like stiffened structures was carried out by Mead [76] who considered an infinite beam with periodic supports and analysed the

free wave propagation based on a space-harmonic approach, for the system subjected to a harmonic point force excitation. He derived expressions for the flexural propagation constants, and showed that the wave propagation was affected by the reflections that occur at the supports, and also near-field effects in the wave displacement. It was shown that for the system with rigid supports, the wave propagation only occurs in certain frequency bands and there is a high decay of energy moving away from the source. Following this work, Mead and Pujara [75] investigated the accuracy of the same method by varying the number of terms in the space-harmonic series, and finding the number of terms required for a converged solution, they also computed the displacement of the beam subjected to a random pressure field. Rumerman [91] presented the formalism to examine wave propagation in periodically stiffened infinite plates upon force excitations, the plate was subjected to an external distributed force. It was assumed that the stiffeners are line attachments to the plate, so the force applied on the stiffeners will be considered line forces and line moments upon the plate. He characterised the plate flexural properties and stiffeners in terms of spectral impedance, torsional impedance and spectral bending, respectively. The formulation was based on the principle of superposition and it allows considering an external excitation permitting an explicit solution for the plate's spectral velocity.

Mace [59–61] proposed a solution for periodically stiffened fluid-loaded plates by using Fourier transforms in a similar approach to Rumerman [91]. He derived expressions for the pressure and displacement of infinite stiffened plates with point and line excitations. It was shown that if the excitation is not directly on the stiffeners, the stiffeners effect on the vibrational response is greater at lower frequencies. The studies showed that the free wave propagation affects the acoustic pressure and radiated sound power in the far-field showing peaks at certain frequencies. The stiffeners' effect on the vibration of and sound radiation from a plate was studied by Eatwell and Butler [15]. They considered infinite fluid-loaded elastic plates stiffened with a finite number of beams. They studied different models, with equally and unequally spaced beams, under line or point excitation sources. It was shown that the plate with periodic stiffeners can produce passbands and stopbands at different frequencies that could be predictable, and plates with stiffeners spaced uniformly would not have the same predictability. It was mentioned that the periodicity of the stiffeners changes the nature of the free wave of the plate in the far-field, generating BF waves which may contribute the most to the vibrational response.

These BF waves are the waves that propagate at the passbands in periodically stiffened structures and very often could be the most significant contribution of undesirable noise in the far-field [13]. The BF waves are created as a result of the interaction between the plate flexural waves and the waves of the periodically placed stiffeners (inhomogeneities).

Lee and Kim [45] investigated the sound transmission through an infinitely long elastic plate, stiffened in a single direction, using the space harmonic approach and the virtual energy principle. In their model, the stiffeners were represented by lumped masses along with rotational and translational stiffnesses attached to the plate. They thoroughly considered the interactions between the stiffener and the plate, as well as the plate's interaction with the acoustic medium and derived an exact solution. Maxit [66] presented an efficient method to predict the vibration and sound radiation from infinite fluid-loaded stiffened plates excited by a point force. The proposed method was based on the use of Fourier transforms to analytically formulate the problem in the wavenumber domain; therefore, it was possible to utilise discrete inverse Fourier transforms and directly compute the displacement and pressure fields in the spatial domain. The proposed technique was verified by comparing the results with those obtained from a finite element model as well as available numerical results in the literature [60].

Maxit and Denis [68] estimated the vibroacoustic response of an fluid-loaded infinite stiffened plate for a naval test case. The plate was considered to be excited by a turbulent boundary layer (TBL). TBL was modeled based on the first version of the Chase 1987 model [8]. The plate formulation was similar to Maxit's earlier work [66]. It was found that the addition of stiffeners on the plate could increase the noise in the far-field for specific frequency bands, even though this addition can mitigate the vibrational response of the plate in other frequencies. It was also demonstrated that for different stiffener spacings this noise increment is related to the radiated BF waves that propagate to the far-field. Fig. 2.2 shows the radiated pressure spectra at 10 m away from the plate right above the point force excitation for three different stiffener spacings. The BF wave propagating frequencies are represented by a black dot on the x axis, showing that the highest amplitudes in the spectrum are inside the BF radiating bands. They also proposed an algorithm to find the propagating BF waves and explained how to determine the BF radiating band by examining whether they are in or out of the acoustic circle.

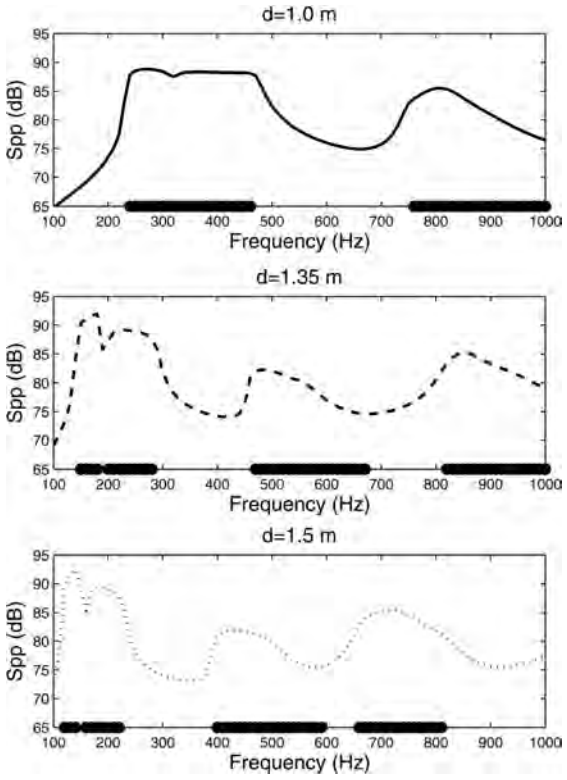

FIGURE 2.2: Radiated pressure spectrum at (0,0,10m), for distance between stiffeners of (a) 1.00 m ,(b) 1.35 m, (c) 1.50 m. Black dots in the x axis indicate the BF radiating frequency band. From Fig. 10 in Ref. [68].

Recently, Tran-Van-Nhieu et al. [96] proposed expressions to obtain the far-field pressure scattered of a fluid-loaded subjected to a harmonic plane wave, stiffened finite elastic plate using the classical plate theory. They calculated the scattered far-field pressure from 20 kHz to 300 kHz using an approximate analytical expression, finding the participation of Bragg diffraction and BF waves in the response's increase of amplitude. The Bragg diffraction is a result from the incident wave reflections on the joint of the stiffeners. Backscattering results from their proposed method were compared with experimental data, obtained using a wideband transducer with a central frequency of 200kHz, showing good agreement.

2.1.2 Cyllinder-like structures

In one of the pioneering studies on cylindrical shells, Burroughs [7] developed analytical expressions for the far-field acoustic radiation of fluid-loaded infinite circular cylinders with periodic ring stiffeners. In his model, the stiffeners interact with the shell exclusively through normal forces. It was shown that the radiation was provenient from low wavenumber in the source near field and also from scattering by the stiffeners. This scattering effect results in radiation patterns reminiscent of an array of ring radiators situated at the ring stiffeners. Hodges et al. [26, 27] analysed the vibration of a cylindrical shell with ring-stiffeners and predicted the travelling waves in an infinite structure. The proposed theory was validated experimentally showing good agreement up to the frequency of three times the ring frequency of the shell. Mead and Bardell [73] investigated the pass and stop bands of the free wave motion, in a periodically stiffened cylindrical shell portraying the fuselage structure of an aircraft. Hysteretic damping was added, which smoothed the propagation curves.

Yan et al. [117] investigated the power flow propagation of a fluid-loaded infinite periodically ring-stiffened cylindrical shell. They described the shell wall wave motions and the sound field in the fluid by Flügge shell and Helmholtz equations, respectively. It was shown that with the transmission of power flow through the axial direction of the structure, the valleys and peaks of power flow correspond to the stiffeners' positions. Later on, Yan et al. [116] applied the same methodology to a fluid-loaded infinite stiffened cylindrical shell with periodic stiffeners excited by a radial line force, and compared the sound power with those from an equivalent unstiffened structure. It was shown that by increasing the structural damping the sound power response will reduce remarkably. Based on the Flügge shell theory and Helmholtz equations, Zhou [123] studied a cylindrical shell conveying fluid stiffened with external rings along the axial direction of the cylinder. By analysing the vibration and stability of the structure, it was found that the effect of the addition of stiffeners could diminish the number of circumferential waves for the fundamental mode. This effect can lead to a higher critical fluid velocity depending on the number of stiffeners. Using the space harmonic method,

To include the stiffener's influence in the shell vibration, Maxit and Ginoux [69] proposed a numerical model based on the circumferential admittance approach (CAA),

permitting the modelling of internal frames with finite element method. It was demonstrated that the proposed method is suitable to describe the behavior of fluid-loaded non-periodically stiffened shells with axisymmetric internal frames, by comparing the displacements utilising three different approaches. Later on, Maxit [67] extended the same method, by proposing a numerical model to analyse the scattering pressure for a finite stiffened fluid-loaded cylindrical shell with internal axisymmetric frames excited by an obliquely incident plane wave. The proposed model was compared with experimental data from the literature for a periodic stiffened shell showing good agreement. The method was extended again by Meyer et. al [79] which developed the condensed transfer function (CTF) to include the assembly of models with axisymmetric and non-axisymmetric internal frames. CAA and CTF methods were then combined to model a fluid-loaded non-periodically stiffened shell. It was found that the non-axisymmetric internal substructures could modify the vibroacoustic behavior of the shell and lead it to a higher radiation efficiency. Fig. 2.3 shows the comparison for the system calculation using the proposed CTF method, combined with the FEM and CAA and a FEM as reference solution, for the radial velocity at the excitation point and the mean quadratic velocity on the shell surface. As shown by Fig. 2.3 the comparison between the CTF method combined with FEM and the reference FEM indicate good agreement. As the authors highlights the small differences between the CTF with CAA and the reference FEM is that CAA is only an approximation and can lead to small deviations.

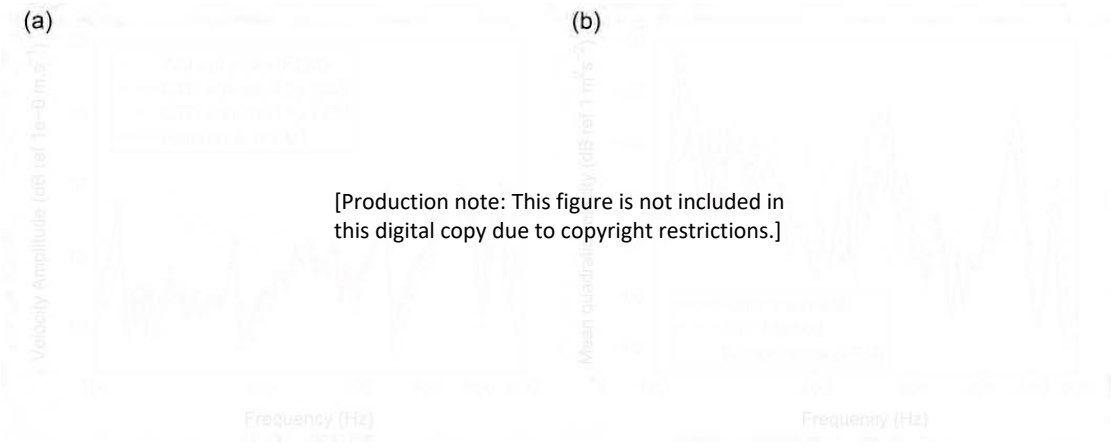

FIGURE 2.3: Frequency response of (a) the radial velocity at the location of excitation and (b) the mean quadratic velocity on the outer shell surface. From Fig. 8 in Ref. [79].

Qu et al. [90] modeled a coupled propeller shafting, and a submarine pressure hull system with longitudinal stringers subjected to different propeller excitation forces. They

combined the Modified Variational Method and the spectral Kirchhoff-Helmholtz integral formulation to predict the acoustic field. An equivalent model was obtained from the coupled FEM/BEM to verify the proposed model. The model of the propeller-shaft system includes a rigid propeller, an elastic shaft, radial bearing, and a thrust bearing, which in the proposed model are considered to be a lumped mass, an elastic beam, and a spring-damper system. The results showed that the radiated sound power from the propeller shaft to the pressure hull could be reduced by decreasing the axial stiffened of the thrust bearing, and the change in the dimensions of the ring stiffeners does not have any significant effect when the system is under the axial propeller force. Using Donnell [14] equations for cylinders, Tong et al. [95] modeled analytically an infinite periodically stiffened cylindrical shell with longitudinal ribs under point excitation. It was found that there are multi-order Bloch-Floquet waves in this type of periodic structure, and its supersonic components can radiate to the far-field. It was demonstrated that this radiation occurs due to phase-matching of the waves in the mid-to-high frequency range.

2.2 Surface contribution identification methods

Identifying the contributions of different surface regions to radiated noise and vibration is crucial for effective control and mitigation in engineering applications. These identification methods provide valuable insights into the specific areas of a structure that significantly influence acoustic radiation and vibrational energy. This section delves into techniques that enable precise localisation and quantification of sound and vibration sources.

2.2.1 Near-field acoustic holography

The Near-field acoustic holography (NAH) is among the first methods used to locate the acoustic energy source areas on vibrating structures [113, 114]. NAH is an experiment-based method that uses microphone measurements to compute the vector field of acoustic energy in a 2D surface in the acoustic near-field. This method considers the evanescent wave spectrum to rebuild the acoustic field. To improve the method, Maynard et al. [70] and Williams et al. [111] proposed a new technique based on NAH, named generalized

near-field acoustic holography (GENAH). This technique considers an acoustic pressure measurement on a 2D surface, so the 3D sound field can be rebuilt using helical waves instead of plane waves and by converting the pressure field to cylindrical coordinates at a constant radius.

With the GENAH, new methods could be introduced as presented by Veronesil and Maynard [102] in their work on digital holographic reconstruction, trying to achieve theoretical and practical applications of reconstruction of odd-shaped sources. The method makes use of triangular shapes to discretize complex structures. Rather than using the 2D Fourier transform to reproduce the acoustic field, this method takes into account the singular value decomposition (SVD). Using this method, they reconstructed a rigid sphere with a small piston with a 60-faced polyhedron model. Utilizing the same method, Borgiotti et al. [4] was able to reconstruct with high resolution the normal velocity on the surface of an acoustic tank (cylindrical shell) using pressure data. By comparing the results with experimental data, it was confirmed the method's viability on a wide frequency band. Kim and Ih [38] also used the same method with SVD in the automotive industry, specifically by applying this technique in a half-scaled automotive cabin. Their work presented an improvement in the resolution of the reconstructed field by utilising the BEM to formulate the problem and the SVD to obtain the least-square solutions and filter out non-radiating components. This combination helped in dealing with the ill-posed nature of the inverse problem caused by the singularity of the transfer matrix. To further enhance resolution, they applied the effective independence method to determine optimal measurement positions, reducing the number of required measurement points and minimising the singularity of the transfer matrix. This method ensured that the measurement locations contributed maximally to the independence of the field pressures, improving the quality of the reconstructed data. Utilising this numerical procedure of regularisation methods, more works followed the same idea with different methods [24, 38, 109] trying to achieve better results for specific problems. As Kim [39] highlights, good results using this alternative are dependent on the proper choice of the regularisation parameter even if there is no prior knowledge on the accuracy and reliability of the measurements. William et al. [112] combined NAH with the boundary element method to compute the normal velocity over the surface of a fuselage of a turboprop airplane in an in-flight hologram reconstruction. Fig. 2.4 shows the velocity field over the surface for an exterior excitation point, the comparison between the reconstructed

velocity on the left and the exact solution on the right showing good agreement.

FIGURE 2.4: Velocity field for an airplane fuselage comparing Near-field acoustic holography and the exact solution adapted from Fig. 5 in Ref. [112].

The need to utilise the method on larger structures influenced the introduction to new methods [92–94, 100] to improve the NAH technique since it has a high computational cost and a great effort on measurements required by it.

2.2.2 Acoustic intensity based methods

A shared interest in many engineering applications is the far-field radiation of sources, as it is often this radiation that a potential observer is exposed to. Acoustic intensity measurement has been vastly used for sound source localisation since its first introduction. Fahy summarises several works with the acoustic intensity method in his book [18]. Even though this method can help locate the structure hot spots and is a commonly used method, it has its own limitations. As William's [106] mentions, the problem with this method is the circulating power flow in the near field of plate-like structures when these structures are excited below local coincidence frequencies since this method considers the contribution of evanescent waves of the vibrating structure to the acoustic energy in the near-field. To address these challenges, alternative methods such as the Supersonic Intensity (SSI) and NNI have been developed. SSI focuses on the propagative components of the acoustic field, filtering out the evanescent waves to provide a clearer

representation of the radiated sound power. Conversely, NNI aims provide a more accurate estimation of the radiated sound by ensuring non-negative intensity values, thus overcoming the limitations of traditional acoustic intensity methods in capturing the vibrational energy distribution.

2.2.2.1 Supersonic acoustic intensity

Several tools to detect the acoustic sources have been developed and applied to localise structure regions that contribute most to the vibroacoustric response. Compelling alternatives such as supersonic acoustic intensity helps to identify exact hot spots and strength of these acoustic sources by filtering out the contribution of those evanescent subsonic wave components.

This method was introduced by Williams [106, 107] to locate the radiating regions on structures. As the name of this tool already suggests, SSI does not take into account evanescent waves (subsonic waves) that do not radiate to the far-field. This technique disregard these subsonic components, thereby isolating the so called SSI. Similar to the acoustic intensity, the SSI is obtained from the product of the supersonic components of the velocity and acoustic pressure, considering only wave-numbers inside the acoustic circle. This tool presents a higher accuracy than the regular acoustic intensity to locate regions in which the noise is radiated to the far-field [106]. Fig. 2.5 presents a comparison between acoustic intensity, on the right, and the SSI, on the left for a cylindrical shell with hemispherical-like endcaps and total structural length L, with a circular plate welded to the shell structure at position $L/3$. William highlights that the acoustic intensity can show an approximated location of the source in the shell surface, but the SSI technique can provide a more precise location of the noise source.

Using a different approach than the formulation by Williams in wave-number domain, Fernandez-Grande et al. [20] presented a direct formulation in the space domain by excluding the evanescent waves in near-field by a spatial filter mask developed on the first-order Bessel function, which corresponds to the representation of the supersonic part of the radiation circle. The direct calculation was computed using a 2D convolution between the developed filter mask and the acoustic field and validated using experimental data from a planar radiator. Later on, to verify the method's accuracy, Fernandez-Grande and Jacobsen [19] performed an experiment on the finite aperture

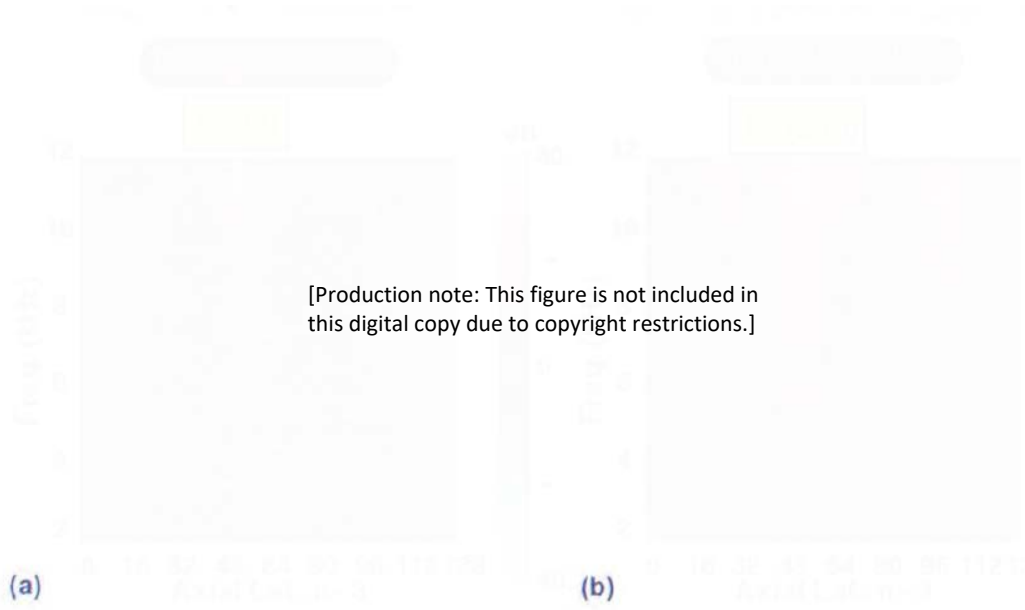

FIGURE 2.5: Results for the surface of the proposed cyllindrical shell for: (a) radial acoustic intensity, (b) super sonic acoustic intensity, from Fig. 3 in Ref. [106].

error due to spatial truncation. The results demonstrate that at lower frequencies, with the wavelength and the range of the filter-mask larger than the size of the structure, the error inserted by the finite aperture in the assessment was substantial. At higher frequencies, the error is not that substantial as a result of the slender lobes of the filter mask, and it can be diminished by adding a cut-off frequency of the corresponding wave-number. This filter eliminates all subsonic wave components, leading to the supersonic intensity with mitigated aperture errors.

Valdivia et al. [101] obtained the SSI by removing the subsonic waves from the NAH evaluation utilising a filtering process. The proposed method is on the basis of a stable invertible representation of the power operator. This operator can be obtained using the equivalent source formulation and complete spectral basis. They used a spherical geometry to demonstrate the technique testing it using numerically generated data. They also used vibrating ship-hull experimental data utilising NAH to validate the proposed method. Magalhaes and Tenenbaum [62] extended the SSI technique to consider arbitraly shaped sources by utilising the BEM and SVD. This extended technique applied the Kirchoff-Helmholtz equation in a discretized form to create a radiation operator linking the normal velocity on a source's surface to the pressure at field points. The SVD is then used to filter out evanescent components, ensuring that the supersonic

acoustic intensity accurately represents the energy transmitted to the far field. Since then, the SSI technique has been extended, and different methods have been proposed as alternatives to accurately locate hotspots [21, 23, 33].

2.2.2.2 Non-negative intensity

An alternative to the SSI method was introduced by Marburg [63] to be a powerful tool to locate the surface areas that can take part in the radiated sound power (hot spots). This technique is an intensity-based tool considering only the positive contributions of the vibrating surface, aiming to eliminate the cancellation effects. Williams [110] named this method of surface contributions to the radiated sound power considering exclusively positive intensity distribution in the plane as Non-negative Intensity. In his work he proposed, two formulas deriving from velocity-only and pressure-only measurements for planar structures and a set of hybrid-intensity formulas, yielding a bipolar intensity using convolution integral for the normal intensity and power. He highlights that NNI works best at frequencies where the smallest dimension of interest is larger than a half-wavelength. Both velocity and pressure NNI formulas yield similar results, showing that the method can predict the regions where the structure emits sounds (hot spots sound production) to the far-field. Utilizing the spectral decomposition of the power operator, Valdivia [99] developed a method to achieve an NNI expression. Comparing SSI and NNI results using numerical models showed that the developed NNI expression is valid. Later on, Valdivia [98] validated the proposed methodology utilising numerically generated data of an elastic spherical shell with a point force excitation.

Liu et al. [53] evaluated the SSI and NNI methods to localise the vibrating areas at the surface of three different structures, such as a 3D baffle plate, a cylindrical shell, and an engine crankcase. Utilising the SSI technique at lower frequencies for a 3D structure, the results showed low accuracy due to a mismatch in size of the spatial radiation filter. Fig. 2.6 shows the maps of the particle velocity distribution, the acoustic intensity, the SSI, and the NNI for the engine crankcase at specific frequencies. With the comparison between maps, it is possible to see the difference between the different identification methods to locate hotspots, being visible that the NNI method is able to show more clearly the hotspot. Liu et al. [54] used BEM to formulate the NNI to predict and compare the scattered sound power on the surface and also in the acoustic far-field for

three different surface areas, a rigid cylinder, a rigid sphere, and a rigid hemispherical shell.

FIGURE 2.6: Maps of the particle velocity distribution, the acoustic intensity, the supersonic intensity and the non-negative intensity for the engine crankcase at specific frequencies and modal assurance criterion. From Fig. 9 in Ref. [53].

Liu et al. [51, 54] extended the NNI with a method he named back-calculated NNI. Unlike the regular NNI, which calculates the acoustic impedance matrix at the structural surface, this new approach determines it at the far-field receiver surface. Later, Liu et al. [52] compared different methods to investigate and examine the influence of inhomogeneous Rayleigh damping on radiated sound power of the surface of elastic structures by

testing several different configurations. As a result of investigating the particle velocity, it was found that high damping values can influence the propagation of the travelling waves towards these regions. Due to the characteristics of NNI that eliminate the cancellation from positive and negative acoustic intensity values, this method is a powerful tool for noise control in structures with these inhomogeneous distributions of Rayleigh damping.

The NNI method was applied by Wilkes et al. [105] by adapting the fast multipole boundary element to calculate the acoustic impedance matrix in a two-stage solution method. They applied this method to a large-scale cylindrical shell submerged in water. This extension of the NNI method was able to locate contributions of regions of the surface to the radiated sound power in fluid-structure interaction problem in large-scale models. Karimi et al. [34] formulated the NNI analytically for planar structures under stochastic excitation. They applied the formulation into a baffle plate excited by an acoustic diffused field or a turbulent boundary layer. The NNI was derived in terms of the cross spectrum density function of the stochastic field for normal fluid particle velocity and acoustic pressure. Results showed that the NNI distribution pattern changes with the frequency of excitation and the type of excitation as well, and high levels of radiation efficiency lead to concentrated distribution areas of NNI on the panel surface

2.3 Control of vibroacoustic responses of structures

Control of the vibroacoustic response from general structures usually can be obtained by either modifying the dynamic properties of the structure or by employing controlled secondary sources of vibration (passive and active control, respectively) [17]. Active and passive control strategies have been employed in several structures to achieve optimal design and vibrational responses. A common passive mechanism of damping vibrations is the use of a viscoelastic damping material. Viscoelastic materials have been extensively employed to control the vibroacoustic response in various structural applications due to their ability to dissipate energy. These materials exhibit both viscous and elastic characteristics, allowing them to effectively dampen vibrations through internal friction mechanisms [81]. The energy dissipation is primarily achieved through hysteresis, where the viscoelastic material undergoes cyclic deformation, converting mechanical energy into heat. This process is influenced by factors such as temperature and frequency,

making viscoelastic materials particularly versatile for a wide range of applications [125]. A comprehensive review of vibration damping using viscoelastic materials can be found in Ref. [125].

Traditionally, damping using viscoelastic materials has been applied using three main methods. Viscoelastic damping with unconstrained (or free) layer [71, 78, 84], constrained layer [25, 35, 37, 74] and active constrained layer [32, 97]. Fig. 2.7 shows the two main damping methods using viscoelastic materials. Unconstrained damping is the simplest damping method using viscoelastic materials, requiring only the attachment of the damping layer to the structure as shown in Fig. 2.7(a). However, its effectiveness is highly dependent on the excitation frequency and temperature [124]. The constrained layer damping, is vastly used in industry due to the higher efficiency in damping compared to a viscoelastic layer (VL). Constrained viscoelastic layer (CVL) is the application of a VL, which is then constrained by a stiffer outer layer. Fig. 2.7(b) shows the CVL applied to a host structure, in which the constrained layer is represented by the green layer. The primary mechanism of energy dissipation in CVL is through shear deformation within the viscoelastic layer, which converts vibrational energy into heat, thereby reducing the amplitude of vibrations [89].

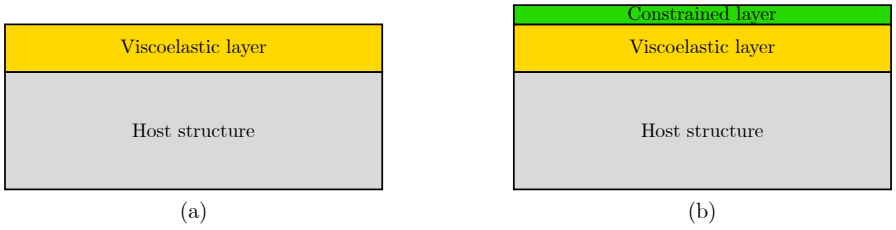

FIGURE 2.7: Host structure (gray) with a (a) VL and (b) CVL. The viscoelastic material is represented by the yellow layer and the constrained layer is represented by the green layer.

Mentel [78] experimentally investigated the effectiveness of viscoelastic damping at the boundaries of beams and circular plates under steady-state vibration conditions. The beams and plates were excited at the centre using an electromagnetic shaker. Results showed that a small inset of a VL at the supports significantly enhanced damping by increasing energy dissipation. The findings demonstrated that the optimised VL design could increase the cyclic energy loss by a factor of 3 for steel and aluminium beams and by a factor of 5 for aluminium circular plates. Theoretical analyses supported these findings, showing the damping effectiveness was due to shear deformations in the VL. Khalfi

and Ross [37] studied the transient response of a plate with a CVL. They developed an analytical model using Lagrange's equations to derive the governing equations, assuming the stiffness of the VL to be complex and frequency-dependent, represented by the Prony series. The plate was subjected to an impact excitation, and the equation of motion was converted to the frequency domain using the fast Fourier transform (FFT), then reverted to the time domain with the inverse fast Fourier transform (IFFT). The model was validated against existing literature for harmonic motion and experimental data for transient response, showing good agreement. Their findings demonstrated the effectiveness of the CVL in reducing vibration in plates impacted by external forces. Trindade et al. [97] investigated hybrid active-passive damping treatments for a cantilever beam. The active-passive mechanism was based on a VL attached to the cantilever beam and a piezoelectric patch on top of the VL. The study compared two models based on FEM, the Anelastic Displacement Fields and Golla-Hughes-McTavish models, to account for frequency dependence in the viscoelastic materials. The excitation was considered to be a transversal force applied to the beam's free end. It was found that hybrid damping was more effective than the VL alone, even with optimal VL thicknesses and lengths.

While CVL damping effectively reduces vibrations through passive means, active control techniques can offer dynamic solutions that can adapt to changing conditions. By integrating sensors and actuators, active control methods provide real-time adjustments to counteract vibrations, enhancing the overall performance of structural damping systems. Recently, Chi et al. [9] investigated the vibration control of beams with active constrained layer damping (ACLD). The constrained layer was a piezoelectric layer bonded to the viscoelastic material. A dynamic model of the beam with ACLD was developed based on the modal superposition method. The model was validated against existing literature and by an experimental model. The beam was subjected to impact excitation, and the effects of control parameters, such as controller bandwidth, control gain, and observer bandwidth, were analysed. It was found that the ACLD significantly damped the system's vibrational response and was more effective than the CVL, by improving energy dissipation and reducing vibrations through the force generated by the piezoelectric layer.

Elliot et al. [16] proposed an active control utilising a multichannel feedback control system to a simply supported finite baffled panel, excited by a plane acoustic wave. The modal response of the panel and the sound radiation are analysed and controlled

utilising point force and piezoelectric actuators. The multichannel feedback control system is made with 16 individual single channels with diverse feedback gains. It was shown that kinetic energy and sound transmission ratio could be controlled for a large frequency band at lower frequencies. To control laminated composite plates, Liu et al. [55] proposed an active control using piezoelectric integration on the plate with a simple negative velocity feedback control algorithm. The proposed approach was aimed for the shape control and mitigation of the active free vibration of the laminated plate. The plate is considered to be flat and is excited by a distributed load. It is shown that is possible to control the shape and free vibrational response of the structure with piezoelectric actuators. The simulation was made using a finite element model, and the results were compared with existing data in the literature to validate the approach.

Mukherjee et al. [82] proposed an active control of stiffened plates utilising piezoelectric effects. The formulation is based on the FEM and the control utilises a velocity feedback. They proposed a general formulation for stiffened plates and applied to different problems in the literature, an unstiffened and stiffened plate subjected to air blast, a stiffened cantilever plate with sinusoidal load and one with the stiffener not passing through the nodal line. It was shown that the active control was able to change the vibrational response of the problems by altering the gain in the velocity feedback signal. Philen and Wang [88] proposed the use of active stiffeners to control the vibrational response of a circular plate. Using the finite element method, they modelled the circular plate with stiffeners and piezoelectric actuators. The active stiffener is a piezoelectric actuator intended to reduce the moment transmitted to the plate, causing a directional decoupling effect. The model was validated with an experimental setup subjected to impact testing. The comparison between the system with the stiffeners direct-attached and the active stiffeners actuators showed that this solution was able to control the vibration of the plate, presenting a lower average power spectrum. Active control techniques provide dynamic, real-time vibration suppression, but they can be complex and energy-intensive. As an alternative, ABHs can be a passive, yet highly effective solution for vibration reduction by leveraging the geometric tapering of structures to dissipate vibrational energy efficiently, and for certain cases without the addition of mass.

2.3.1 Acoustic black holes

ABHs have emerged as a notable strategy for mitigating vibrations in structures. An ideal ABH is an engineered structure featuring a continuously varying cross-sectional area that its thickness decreases following a power-law profile along its length towards zero as described by Mironov [80] in his pioneer work. This ideal ABH geometry induces a unique phenomenon where the velocity of flexural waves gradually reduces and the travel time will prolong infinitely, leading to the elimination of wave reflections. This ideal design is not feasible in practical applications, as the end of the ABH will always have a residual thickness. The ABH concept was also investigated by Krylov and Shuvalov [41] when studying the propagation of localised flexural vibrations along the edges of plates with thickness profiles described by a power law. The primary focus was on wedge acoustic waves, which are characterized by the concentration of elastic energy near the edges. Krylov and Shuvalov used the geometrical acoustics technique to analyse these wave propagation characteristics and derived conditions under which localised flexural waves can propagate without significant reflection, demonstrating that wedges with specific power-law profiles can effectively trap incident flexural waves. Although ABH showed promising damping characteristics, the ideal design is not feasible in practical applications, as the edge of the ABH will always have a residual thickness. This limitation led the solution proposed by Krylov, which studied theoretically [42] and experimentally [44], the addition of viscoelastic damping layers to reduce the reflections caused by the truncation of the ABH edge. This solution changes the dissipative mechanism from reducing the wave speed and prolonging the propagation time to absorbing the bending waves at the edge, where the vibrations are concentrated.

ABHs have been validated as efficient vibration absorbers through numerical simulations [13, 104, 115] and experimental studies [44, 86, 118]. They are implemented in various configurations, such as 1D wedges as shown in Fig. 2.8 and 2D indentations as presented shown in Fig. 2.9. The 2D ABH is formed by rotating the 1D thickness profile around a central axis. ABHs are especially effective for vibration mitigation as they serve as broadband absorbers beyond a certain frequency threshold. However, recent findings indicate that at low to mid frequencies, where modal density is low, embedded ABH structures can exhibit local mode shapes where the ABH-containing section remains non-vibrating, thus rendering the ABH ineffective.

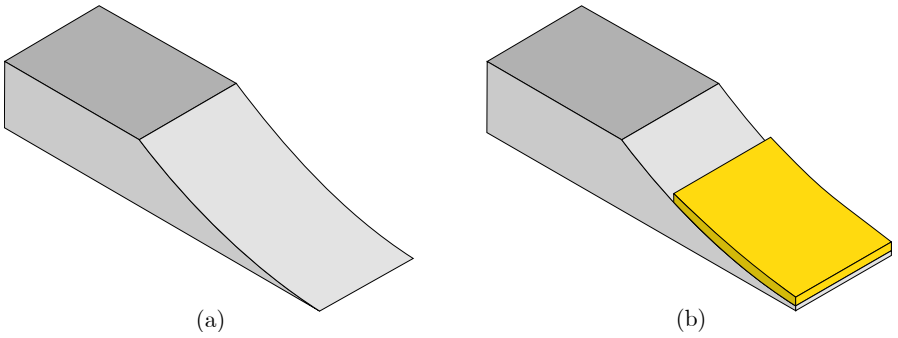

(a) (b)

FIGURE 2.8: Uniform beam (gray) with a embedded 1D (a) ideal ABH and (b) ABH with non-zero tip with a damping layer (yellow).

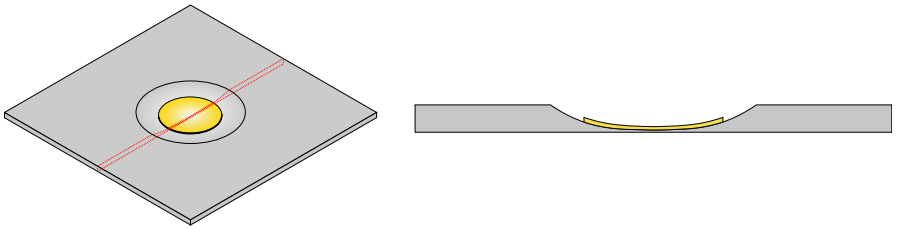

(a) (b)

FIGURE 2.9: Uniform plate with a embedded 2D ABH (gray) with damping layer (yellow), presented in a (a) 3D view and (b) side view of a cross section marked in red in the 3D view.

Different dissipative layers have been studied, including piezoelectric layers as the work from Zhen et al. [121] which investigates the aeroelastic characteristics and active control of one-dimensional ABH structures subjected to supersonic airflow. Their approach involved applying piezoelectric layers at the tip of the ABH to enhance structural stability under aerodynamic loads through an active control system using a feedback algorithm. They derived the motion equations using Hamilton's principle and modeled aerodynamic pressures using the first-order piston theory. The findings revealed that the proposed feedback control significantly boosts aeroelastic stability and critical pneumatic pressure, effectively reducing vibrations, especially at lower-order resonances. Wan et al. [103] investigated a method to enhance the wave suppression capabilities of ABH plates specifically in the low-frequency range. They introduced shunt damping combined with a viscoelastic damping layer as a strategy to improve the effectiveness of ABH plates. Utilising a semi-analytical approach based on the Kirchhoff–Love plate theory and Hamiltonian principle, they analysed the natural frequencies and vibration characteristics of ABH plates, incorporating modified Fourier series as shape functions. Their approach was validated through comparisons with FEM simulations. It was found

that ABH plates equipped with shunt damping exhibit significant suppression of resonant formants in the low-frequency range, with the potential to enhance suppression performance at higher frequencies by increasing the thickness of the viscoelastic damping layer.

Several configurations of ABHs have been studied to understand its capabilities in vibration mitigation [2, 48], sound absorption [50, 58], and energy harvesting [29, 46], either embedded into the main structure [57, 120] or as attached vibration dampers [30, 56, 122]. Many of these configurations and works have been reviewed by Pelat et al. [87] in their review of the theory and applications of ABHs. Here, works are divided into embedded ABHs and attached vibration damper ABHs.

2.3.1.1 Embedded ABHs

Considering ABHs embedded in a plate, Bowyer and Krylov [5] conducted an experimental analysis to investigate the capability of circular ABHs in reducing the acoustic response when compared with uniform plates. They compared the acoustic power response of a plate embedded with several circular ABHs and a central hole, to that of a uniform reference plate. Both plates were subjected to harmonic excitation through a point force. It was noted that while the vibration amplitudes at the centres of the ABHs were increased, the overall plate vibration was reduced and led to a mitigation in the sound radiation. This was ascribed to the synergistic impact of the ABH indentations and the acoustic short-circuiting resulting from the presence of the central hole. Feurtado and Colon [22] investigated the use of wavenumber transform analysis to design and optimise ABHs in structures for vibration reduction and sound radiation control. This analysis allowed them to visualise and quantify the changes in bending wave speed, vibration amplitude, and energy dissipation due to the ABH effect. It was shown that the damping layer could be up to six times the size of the tip of the ABH before the loss factor from the damping layer diminishes. The results showed that when the ABH dynamics dominate the system response it could lead to lower vibration and sound radiation levels. This was attributed to the redistribution of supersonic bending waves into subsonic wavenumbers.

Hook et al. [28] studied the influence of the geometric parameters of beam's ABHs, on modal density and the reflection coefficient using a numerical model of the ABH subjected to a point force. It was shown that the ABH can be tuned for a specific frequency band, and by changing the tip of the ABH the modal density can be changed to an optimal result. They found that, by increasing the length of the ABH the reflection coefficient is minimised. The study was validated by an experimental case, considering a structure subjected to a point excitation with white noise, showing the same pattern of change in the reflection coefficient by varying these parameters. Deng et al. [13] utilised the wave finite element (FE) model to study the capability of embedded ABH in a cylindrical shell structures to reduce BF bending waves when subjected to a ring excitation. They investigated the BF passbands and stopbands in both uniform and ABH-embedded infinite cylindrical shells, demonstrating how ABHs can significantly alter these bands. The authors highlighted that while ABHs enhance vibration damping, they also reduce the shell's stiffness. In most applications this could be a disadvantage of embedded ABHs. To overcome this disadvantage, Zhang et al. [119] proposed ABH indentations with reinforcing stiffeners in a plate. Using a symplectic space wave propagation model, they showed that the ABH could still mitigate the plate's vibration, but the results indicated the mitigation effectiveness decreased due to the addition of reinforcements highlighting the limitation of embedded ABHs. Efforts to address this constraint have led to the emergence of additive ABHs, with initial investigations conducted following the concept's inception in Zhou et al. [122] work.

2.3.1.2 Attached vibration damper ABHs

Zhou et al. [122] investigated the use of ABH as a dynamic vibration absorber (DVA). The approach combines DVA and waveguide absorber (WGA) principles, requiring no complex tuning and no variations in the host structure. They considered the vibration response of a beam as a benchmark solution, and employed numerical simulations using the FEM and experiments to demonstrate the ABH-DVA effectiveness in reducing vibration amplitudes at multiple resonance frequencies of the host structure across a broad frequency range. Fig. 2.10 shows the experimental results for the comparison between the case with and without the ABH-DVA. Considering the case with the ABH-DVA, it was noted that it significantly suppresses the resonant peaks of the primary system across a wide frequency range, except for certain specific frequencies. This observation

aligns with the general vibration reduction phenomena predicted by their numerical simulations.

(a)

[Production note: This figure is not included in this digital copy due to copyright restrictions.]

(b)

FIGURE 2.10: Comparisons of the measured (a) driving and (b) cross point mobility of the primary host beam with and without ABH-Resonant Beam Damper (RBD). From Fig. 12 in Ref. [122].

In a similar approach, Ji et al. [30] investigated a 2D circular ABH-DVA designed to enhance vibration mitigation in arbitrary structural applications. Their focus was to address the limitations of embedded ABHs, which often compromise structural stiffness and strength. Using FE simulations and experimental results, they analysed the performance of the 2D ABH-DVA when attached to a plate. The results showed that the 2D ABH-DVA significantly reduced resonant peaks over a broad frequency range, primarily through the dynamic interaction of the ABH-DVA and the structure and the damping characteristic of the ABH. Later, Ji et al. [31] extended this work by studying a 2D circular eccentric ABH-DVA to mitigate vibrations in plate structures utilising the FE simulations and experimental results. It was shown that the 2D Eccentric ABH-DVA also significantly lowers resonant peaks across a broad frequency range, and can reduce the vibrational response in 15 dB when compared to the system with their previous design of the 2D circular ABH-DVA. Using a 1D ABH-DVA Li et al. [49] developed a semi-analytical method utilising the Gaussian expansion method (GEM) and the Rayleigh–Ritz method to characterise the complex coupling between the ABH-DVA and the host structure. They validated the model against FE simulations and conducted

experiments to assess the damping effects of the ABH-DVA. Key findings include the identification of optimal sizes for ABH-DVAs and damping layers, and the demonstration that properly shaped ABH-DVAs significantly reduce vibration levels across a broad frequency range.

Deng et al. [12] also observed a wide vibration damping across a broad frequency range when studying ABH pillars attached to a plate excited by a point force using the Rayleigh–Ritz method. It was noted that the inherent loss factor of the beams and damping layer can unify the local resonance and Bragg scattering bandgaps. Additionally, it induces notable dissipation within the passbands, leading to the presence of substantial evanescent waves throughout the entire analysed frequency range. Li et al. [47] investigated the efficacy of a vibration absorber that integrates the ABH effect with vibro-impact mechanisms, aimed at enhancing low-frequency vibration attenuation. Their study employed both numerical and experimental methodologies, using an FE model to simulate the dynamics of the absorber applied to a honeycomb panel, alongside conducting parametric studies to refine the design variables such as impact mass and stiffness. It was shown that the vibro-impact ABH absorber significantly mitigates vibrations across a broad frequency spectrum by efficiently transferring energy from lower to higher frequencies where it was dampened by the ABH-DVA.

A synthesis of the literature reveals several critical gaps that have directly shaped the objectives of this thesis. A notable gap is the insufficient understanding of where vibrational energy localizes when excitations occur within a BF wave passband. Despite comprehensive studies on vibroacoustic responses in stiffened structures and advanced surface contribution identification methods, current research has not adequately shown the specific regions that predominantly radiate sound power within BF passbands. This shortcoming motivates the present investigation to study the vibroacoustic behaviour of stiffened structures when excited in such BF passbands. Furthermore, the literature underscores the efficacy of NNI as a powerful tool for localising and quantifying regions responsible for significant sound radiation, offering a promising approach to elucidate BF wave propagation and related interaction mechanisms. Moreover, while ABH have been explored as a means of controlling vibroacoustic responses, their integration with stiffener designs in fluid-loaded structures remains largely unexplored. The potential for ABHs to mitigate both the transmission of vibrational energy and the generation and

propagation of BF waves represents an untapped avenue for research. This study, therefore, seeks to evaluate the feasibility and effectiveness of incorporating ABH concepts into stiffened structures. By systematically addressing these gaps, this research aspires to enhance our understanding of vibroacoustic behaviour of fluid-loaded structures and to develop innovative strategies for controlling vibration and sound radiation in complex structural systems.

Chapter 3

Non-negative intensity for a heavy fluid-loaded stiffened plate

This chapter presents theoretical developments and subsequent findings regarding the use of NNI to identify the contribution of BF waves to the radiated sound power of a heavy fluid-loaded stiffened plate. The analytical formulation is presented in Section 3.1, where the plate response is modelled using a wavenumber domain approach. The formulation begins with the equations of motion for a fluid-loaded stiffened plate, considering the periodicity of the stiffeners and the fluid-structure interaction. The amplitudes of the transverse displacement of the plate are derived from the dynamic stiffness of the fluid-loaded plate, incorporating the contributions of the stiffeners through their flexural and torsional dynamics.

The interaction between the plate's flexural waves and the stiffeners' flexural/torsional waves generates BF waves, which are characterised by their propagation in passbands and attenuation in stopbands. These BF waves significantly contribute to the radiated sound power, especially when their wavenumbers are below the acoustic wavenumber. The NNI formulation, is then introduced (Section 3.2) to identify and visualise the surface regions contributing to the far-field radiation.

The predicted results are presented in Section 3.3. Verification of the analytical results is achieved through comparisons with results available in the literature, demonstrating the accuracy of the wavenumber domain approach. The study explores the effects of stiffeners on the vibroacoustic response, focusing on the generation and propagation of

BF waves and their influence on the radiated sound power. The results show that BF waves predominantly radiate in specific frequency bands, and the NNI maps effectively identify these regions. The influence of excitation position, material damping, and structural parameters on the NNI distribution is also investigated, providing a comprehensive understanding of the vibroacoustic behaviour of stiffened plates.

This chapter is based on the article "Non-negative intensity for a heavy fluid-loaded stiffened plate," published in the *Journal of Sound and Vibration* [65].

3.1 Infinite fluid-loaded stiffened plate formulation

Let us consider a infinite fluid-loaded thin plate. The infinite plate is coupled with identical stiffeners distributed periodically throughout its extension, along the x-axis, or $x = nd$ with n being an integer ($\mathbb{Z}$) related to the stiffener number, and d is the distance between stiffeners as shown in Fig. 3.1. The stiffeners are considered to be uniform beam-like stiffeners. The connections between the plate and stiffeners are assumed to be rigid.

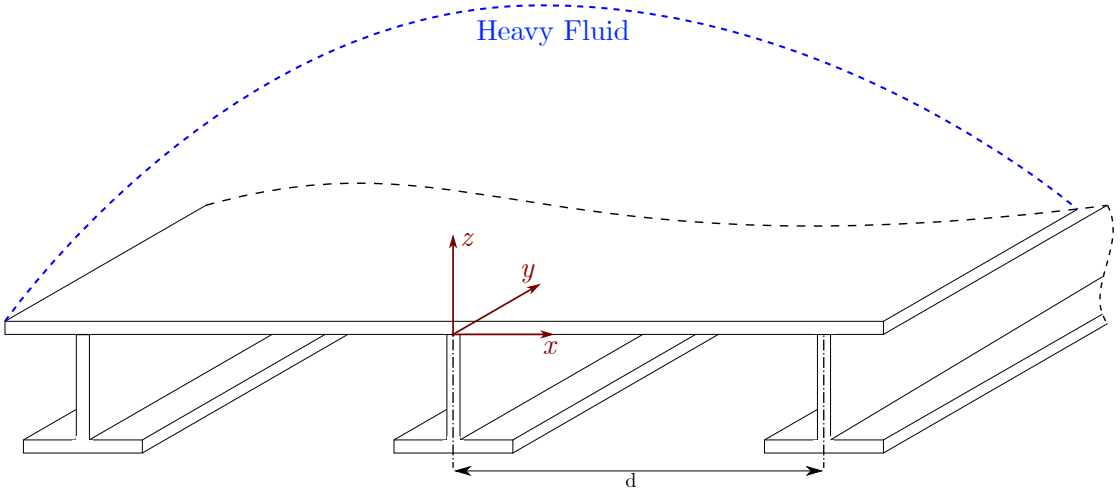

FIGURE 3.1: Infinite plate with periodic stiffeners upon fluid loading

The subsequent analysis is based on the parameters for the T-shaped stiffeners and the steel plate as presented in Table 3.1. The plate thickness, dimension of the stiffeners and the material properties are chosen such that the stiffened plate represents a typical naval structure. The fluid properties, mass density (ρ_f) and sound speed (c_f) are 1000 kg/m^3 and 1500 m/s, respectively.

TABLE 3.1: Material and geometrical proprieties of the proposed structure.

Parameters	Plate	Stiffeners
Mass density ($\rho_{\mathrm{p,s}}$)	7800 kg/m^3	7800 kg/m^3
Young's modulus (E)	$2.1 \times 10^{11}\,(1 + \mathrm{j}\eta)$ Pa	$2.1 \times 10^{11}\,(1 + \mathrm{j}\eta)$ Pa
Loss factor (η)	2%	2%
Poisson's ratio (ν)	0.3	0.3
Thickness (h)	0.05 m	—
T cross-section web	—	0.15 m $\times$ 0.08 m
T cross-section flange	—	0.08 m $\times$ 0.15 m

The plate is submitted to a fluid loading on one side of the plate, and a point force is applied on the bottom towards the top of the plate, in the z direction.

3.1.1 Vibroacoustic analysis of the plate under point force excitation

The plate is considered to be excited by a point force F_0 at a position $(x_0, 0)$. Considering the Love-Kirchhoff assumptions, and omitting the harmonic time dependence ($e^{\mathrm{j}\omega t}$, in which ω and j are the excitation frequency and the imaginary unit, respectively) for the following developments, the equation of motion of the fluid loaded stiffened plate can be written as [59, 66, 68],

$$\begin{aligned} D\nabla^4 W(x,y) - \omega^2 \rho_{\mathrm{p}} h W(x,y) =& F_0 \delta(x - x_0)\,\delta(y) - p(x,y,0) \\ &- \sum_{n\in\mathbb{Z}} F_{\mathrm{s}}(x,y)\,\delta(x - nd) \\ &+ \sum_{n\in\mathbb{Z}} \frac{\partial}{\partial x}\left(M_{\mathrm{s}}(x,y)\,\delta(x - nd)\right), \end{aligned} \tag{3.1}$$

where δ is the Dirac delta function, $F_{\mathrm{s}}(x,y)\,\delta(x - nd)$ and $M_{\mathrm{s}}(x,y)\,\delta(x - nd)$ are respectively the force and moment distributions related to the interaction between the plate and the nth stiffener. D, h and ρ_{p} are the flexural rigidity of the plate, plate's thickness, and mass density of the plate, respectively. $p(x,y,0)$ is the wall pressure due to the fluid loading. For beam-like stiffeners and with displacement continuity relations between the plate and the stiffeners, the force and moment at the interface of the plate

and stiffeners can be written as [66, 68],

$$F_{\mathrm{s}}(x,y) = E_{\mathrm{s}} I_x \frac{\partial^4 W}{\partial y^4}(x,y) - \omega^2 \rho_{\mathrm{s}} A_{\mathrm{s}} W(x,y), \tag{3.2}$$

$$M_{\mathrm{s}}(x,y) = -G_{\mathrm{s}} J_{\mathrm{s}} \frac{\partial^3 W}{\partial x \partial y^2}(x,y) - \omega^2 \rho_{\mathrm{s}} I_0 \frac{\partial W}{\partial x}(x,y), \tag{3.3}$$

in which E_{s}, G_{s}, ρ_{s} and A_{s} are the Young's and Coulomb's modulus, density and the cross section of the stiffener. I_x and I_0 are the moments of inertia, and J_{s} is the torsion constant.

The acoustic pressure $p(x,y,z)$ satisfies:

- The Helmholtz equation in the half space Ω_{f} occupied by the fluid,

$$\nabla^2 p(x,y,z) + k_{\mathrm{f}}^2 p(x,y,z) = 0, \ \forall (x,y,z) \in \Omega_{\mathrm{f}}, \tag{3.4}$$

  where k_{f} is the acoustic wavenumber and ∇ the Nabla operator.

- The Euler equation at the coupling area between plate and the fluid,

$$-\rho_{\mathrm{f}} \omega^2 W(x,y) = -\frac{\partial p}{\partial z}(x,y,0). \tag{3.5}$$

- The Sommerfeld radiation conditions on a fictional infinite surface.

By applying the space-Fourier transform to the above coupled fluid-structure equations we obtain spectral displacement as described in the literature [66], which is given by

$$\widetilde{W}(\mathbf{k}) = \widetilde{W}_0(\mathbf{k}) \Gamma(\mathbf{k}), \tag{3.6}$$

in which, $\widetilde{W}_0(\mathbf{k})$ is the spectral displacement of the plate without the stiffeners, and $\Gamma(\mathbf{k})$ is the stiffeners effects on the plate vibrations, where $\mathbf{k}$ is the wavevector with components k_x and k_y in the x and y directions, respectively. $\widetilde{W}_0(\mathbf{k})$ is given by

$$\begin{cases} \widetilde{W}_0(\mathbf{k}) = \frac{F_0 e^{-\mathrm{j} k_x x_0}}{Z(\mathbf{k})} & \text{if } \sqrt{k_x^2 + k_y^2} \neq k_{\mathrm{f}}, \\ \widetilde{W}_0(\mathbf{k}) = 0 & \text{if } \sqrt{k_x^2 + k_y^2} = k_{\mathrm{f}}, \end{cases} \tag{3.7}$$

where $Z(\mathbf{k})$ is the fluid-loaded plate dynamic stiffness (i.e. force over displacement) which defines the dispersion relation for a fluid-loaded plate, defined by

$$Z(\mathbf{k}) = D\left(k_x^2 + k_y^2\right)^2 - \rho_{\mathrm{p}}\omega^2 h - \mathrm{FL}, \tag{3.8}$$

where $_{\mathrm{f}}$ is the density of the fluid, and FL is the fluid loading contribution given by

$$\mathrm{FL} = \frac{k_{\mathrm{f}}\omega^2}{\sqrt{k_x^2 + k_y^2 - k_{\mathrm{f}}^2}}. \tag{3.9}$$

The stiffeners contribution Γ is defined based on the periodicity of the stiffeners along the plate and described by the following expression

$$\Gamma = \frac{\gamma_1 - \gamma_2 - \gamma_3}{\gamma_4 - \gamma_5}, \tag{3.10}$$

where,

$$\begin{cases} \gamma_1 = \frac{1}{d^2} O_{\mathrm{s}} Z_{\mathrm{s}} S_1 \left(S_1 - \widehat{S}_1\right), \\ \gamma_2 = \left(1 + \frac{1}{d} O_{\mathrm{s}} S_2\right)\left[1 + \frac{1}{d} Z_{\mathrm{s}}\left(S_0 - \widehat{S}_0\right)\right], \\ \gamma_3 = \frac{1}{d} k_x O_{\mathrm{s}}\left[\frac{1}{d} Z_{\mathrm{s}}\left(\widehat{S}_0 S_1 - S_0 \widehat{S}_1\right) - \widehat{S}_1\right], \\ \gamma_4 = \frac{1}{d^2} O_{\mathrm{s}} Z_{\mathrm{s}} S_1^2, \\ \gamma_5 = \left(1 + \frac{1}{d} O_{\mathrm{s}} S_2\right)\left(1 + \frac{1}{d} Z_{\mathrm{s}} S_0\right), \end{cases} \tag{3.11}$$

in which,

$$S_p = \sum_{n\in\mathbb{Z}} \frac{\left(k_x + \frac{2\pi n}{d}\right)^p}{Z\left(k_x + \frac{2\pi n}{d}, k_y\right)}, \quad \widehat{S}_p = \sum_{n\in\mathbb{Z}} \frac{\left(k_x + \frac{2\pi n}{d}\right)^p e^{-\mathrm{j}\frac{2\pi n}{d} x_0}}{Z\left(k_x + \frac{2\pi n}{d}, k_y\right)}, \tag{3.12}$$

directly associated with the stiffener number n and spacing between stiffeners d, with $p = 0, 1, 2$. As suggested by the convergence study presented in [66], the infinite sum is truncated to the interval $n \in [-N, N]$, with $N = 50$. This truncation is justified in the current analysis, given that the geometry of the plate closely resembles that considered in the aforementioned reference. The torsional and flexural dynamic stiffness of the stiffeners are represented by $O_{\mathrm{s}}(k_y)$ and $Z_{\mathrm{s}}(k_y)$ and are described by the following

expressions [66]

$$O_{\mathrm{s}}\left(k_y\right) = G_{\mathrm{s}} J_{\mathrm{s}} k_y^2 - \omega^2 \rho_{\mathrm{s}} I_0, \tag{3.13}$$

$$Z_{\mathrm{s}}\left(k_y\right) = E_{\mathrm{s}} I_x k_y^4 - \omega^2 \rho_{\mathrm{s}} A_{\mathrm{s}}. \tag{3.14}$$

The acoustic pressure in the wavenumber domain is also given by the following expression for each value of z [66]

$$\widetilde{P}\left(\mathbf{k}, z\right) = \widetilde{P}_0\left(\mathbf{k}, z\right) \Gamma\left(\mathbf{k}\right), \tag{3.15}$$

in which

$$\begin{cases} \widetilde{P}_0\left(\mathbf{k}, z\right) = -\frac{k_{\mathrm{f}} \omega^2 F_0 e^{-\mathrm{j}k_x x_0} e^{-\sqrt{k_x^2 + k_y^2 - k_{\mathrm{f}}^2}\, z}}{Z(\mathbf{k}) \sqrt{k_x^2 + k_y^2 - k_{\mathrm{f}}^2}} & \text{if } \sqrt{k_x^2 + k_y^2} \neq k_{\mathrm{f}}, \\ \widetilde{P}_0\left(\mathbf{k}, z\right) = F_0 e^{-\mathrm{j}k_x x_0} & \text{if } \sqrt{k_x^2 + k_y^2} = k_{\mathrm{f}}, \end{cases} \tag{3.16}$$

where $\widetilde{P}_0$ is the spectral pressure of the plate without the stiffeners.

The total acoustic power can be expressed in terms of velocity-only or pressure-only formula by the velocity pressure relation $\widetilde{P}(\mathbf{k}, z) = \frac{k_{\mathrm{f}}\omega}{k_z} \widetilde{V}(\mathbf{k}, z) \mid z = 0$ ([108]), as follows

$$\begin{aligned} \Pi_V &= \frac{k_{\mathrm{f}}\omega}{8\pi^2} \int_{k \in \Omega_a} \frac{1}{k_z} |\widetilde{V}(\mathbf{k})|^2 d\mathbf{k}, \\ \Pi_P &= \frac{1}{8\pi^2 k_{\mathrm{f}}\omega} \int_{k \in \Omega_a} k_z \left|\widetilde{P}(\mathbf{k})\right|^2 d\mathbf{k}, \end{aligned} \tag{3.17}$$

for $\mathbf{k}$ inside the acoustic circle $\left(\Omega_a = \{(k_x,\, k_y) \in \Re^2, \sqrt{k_x^2 + k_y^2} \leq k_{\mathrm{f}}\}\right)$, not considering subsonic waves that do not propagate to the far-field. An inverse discrete Fourier transform (IDFT) can be applied to Eqs. 3.6 and 3.15 to obtain the displacement and pressure fields in the space domain if needed.

3.1.2 Bloch-Floquet propagating waves

The interactions between the flexural motions of the plate and the flexural-torsional motions of the stiffeners, which are periodically spaced, lead to the Bloch-Floquet propagating waves. These waves can be predicted by finding the roots ($\mathbf{k}^{\mathrm{BF}}$) of the denominator

of the stiffener's influence Γ, as expressed by [68]

$$\Delta\left(\mathbf{k}^{\mathrm{BF}}\right) = \gamma_4\left(\mathbf{k}^{\mathrm{BF}}\right) - \gamma_5\left(\mathbf{k}^{\mathrm{BF}}\right) = 0, \tag{3.18}$$

if $(\mathbf{k}^{\mathrm{BF}})$ are real, the free waves can propagate through the plate without attenuation.

As indicated by previous studies [59, 68, 77] explicit expressions for $(\mathbf{k}^{\mathrm{BF}})$ cannot be derived when fluid loading is considered in the formulation. To overcome this limitation an algorithm was proposed by [68] to compute real values for $(\mathbf{k}^{\mathrm{BF}})$ such that the denominator $(\gamma_4(\mathbf{k}^{\mathrm{BF}}) - \gamma_5(\mathbf{k}^{\mathrm{BF}}))$ is lower than a specific tolerance. The procedure is presented by the flowchart in Fig. 3.2, and it is detailed in Ref. [68]. The aim is to find the roots of $\Delta\left(\mathbf{k}^{\mathrm{BF}}\right)$ which maximises the displacement $\widetilde{W}$ inside of the first Brillouin zone, it is possible to extract the minimum of the $\Delta\left(\mathbf{k}^{\mathrm{BF}}\right)$ indicated by $\Delta_{\min}\left(k_y^i\right)$. The latter, is compared to the tolerance to determine if it is propagating BF wave or not. After this process, the obtained k_y^i BF waves are then matched with the associated k_x^{BF}, with this, the BF wavenumber can be obtained, and by comparing to the acoustic wavenumber (k_{f}) it can be determined if the BF wavenumber is radiating to the far-field or not.

3.1.3 Contribution of Bloch-Floquet waves to the vibroacoustic response

To investigate the effect of the BF waves on the vibroacoustic response of the stiffened plate, first, we need to identify the frequency bands where a set of waves propagating along the plate (passbands) and the frequency bands outside passbands (stopbands) where waves are strongly attenuated across the plate corresponding to a set of evanescent waves. The BF passbands are obtained according to the procedure presented in Fig. 3.2, which is based on the algorithm in the literature [68], considering the tolerance to be $\epsilon = 0.05$ and also the material and geometrical properties presented in Table 3.1. For illustration, in Appendix B, an interactive plot showing the spectral displacement in function of the frequency is proposed. It highlights that the highest values of the spectral displacements (in red) are obtained for the wavenumbers k_y corresponding to the k_y^{BF} wavenumbers (symbolised with a white circle on the k_y axis), which have been extracted with the process described in the previous subsection.

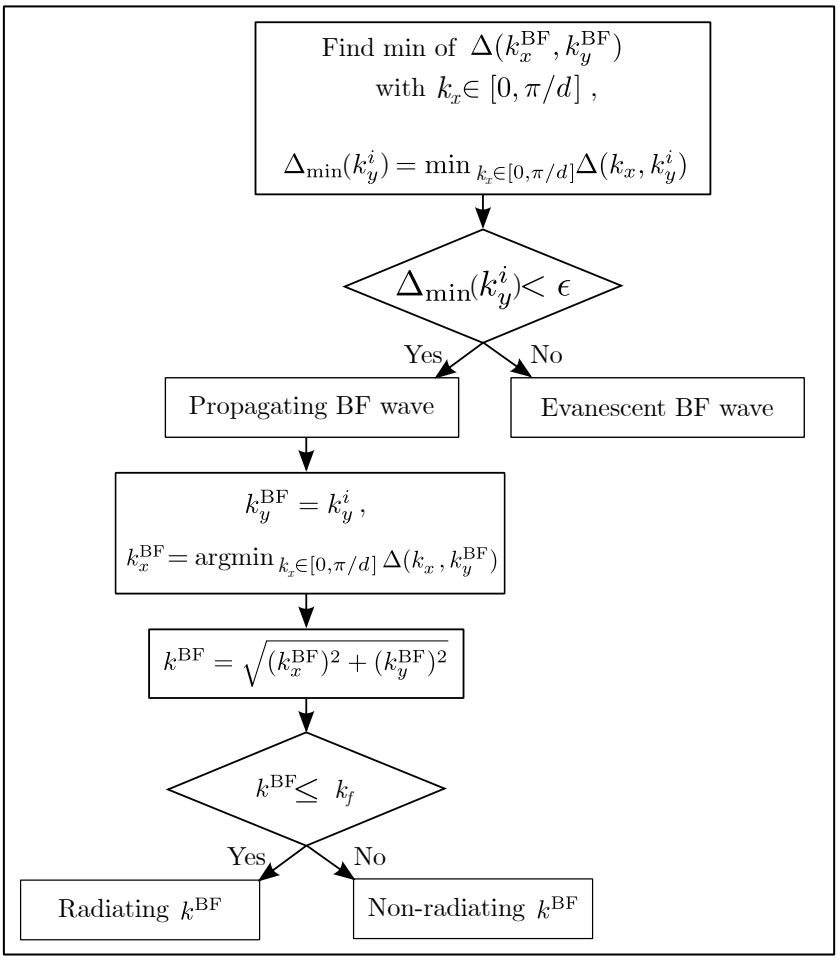

FIGURE 3.2: Algorithm to obtain the BF propagating waves described in Ref. [68].

The propagating k^{BF} are shown in Fig. 3.3 by black dots as a function of frequency. The solid blue line represents the acoustic wavenumber. Those propagating BF waves below the acoustic wavenumber are supersonic waves which are radiating to the far-field. The corresponding frequency bands for these radiating BF waves are indicated by the red dots on the x-axis. These BF radiating frequency ($\mathrm{BF}_{\mathrm{rad}}$) bands are also shown as a red-shaded area in Figs. 3.7 and 3.11.

3.2 Non-negative intensity formulation

In this section, an analytical formulation is presented for NNI in the wavenumber domain for the plate under harmonic point excitation to identify the areas of the vibrating structure that produce radiation to the far-field. The aim here is to develop a formula for $I^{\mathrm{N}}(\mathbf{x})$ which meets the two following conditions:

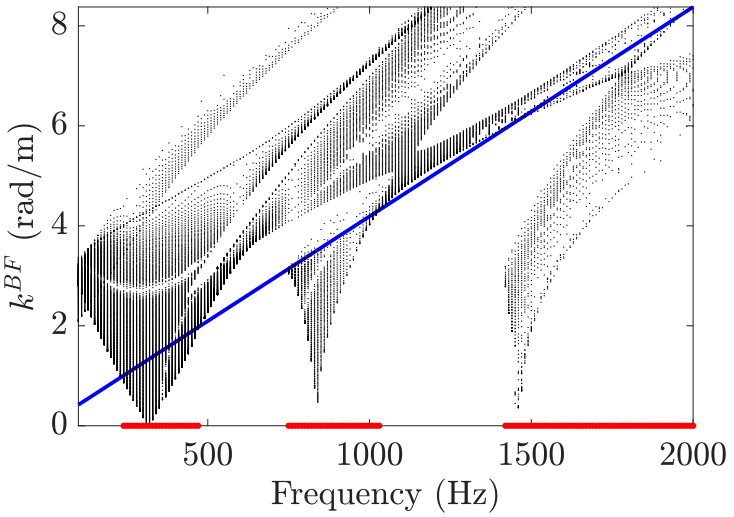

FIGURE 3.3: Amplitude of the BF wavenumber k^{BF} in function of frequency (black dots) and $\mathrm{BF}_{\mathrm{rad}}$ (red dots) corresponding to frequency such that $k^{\mathrm{BF}} < k_{\mathrm{f}}$, in which k_{f} is represented by the blue line.

1. The NNI must be always non-negative. This will prevent acoustic short-circuit in the adjacent areas on the surface of the structure.

2. When integrating the NNI over the boundary surface, it must produce the total sound power.

To meet the first condition, the NNI can be defined as follows [110]

$$I^{\mathrm{N}}(\mathbf{x}) = \frac{1}{2}\beta^*(\mathbf{x})\beta(\mathbf{x}), \tag{3.19}$$

in which $\beta(\mathbf{x})$ is a parameter without physical significance. It has been introduced to ensure that the NNI is always non-negative by definition. The second condition for the NNI states that the total radiated acoustic power must be obtained by integrating the NNI over the boundary surface, therefore we have

$$\Pi = \int_A I^{\mathrm{N}}(\mathbf{x}) d\mathbf{x} = \frac{1}{2}\int_A \beta(\mathbf{x})\beta^*(\mathbf{x})\, d\mathbf{x}. \tag{3.20}$$

It is possible to establish the relation between Eq. 3.20 and the two formulations for sound power in Eq. 3.17 to find β that satisfies Eq. 3.20 for velocity and pressure-only

as given by

$$\beta_v = \frac{\sqrt{\rho_f \omega}}{4\pi^2} \int_{k\in\Omega_a} \frac{1}{\sqrt{k_z}} \widetilde{V}(\mathbf{k}) e^{\mathrm{j}\mathbf{kx}} d\mathbf{k}, \tag{3.21}$$
$$\beta_p = \frac{1}{4\pi^2 \sqrt{\rho_f \omega}} \int_{k\in\Omega_a} \sqrt{k_z} \widetilde{P}(\mathbf{k}) e^{\mathrm{j}\mathbf{kx}} d\mathbf{k}.$$

Substituting Eq. 3.21 in Eq. 3.19, the two expressions for NNI are given by

$$I_V^{\mathrm{N}} = \frac{\rho_f \omega}{32\pi^4} \left| \int_{k\in\Omega_a} \frac{1}{\sqrt{k_z}} \widetilde{V}(\mathbf{k}) e^{\mathrm{j}\mathbf{kx}} d\mathbf{k} \right|^2, \tag{3.22}$$

$$I_P^{\mathrm{N}} = \frac{1}{32\pi^4 \rho_f \omega} \left| \int_{k\in\Omega_a} \sqrt{k_z} \widetilde{P}(\mathbf{k}) e^{\mathrm{j}\mathbf{kx}} d\mathbf{k} \right|^2. \tag{3.23}$$

In Eq. 3.22 the term in the denominator tends to zero when integrating on the acoustic circle, resulting in a singular integral. It is possible to remove this singularity in the integral analytically as proposed in Ref. [34].

3.3 Results and discussion

The following results are based on the material and geometrical properties presented in Table 3.1. A MATLAB code was generated based on the formulation in the previous sections and it was used for numerical analyses. To verify the presented formulation, the vibration results were compared to those presented by Mace [60] for a fluid-loaded/unloaded infinite stiffened plate, both excited by a point force on the stiffener. Figs. 10 and 11 in Ref. [60] have been digitalised for the comparison. The results are shown in Fig. 3.4, comparing the input mobility for the present formulation and Mace's, showing good agreement with this well established formulation. This verification confirms the accuracy and reliability of the proposed formulation and MATLAB code.

To show the contribution of BF waves on the plate response, a comparison is made between an unstiffened and two cases of a stiffened fluid-loaded plate. The stiffened fluid-loaded plate is considered to be under point force at $x_0 = 0$ m and $x_0 = 0.5$ m, representing excitation on the stiffener and between stiffeners, respectively.

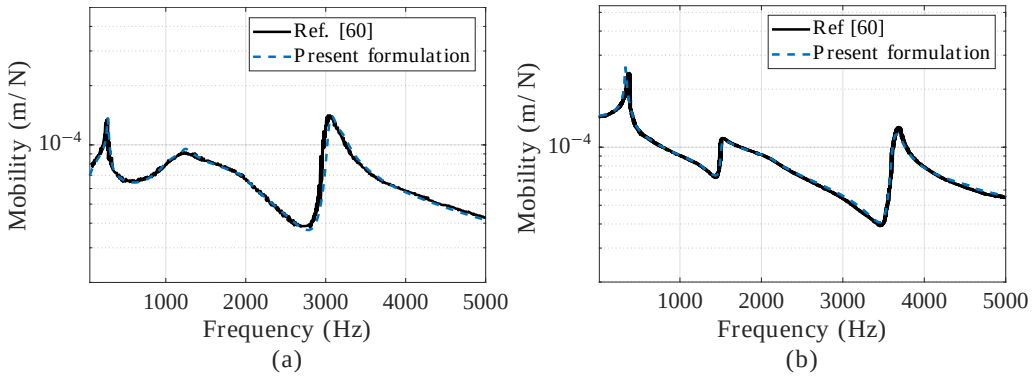

FIGURE 3.4: Input mobility for a frequency range with respect to the two cases presented in [60]. Infinite stiffened structure with the point excitation on the stiffener (a) with fluid loading, and (b) without fluid loading. Present formulation is represented by the blue dashed line, and the response from Ref. [60] by the black solid line.

First, let us consider six distinct frequencies of 350 Hz, 450 Hz, 550 Hz, 650 Hz, 750 Hz and 850 Hz. This range comprises the transition from a $\mathrm{BF}_{\mathrm{rad}}$ to a non-radiating band, and towards a $\mathrm{BF}_{\mathrm{rad}}$ band again. The first two frequencies, 350 Hz and 450 Hz are inside the $\mathrm{BF}_{\mathrm{rad}}$ band, the following two 550 Hz and 650 Hz are inside a non-radiating band, and the last two frequencies, 750 Hz and 850 Hz are again inside the $\mathrm{BF}_{\mathrm{rad}}$ band. Figs. 3.5 and 3.6 shows the wavenumber spectrum of the plate velocity at these six frequencies, considering the excitation on the stiffener and between the stiffeners, respectively. The acoustic circle is described by a solid white line at the center of each map, highlighting the well established concept that the only the waves inside of it will radiate to the far-field. The propagation zones are the red marks on the sides of the map, along the k_y-axis. The map shows with green to red the regions of high velocity amplitudes which are located within the propagation zones. The wavenumbers for the flexural and torsional motions of the stiffeners are marked by the horizontal white dashed and dashed-dot lines, respectively. The fluid-loaded plate natural flexural circle is represented by the white dotted line.

When comparing the results from Figs. 3.5 and 3.6, it can be noticed that the areas of interactions between the torsional and flexural motion of the stiffeners and the plate ("oscillating lines" between the horizontal white lines) have higher amplitude in the case with the excitation on stiffener (Fig. 3.5), explaining why the effect of the BF waves is more noticeable when the excitation force is placed on stiffeners. When the excitation is on stiffener, at the frequencies within the $\mathrm{BF}_{\mathrm{rad}}$ band (see Fig. 3.5(a), (b),

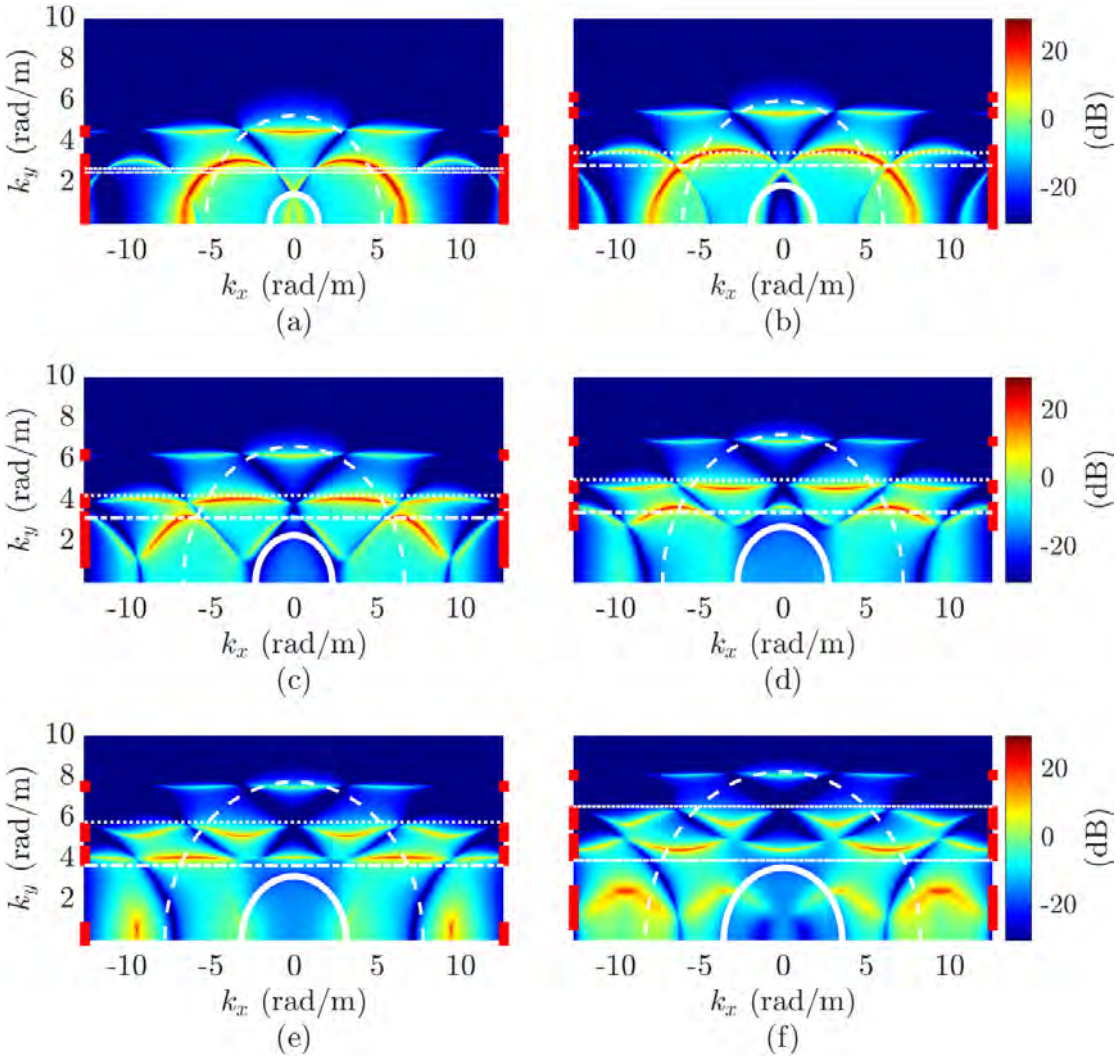

FIGURE 3.5: Wavenumber spectrum of the plate velocity with excitation on stiffener ($x_0 = 0$ m) for, (a) 350 Hz, (b) 450 Hz, (c) 550 Hz, (d) 650 Hz, (e) 750 Hz and (f) 850 Hz. (dB, ref 1 μm.s^{-1}). Propagation zones are indicated by a red mark on the k_y-axis. The wavenumbers for the flexural and torsional motions of the stiffeners are marked by the horizontal white dashed and dashed-dot lines, respectively. The fluid-loaded plate natural flexural circle is represented by the white dotted line.

(e) and (f)), the waves inside the acoustic circle present a relative high contribution, from green to yellow in comparison to the response for the cases outside the radiating band (Fig. 3.5(c) and (d)) where there is a predominant blue color inside the acoustic circle. This is consistent with Fig. 3.7(b) which shows high radiated sound power at the radiating bands that is directly proportional with the sum of the square of spectral velocity in the acoustic circle as indicated by Eq. 3.17. It can be seen from Fig. 3.6(c) and (d) that when the excitation force is between stiffeners, the area inside the acoustic circle is green and this explains why the sound power for this case at these frequencies is relatively high as shown in Fig. 3.7(b). Further results are provided by the interactive

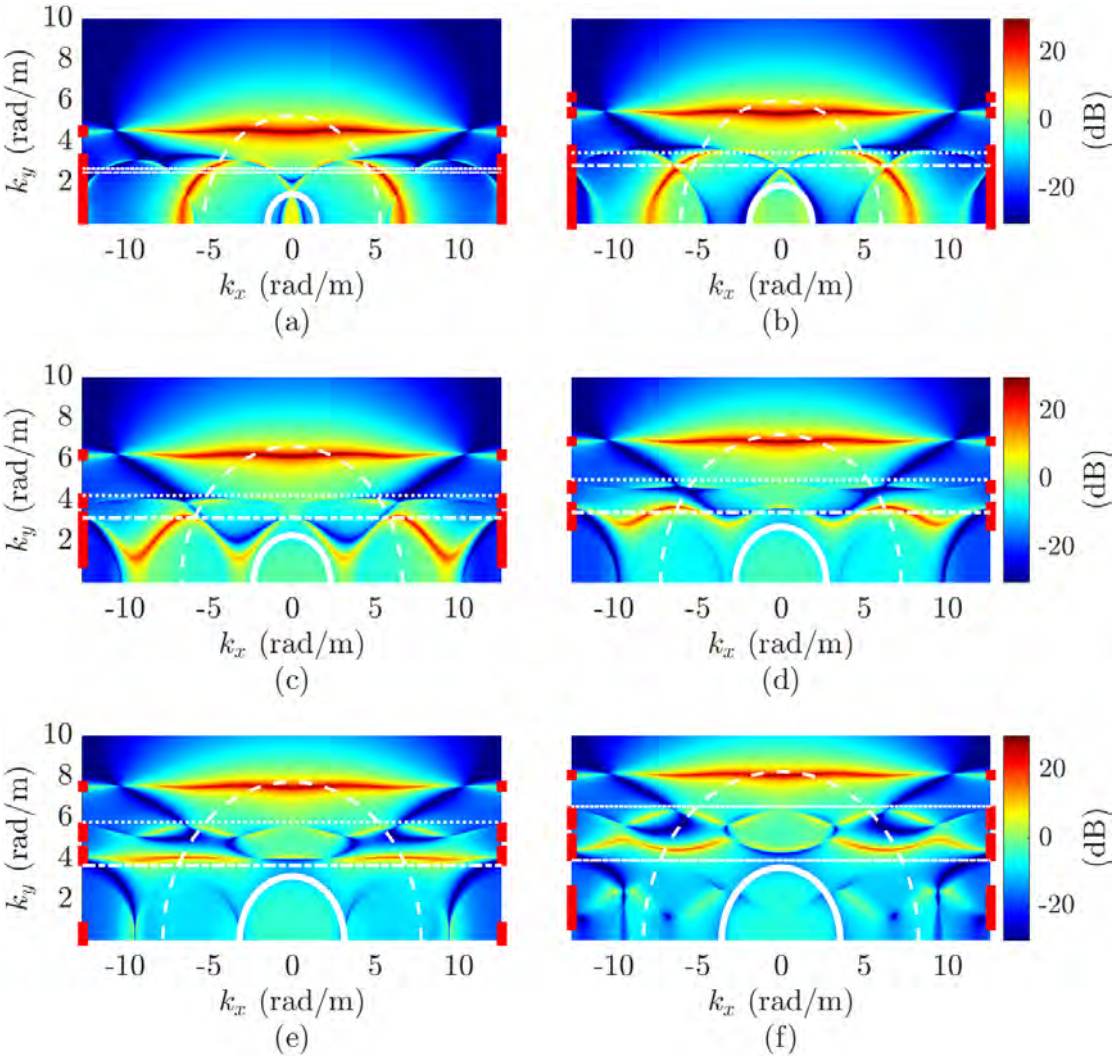

FIGURE 3.6: Wavenumber spectrum of the plate velocity with excitation between stiffeners ($x_0 = 0.5$ m) for, (a) 350 Hz, (b) 450 Hz, (c) 550 Hz, (d) 650 Hz, (e) 750 Hz and (f) 850 Hz. (dB, ref 1 μm.s^{-1}). Propagation zones are indicated by a red mark on the k_y-axis. The wavenumbers for the flexural and torsional motions of the stiffeners are marked by the horizontal white dashed and dashed-dot lines, respectively. The fluid-loaded plate natural flexural circle is represented by the white dotted line.

maps in Appendix A.1 Fig. A.1, being possible to see the transition between the radiating bands. This is consequently observed in the response for the sound power and radiation efficiency, presenting higher amplitudes when the excited frequency is inside a $\mathrm{BF}_{\mathrm{rad}}$ band, as shown in Fig. 3.7.

Fig. 3.7 shows the sum of the quadratic velocity (AV^2), the sound power response (Π), and the radiation efficiency (σ). The sum of the quadratic velocity can be estimated using, $AV^2 = \frac{1}{8\pi^2}\int_{-\infty}^{\infty}\left|\widetilde{V}\left(\mathbf{k}\right)\right|^2 d\mathbf{k}$, in which the infinite sum is approximated by truncating the wavenumber space as detailed in Refs. [66, 68]. The radiation efficiency can

be obtained by $\sigma = \frac{\Pi}{\rho_f c_f A_p V^2}$ [108].

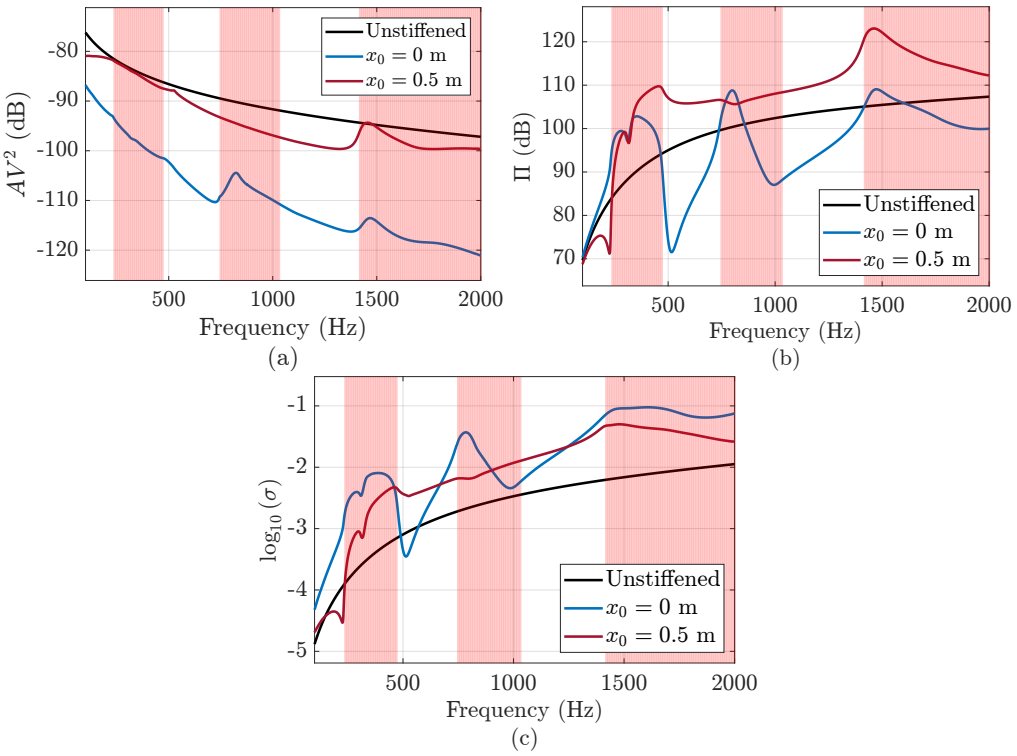

FIGURE 3.7: Comparison between unstiffened and stiffened plates excited by a point force at x_0, in (a) the sum of the quadratic velocity (AV^2), (b) sound power (Π), and (c) radiation efficiency (σ).

From Fig. 3.7 it can be seen that the vibroacoustic response of the unstiffened plate is a smooth curve compared to the stiffened system. It is known that the addition of the periodic stiffeners introduces so-called stopbands and passbands in the response [59]. For example, some peaks in the response of the stiffened plate can be observed around frequencies of 350 Hz, 800 Hz, 1460 Hz, which are located in a $\mathrm{BF_{rad}}$ band, and some troughs (outside the $\mathrm{BF_{rad}}$ band) occur approximately at 500 Hz and 1000 Hz. As shown in Fig. 3.7(a), adding stiffeners to the plate increases the total stiffness of the system and results in a decrease of the surface velocity. However, this addition significantly increases the sound power in the $\mathrm{BF_{rad}}$ band and leads to a considerable increase of the radiation efficiency in almost the entire considered frequency range.

Comparing the two excitation cases, it can be observed that the excitation between stiffeners leads to a higher vibroacoustic response in most frequencies compared to the response of the system due to the excitation on the stiffener. Fig. 3.7(a) shows that when the excitation force is on the stiffener, the vibration of the plate is always lower than that of the plate excited in between the stiffeners. Moreover, for the latter case,

the influence of the $\mathrm{BF}_{\mathrm{rad}}$ bands is insignificant on the radiated power response, as shown in Fig. 3.7(b). This has caused a notable difference between the radiated sound power generated by the two types of excitations. For example, a discrepancy of almost 35 dB can be seen around 500 Hz between the two predicted sound power responses. Fig. 3.7(c) indicates that the radiation efficiency is higher when the excitation force is on the stiffener except outside the $\mathrm{BF}_{\mathrm{rad}}$ bands. For both cases, the sound power peaks are inside the $\mathrm{BF}_{\mathrm{rad}}$ bands, but evidently, this behaviour is more noticeable when the excitation is on the stiffener. It should be noted that in many engineering applications utilising stiffened structures, the excitation force is located on the stiffeners. It has been reported in the literature that the peaks in the passbands are related to the BF propagating waves, which can contribute most to the radiated sound power, resulting in a higher amplitude in the sound power response [68]. Therefore, the use of the NNI for these pass and stopbands are the focus of our analysis in the next section.

3.3.1 Surface contribution identification using non-negative intensity

To further study the generation of BF waves in the heavy fluid-loaded stiffened plate and their radiation to the far-field, let us consider the same six distinct frequencies of 350 Hz, 450 Hz, 550 Hz, 650 Hz, 750 Hz and 850 Hz. Fig. 3.8 compares the maps of NNI (I^{N}) with those for the active intensity (I_{act}) for the stiffened plate at six distinct frequencies (including the transition between the first and second radiating band) for the excitations on or between the stiffeners. The active intensity is given by [108], $I_{\mathrm{act}} = \Re\left[\frac{1}{2}P(\mathbf{x})V(\mathbf{x})\right]$, in which, P and V are the acoustic pressure and fluid particle velocity at the plate surface. To observe the effect of stiffeners on the energy distribution, the results are also compared with the intensity maps for the unstiffened plate. The maps are plotted over an area of 10 m $\times$ 10 m. All the maps are presented with the same dynamic range of 60 dB.

It can be observed from Fig. 3.8 that hot spots at the surface of the stiffened plate cannot be accurately identified by the active acoustic intensity due to its bipolar nature [34]. However, since NNI is always positive, it prevents acoustic short circuit at the surface of the plate and provides a clear map of the local areas which are contributing to the radiated sound power. The NNI maps show that at frequencies 350 Hz, 450 Hz, 750 Hz and 850 Hz, considering $x_0 = 0$ m, there is a great spread of intensity over the surface,

resulting in a higher sound power which is consistent with the results in Fig. 3.7. It is evident that the majority of the acoustic energy is dispersed in the normal direction to the stiffeners within the BF radiating bands. Further results are provided by the interactive maps in Appendix A.2 Fig. A.2. For the first frequencies of the BF radiating frequency band, it is noticeable that the energy is spreading in the direction normal to the stiffeners, however for the last frequencies of the BF band, it tends to spread in the direction of the stiffeners. Additionally, it was discovered that the NNI is not only confined to the region enclosed by the two stiffeners adjacent to the excitation, proving that the vibrations responsible for the far-field noise are those that have propagated through the stiffeners. The NNI presents a distinct pattern of distribution of energy in periodic arcs that are dissipated when moving away from the source. However, outside these frequency passbands, the surface contributions of the stiffened plate are similar to that of the unstiffened plate (6th row of Fig. 3.8) where the energy is concentrated at the excitation location as can be seen from Fig. 3.8(c), (d).

Considering the point force in between stiffeners ($x_0 = 0.5$ m), only at low frequency radiating band where there is a distinct peak in the sound power response (see Fig. 3.7), the propagation of the BF waves is exhibited as high-intensity area normal to the stiffeners. This behaviour is noticed only at lower frequencies (the first $\mathrm{BF_{rad}}$ band), thenceforth the NNI pattern becomes similar to an unstiffened plate, presenting a circular pattern around the excitation source. Even though the excitation frequency is outside the $\mathrm{BF_{rad}}$ band, there is a large spread of the NNI across the plate significantly higher than the ones from the case with the applied force on stiffener.

For the following $\mathrm{BF_{rad}}$ band (Figs. 3.8(e),(f)) is possible to see small hot spots following the stiffener's lines, or in between again, showing that however the response is not dictated by the BF propagating waves they are still influential in the radiation. This can be seen with more details in the interactive plot in Appendix A.2 Fig. A.3. According to these figures, NNI results can provide important information on the BF wave propagation and help us visualise and understand its relation with the radiated sound power.

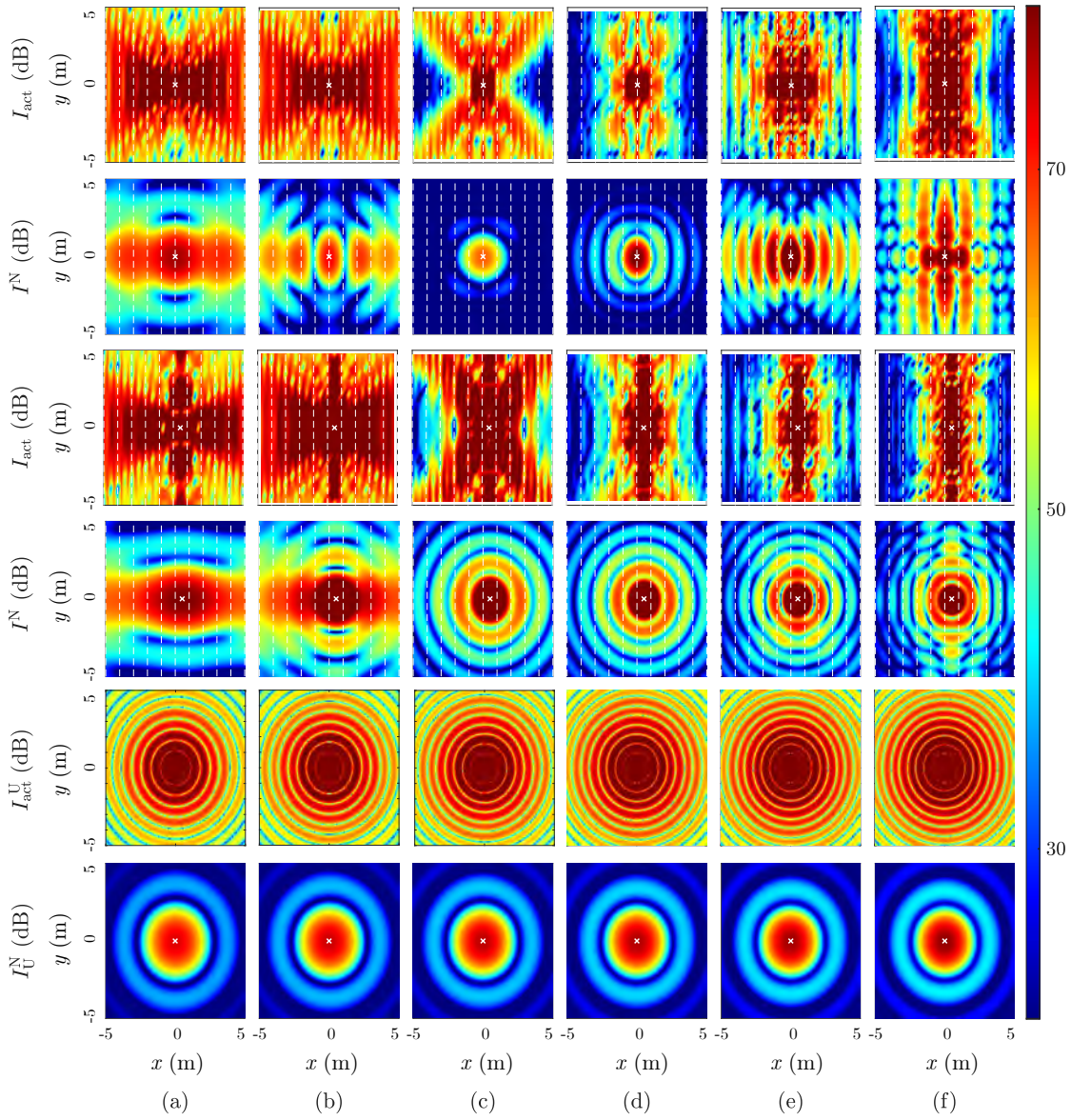

FIGURE 3.8: Maps of I_{act}, I^N, I^U_{act} and I^N_U considering the plate with excitation at $x_0 = 0$ m (1st and 2nd rows), $x_0 = 0.5$ m (3rd and 4th rows) and the unstiffened plate (5th and 6th rows). The maps shows a 10 m $\times$10 m of the infinite plate, for (a) 350 Hz, (b) 450 Hz, (c) 550 Hz, (d) 650 Hz, (e) 750 Hz and (f) 850 Hz. Stiffener's lines and the point force position (x_0) are presented as white dashed lines and white x mark, respectively.

3.3.2 Non-negative intensity distribution with respect to the force position

By varying the point force position from $x_0 = 0$ m (on the stiffener) to $x_0 = 0.5$ m (in between the stiffeners), as shown in the previous sections, the NNI pattern becomes similar to an unstiffened plate, and the distribution of energy is concentrated at the excitation position. Fig. 3.9 presents the transitional behaviour of the stiffened plate

in terms of the sum of the quadratic velocity, sound power, and radiation efficiency when the point force excitation moves from $x_0 = 0$ m to $x_0 = 0.5$ m for the highlighted frequencies. Fig. 3.9(a) shows that plate average velocity increases as the excitation force is moved away from the stiffener at all considered frequencies except at 850 Hz where it is diminished for $x_0 > 0.3$ m. A more complex trend can be observed in the sound power and radiation efficiency as shown in Fig. 3.9(b) and (c), where the variation of these acoustic parameters is clearly dependent on the frequency of excitation and the fact that whether it is in a passband or a stopband. For example, the sound power variation with respect to the force position at 350 Hz is similar to that of 450 Hz, presented by the dark blue and orange lines, as these frequencies are located in the first $\mathrm{BF_{rad}}$ band. This also holds true for the results at the second passband (750 Hz and 850 Hz).

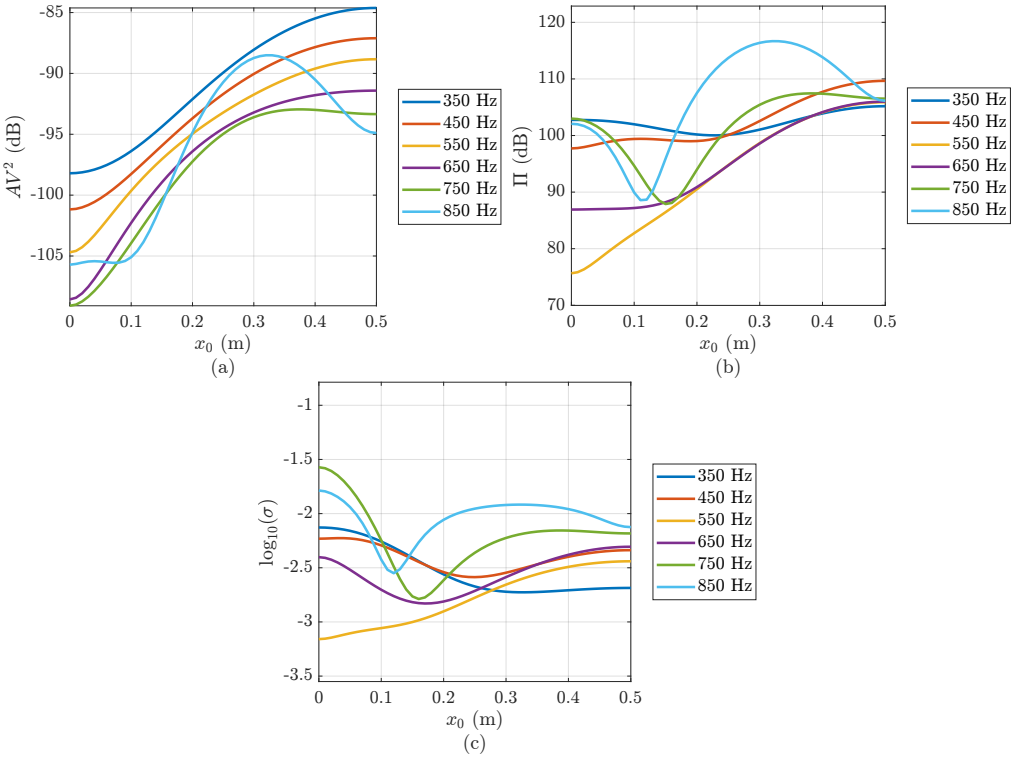

FIGURE 3.9: (a) Sum of the quadratic velocity (AV^2), (b) sound power (Π), and (c) radiation efficiency (σ) as a function of excitation position for different frequencies. $x_0 = 0$ m, and $x_0 = 0.5$ m denote on and in between the stiffeners excitation, respectively.

Fig. 3.10 presents the variation of NNI distribution with respect to the force position for the six distinct frequencies, presenting the transition between on stiffener to between stiffeners (i.e. $0.5 \text{ m} > x_0 > 0$ m). The maps show that if the excitation frequency is outside a $\mathrm{BF_{rad}}$ band, the energy is concentrated at the point force position. Moreover,

at the second stopband (550 Hz and 650 Hz), the more the force is moved away from the stiffener, the larger the NNI distribution becomes over the plate surface. This means a higher radiated sound power, as shown in Fig. 3.9(b). At frequencies of 750 Hz and 850 Hz (in the passband), it is noted that NNI distribution becomes smaller as the force is moved from $x_0 = 0$ m (Fig. 3.8) to $x_0 = 0.1$ m, and it then gradually becomes greater and covers a large surface area when the force is at $x_0 = 0.3$ m. This means the plate's radiated sound power reaches its maximum value, as shown in Fig. 3.9(b) for this force position. The NNI distribution and the vibroacoustic response of the stiffened plate at 550 Hz and 750 Hz, which are respectively inside and outside a $\mathrm{BF}_{\mathrm{rad}}$ band, can be examined in more detail in the interactive plot in Appendix D.

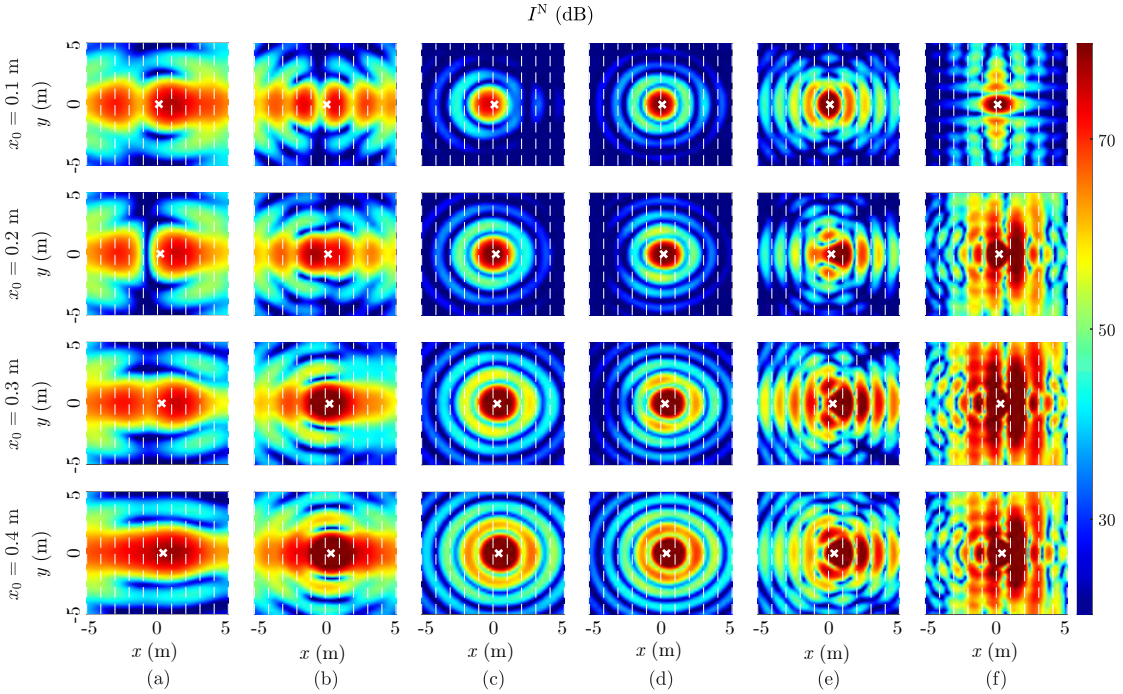

FIGURE 3.10: Maps of I^{N} for (a) 350 Hz, (b) 450 Hz, (c) 550 Hz, (d) 650 Hz, (e) 750 Hz and (f) 850 Hz, varying the point force position from $x_0 = 0.1$ m to $x_0 = 0.4$ m. Stiffener's lines and the point force position (x_0) are presented as white dashed lines and white x mark, respectively.

3.3.3 Non-negative intensity distribution with respect to the damping

It was shown that NNI presents significant values in a large spatial domain for the passbands, highlighting the propagation of waves that contribute to the sound power. In contrast, for the stop bands, NNI presents significant values only close to the excitation location, highlighting that the main source contribution to the sound power is not related

to the wave propagation (but to the excitation itself). This information given by the NNI suggests that if we increase the damping (which leads to the attenuation of the propagative waves), a significant reduction of the sound power will only be noticed in the frequency band for which a spread of NNI has been observed. To verify this statement, results for different dampings are presented and analysed in this section.

Let us consider a change in the plate and stiffener's structural damping by changing the loss factor (η) from $\eta = 2\%$ to $\eta = 10\%$. Fig. 3.11 presents the sound power response for $\eta = 2\%$ and $\eta = 10\%$ considering the excitation on the stiffener ($x_0 = 0$ m) and between stiffeners ($x_0 = 0.5$ m). The $\mathrm{BF}_{\mathrm{rad}}$ is represented by the vertical red lines. Fig. 3.11(a) shows that the high structural damping lowers the peaks at the passbands but not at the stopbands. The same behaviour can be observed by considering the force at $x_0 = 0.5$ m as presented by Fig. 3.11(b).

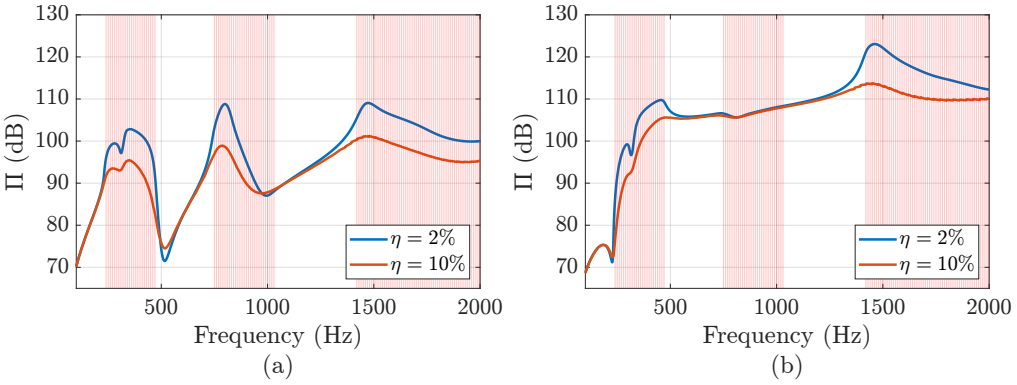

FIGURE 3.11: Sound power (Π) response considering, (a) excitation on stiffeners ($x_0 = 0$ m), and (b) excitation between stiffeners ($x_0 = 0.5$ m), for $\eta = 2\%$ and $\eta = 10\%$. The $\mathrm{BF}_{\mathrm{rad}}$ is represented by the vertical red lines.

Figs. 3.12 and 3.13 present the comparison of the NNI distribution for the six distinct frequencies considering $\eta = 2\%$ and $\eta = 10\%$, with respect to the point force on the stiffener ($x_0 = 0$ m) and between stiffeners ($x_0 = 0.5$ m), respectively. As Fig. 3.12 presents, only frequencies inside passbands (Fig. 3.12(a), (b), (e) and (f)) have significant attenuation when comparing the response from $\eta = 2\%$ to $\eta = 10\%$, which is consistent with the sound power results in Fig. 3.11. As expected, the energy is mitigated as it moves away from the source, but when the excitation frequency is in a stopband, the energy is mainly focused on the source location, and there is no significant change in the NNI distributions. The same behaviour is present considering the excitation in between stiffeners ($x_0 = 0.5$ m) as shown by Fig. 3.13. The NNI distribution shows that if the

energy is already concentrated at the source location, increasing the damping will not have a significant effect on dissipating the energy. This can be observed in the second passband (750 Hz and 850 Hz) considering the excitation between stiffeners, in which the energy was concentrated at the source location with a similar pattern to an unstiffened plate and as stopbands, as mentioned before.

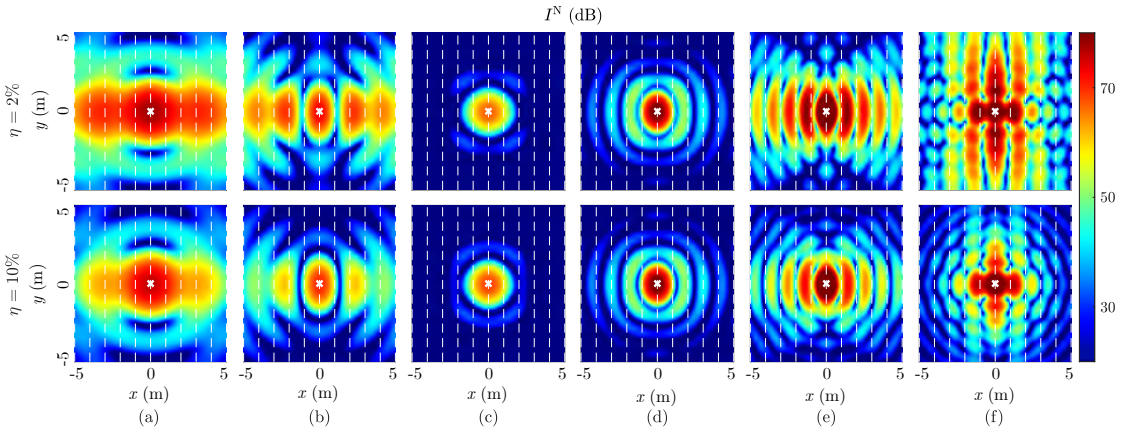

FIGURE 3.12: Maps of I^{N} for (a) 350 Hz, (b) 450 Hz, (c) 550 Hz, (d) 650 Hz, (e) 750 Hz and (f) 850 Hz, with the point force position at $x_0 = 0$ m. Stiffener's lines and the point force position (x_0) are presented as white dashed lines and white x mark, respectively.

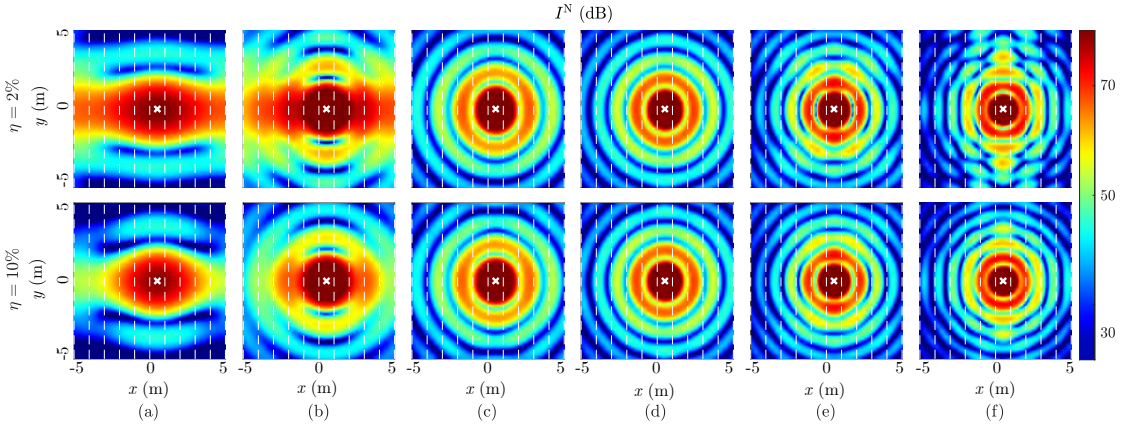

FIGURE 3.13: Maps of I^{N} for (a) 350 Hz, (b) 450 Hz, (c) 550 Hz, (d) 650 Hz, (e) 750 Hz and (f) 850 Hz, with the point force position at $x_0 = 0.5$ m. Stiffener's lines and the point force position (x_0) are presented as white dashed lines and white x mark, respectively.

3.4 Summary

An analytical formulation of the NNI for an infinite heavy fluid-loaded plate with periodic stiffeners was proposed. It allowed us to study the NNI maps in regard to the panel

vibroacoustic response. The effects of stiffeners on the vibration response and radiated sound power were initially demonstrated, and associated BF radiating frequencies were identified. To identify the surface areas on the stiffened plate associated with the propagation of BF waves contributing to the radiated sound power, colour maps of NNI were compared considering the different excitation cases to those from the unstiffened plate. Frequencies inside and outside the BF radiating frequency bands were considered.

It was found that when the frequency is inside a BF radiating frequency band, the NNI is widely distributed on the plate, regardless of the excitation position. Moreover, the intensity is spreading in the direction normal to the stiffeners for the first frequencies of the BF radiating frequency band, whereas it tends to spread toward the direction of the stiffeners for the last frequencies of the BF band. Furthermore, it was observed that the area for which the NNI is significant is not limited to the area bounded by the two stiffeners close to the excitation, which indicates that the vibrations inducing the radiated noise in the far-field are due to the propagation through the stiffeners. For frequencies outside the BF radiation frequency band, the NNI is concentrated close to the excitation point and the vibrations responsible for the radiated noise do not result from wave propagations. It was also noticed that the hot spots on the plate were larger when the excitation was between stiffeners than that on the stiffener. This may explain why the plate radiates significantly more when the excitation is between two stiffeners at these frequencies. Moreover, the large spread of the NNI spots for BF radiating frequencies compared to non-BF radiating frequencies expressed well that the plate radiates more for the former frequencies than for the latter ones.

It was also shown that increasing the structural damping can reduce the NNI distribution over the plate surface at BF radiating frequencies and decrease the radiated sound power, while this effect is negligible outside the BF radiating frequencies. This agrees with the fact that the vibrations inducing the radiated noise in the far-field are due to wave propagations, that is why increasing damping can then attenuate the radiated sound power for BF radiating frequencies. This study has shown that NNI is an efficient tool for identifying the surface contribution to the noise radiation in the far-field for stiffened structures. The proposed process is an efficient computational technique allowing one to do a parametric survey on different stiffened panel cases.

Chapter 4

Semi-analytical formulation for vibroacoustic response of a heavy fluid-loaded plate with ABH stiffeners

This chapter focuses on the semi-analytical formulation and analysis of the vibroacoustic response of a heavy fluid-loaded plate with ABH stiffeners. The theoretical development of the model is presented in Section 4.1, where the vibroacoustic response of the system is modelled in the wavenumber domain. This approach facilitates efficient and accurate calculations, enabling a comprehensive analysis of the system's behaviour.

The theoretical formulation in Section 4.1 begins with the equations of motion for a fluid-loaded plate with ABH stiffeners. The stiffeners are characterised by their dynamic stiffness, which is obtained through FEM simulations (Section 4.1.2). These dynamic properties are coupled with the analytical model of the fluid-loaded plate, allowing for precise predictions of the spectral displacement and radiated pressure.

The chapter investigates the effectiveness of ABH stiffeners in mitigating vibroacoustic responses compared to conventional rectangular stiffeners. Section 4.2 details the investigation of the addition of damping damping layers in both stiffeners and the variation of the distance between stiffeners on the vibroacoustic behavior of the plate. The role

of Bloch-Floquet waves in creating passbands and stopbands is also explored, with a focus on how ABH stiffeners can reduce these effects. The findings highlight the significant reductions in mean quadratic velocity and radiated sound power when comparing ABH stiffeners against traditional rectangular stiffeners, particularly within identified passbands.

This chapter is based on the article "Semi-analytical formulation to predict the vibroacoustic response of a fluid-loaded plate with ABH stiffeners", published in the journal *Thin-Walled Structures* [64].

4.1 Semi-analytical formulation

In this section, we introduce a semi-analytical formulation to model the vibroacoustic response of an infinite heavy-fluid loaded plate with ABH stiffeners. While the formulation can be applied to stiffeners with various cross-sections, as they are represented by a FEM, our focus is predominantly on exploring its applicability and effectiveness in the context of ABH stiffeners. The schematic diagram of the system is shown in Fig. 4.1, where, a 2D periodically distributed array of identical stiffeners is coupled with an infinite heavy fluid-loaded thin plate extending along the x-axis. $x = nd$ and n is an integer ($\mathbb{Z}$) indicating the stiffener's number, and d is the distance between them, as shown in Fig. 4.1. The stiffeners are assumed to have rigid connections with the plate. The plate of thickness h is considered to be excited by a point force F_0 at a position (x_0), and it is in contact with a fluid on one side in the half space Ω. Herein, the thickness h is set to 0.010 m. For the two cases considered in air (light fluid) and in water (heavy fluid), the fluid density ρ_f and sound speed c_f are 1.225 kg/m^3 and 353 m/s for air, and 1000 kg/m^3 and 1500 m/s for water, respectively.

For the purposes of the following developments, let us omit the harmonic time dependence represented by $e^{\mathrm{j}\omega t}$, where ω is the excitation frequency in rad/s and j is the imaginary unit. Considering the Love-Kirchhoff assumptions, the equation of motion of the fluid loaded stiffened plate can be written as [66],

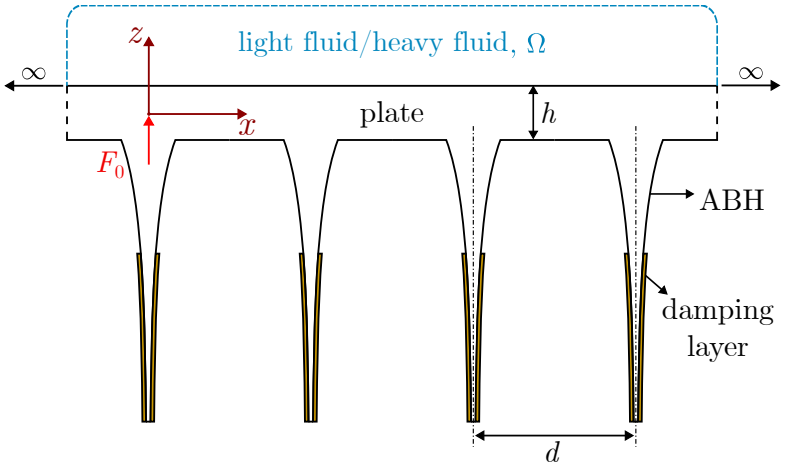

FIGURE 4.1: Schematic of an infinite heavy fluid-loaded plate with periodic ABH stiffeners.

$$
\begin{aligned}
D\nabla^4 W(x,\omega) - \omega^2 \rho_{\mathrm{p}} h W(x,\omega) = F_0 \delta(x - x_0) - p(x,\omega,0) \\
- \sum_{n\in\mathbb{Z}} F(x,\omega)\,\delta(x - nd) \\
+ \sum_{n\in\mathbb{Z}} \frac{\partial}{\partial x}\left(M(x,\omega)\,\delta(x - nd)\right),
\end{aligned}
\tag{4.1}
$$

where W, D and ρ_{p} are the plate's displacement, complex flexural rigidity and mass density, respectively. $p(x,\omega,0)$ is the wall pressure due to the fluid loading. The Dirac delta function is presented by δ. $F(x,\omega)\,\delta(x - nd)$ and $M(x,\omega)\,\delta(x - nd)$ are respectively the force and moment distributions related to the interaction between the plate and the nth stiffener. Assuming displacement continuity between the plate and stiffeners, the force and moment at their interface can be expressed as,

$$
F(x,\omega) = T_{\mathrm{s}}(\omega)\, W(x,\omega), \tag{4.2}
$$

$$
M(x,\omega) = R_{\mathrm{s}}(\omega)\, \frac{\partial W}{\partial x}(x,\omega), \tag{4.3}
$$

in which, T_{s} and R_{s} are the stiffener's translational and rotational dynamic stiffnesses, respectively. The numerical process for calculating these functions are provided in Section 4.1.2.

The acoustic pressure $p(x,\omega,z)$ in the fluid domain satisfies:

- The Helmholtz equation in the half space Ω occupied by the fluid,

$$\nabla^2 p\left(x,\omega,z\right)+k_{\mathrm{f}}^2 p\left(x,\omega,z\right)=0\,,\ \forall(x,\omega,z)\in\Omega, \tag{4.4}$$

  where ∇ is the Nabla operator and k_{f} is the acoustic wavenumber.

- The Euler equation at the interface between plate and the fluid is given by,

$$\rho_{\mathrm{f}}\omega^2 W(x,\omega,0)=\frac{\partial p}{\partial z}(x,\omega,0). \tag{4.5}$$

- The Sommerfeld radiation conditions on a fictional infinite surface.

Applying space-Fourier transform to Eq. 4.1 yields [66]

$$\begin{aligned}\left[D\left(k_x^4\right)-\omega^2\rho_{\mathrm{p}}h\right]\widetilde{W}(k_x) =& F_0 e^{-\mathrm{j}k_x x_0}-\widetilde{P}(k_x,0)\\ &-\frac{1}{d}T_{\mathrm{s}}\left[\sum_{n\in\mathbb{Z}}\widetilde{W}\left(k_x+\frac{2\pi n}{d}\right)\right]\\ &-\frac{k_x}{d}R_{\mathrm{s}}\left[\left(k_x+\frac{2\pi n}{d}\right)\sum_{n\in\mathbb{Z}}\widetilde{W}\left(k_x+\frac{2\pi n}{d}\right)\right],\end{aligned} \tag{4.6}$$

whereas applying the space-Fourier transform to Eqs. 4.4 and 4.5 yields

$$\begin{cases}\widetilde{P}(k_x,z)=\frac{\rho_{\mathrm{f}}\omega^2 e^{\alpha z}}{\alpha}\widetilde{W}(k_x) & \text{if}\quad k_x\neq k_{\mathrm{f}},\\ \widetilde{P}(k_x,z)=C,\quad \widetilde{W}(k_x)=0 & \text{if}\quad k_x=k_{\mathrm{f}},\end{cases} \tag{4.7}$$

where C is a constant and $\alpha=-\sqrt{k_x^2-k_{\mathrm{f}}^2}$. Finally, the spectral displacement and pressure can be written as [66, 68],

$$\widetilde{W}\left(k_x\right)=\widetilde{W}_0\left(k_x\right)\Gamma\left(k_x\right), \tag{4.8}$$

$$\widetilde{P}\left(k_x,z\right)=\widetilde{P}_0\left(k_x,z\right)\Gamma\left(k_x\right), \tag{4.9}$$

where, $\widetilde{W}_0\left(k_x\right)$ and $\widetilde{P}_0\left(k_x,z\right)$ are respectively the spectral displacement of the plate and spectral pressure for each value of z considering the plate without the stiffeners. k_x is the wavenumber in the x direction. The contributions of the stiffeners to the plate's

vibration are given by $\Gamma(k_x)$. $\widetilde{W_0}(k_x)$ can be defined as,

$$\begin{cases} \widetilde{W_0}(k_x) = \frac{F_0 e^{-\mathrm{j}k_x x_0}}{Z(k_x)} & \text{if } k_x \neq k_\mathrm{f}, \\ \widetilde{W_0}(k_x) = 0 & \text{if } k_x = k_\mathrm{f}, \end{cases} \tag{4.10}$$

and the spectral pressure $\widetilde{P_0}(k_x, z)$ is given by,

$$\begin{cases} \widetilde{P_0}(k_x, z) = \frac{\rho_\mathrm{f}\omega^2 F_0 e^{-\mathrm{j}k_x x_0} e^{\alpha z}}{Z(k_x)\alpha} & \text{if } k_x \neq k_\mathrm{f}, \\ \widetilde{P_0}(k_x, z) = F_0 e^{-\mathrm{j}k_x x_0} & \text{if } k_x = k_\mathrm{f}, \end{cases} \tag{4.11}$$

in which $Z(k_x)$ is the fluid-loaded plate dynamic stiffness defined by

$$Z(k_x) = Dk_x^4 - \rho_\mathrm{p}\omega^2 h + \mathrm{FL}, \tag{4.12}$$

where FL is the fluid loading term,

$$\mathrm{FL} = \frac{\rho_\mathrm{f}\omega^2}{\alpha}. \tag{4.13}$$

The stiffeners contribution $\Gamma(k_x)$ is given by the following expression

$$\Gamma = \frac{\gamma_1 - \gamma_2 - \gamma_3}{\gamma_4 - \gamma_5}, \tag{4.14}$$

where,

$$\begin{cases} \gamma_1 = \frac{1}{d^2} T_\mathrm{s} R_\mathrm{s} S_1 \left(S_1 - \widehat{S}_1 \right), \\ \gamma_2 = \left(1 + \frac{1}{d} R_\mathrm{s} S_2 \right) \left[1 + \frac{1}{d} T_\mathrm{s} \left(S_0 - \widehat{S}_0 \right) \right], \\ \gamma_3 = \frac{1}{d} k_x R_\mathrm{s} \left[\frac{1}{d} T_\mathrm{s} \left(\widehat{S}_0 S_1 - S_0 \widehat{S}_1 \right) - \widehat{S}_1 \right], \\ \gamma_4 = \frac{1}{d^2} T_\mathrm{s} R_\mathrm{s} S_1^2, \\ \gamma_5 = \left(1 + \frac{1}{d} R_\mathrm{s} S_2 \right) \left(1 + \frac{1}{d} T_\mathrm{s} S_0 \right), \end{cases} \tag{4.15}$$

in which,

$$S_p = \sum_{n \in \mathbb{Z}} \frac{\left(k_x + \frac{2\pi n}{d} \right)^p}{Z\left(k_x + \frac{2\pi n}{d} \right)}, \ \widehat{S}_p = \sum_{n \in \mathbb{Z}} \frac{\left(k_x + \frac{2\pi n}{d} \right)^p e^{-\mathrm{j}\frac{2\pi n}{d} x_0}}{Z\left(k_x + \frac{2\pi n}{d} \right)}, \tag{4.16}$$

where S_p and $\widehat{S}_p$ are associated with the stiffener number n and spacing between stiffeners d, considering $p = 0, 1, 2$. Finally, the spectral displacement and pressure in the wavenumber space can be analytically calculated from Eqs. 4.8 and 4.9, respectively.

4.1.1 Estimation of the vibratory field and sound power

As an indicator of the plate vibration, we can define the mean quadratic plate velocity on the plate section $[0, L]$ as [36],

$$\langle v^2 \rangle = \frac{\omega^2}{L} \int_0^L |W(x, \omega)|^2 dx, \tag{4.17}$$

where L is a distance from the excitation point. For the numerical application, the plate length L is equivalent to the distance covering the first 15 stiffeners ($L = 15d$). The displacement $W(x, \omega)$ can be estimated from the inverse discrete Fourier transform (IDFT) of the spectral displacement $\widetilde{W}(k_x)$ given by Eq. 4.8. Also in order to investigate the vibrational response, the transmissibility can be obtained considering the surface of the plate covering n stiffeners. The transmissibility is given by

$$\mathrm{T}_n = \frac{w_n^2}{w_0^2}, \tag{4.18}$$

in which, w_n and w_0 are the displacement at the n^{th} stiffener and at the stiffener at source, respectively. The transmissibility results presented in this paper consider $n = 15$.

The total acoustic power can be deduced using formulations exclusively dependent on the spectral wall pressure or displacement as Eq. 4.7 holds [108]. The radiated sound power exclusively dependent on the pressure can be written as follows,

$$\Pi = \frac{\rho_{\mathrm{f}} \omega}{4\pi} \int_{k \in \Omega_a} \frac{1}{\sqrt{k_x^2 - k_{\mathrm{f}}^2}} |\widetilde{V}(k_x)|^2 dk, \tag{4.19}$$

where, $\Omega_a = \{k_x \in \mathbb{R}, |k_x| \leq k_{\mathrm{f}}\}$ does not consider subsonic waves that do not propagate to the far-field and $\widetilde{V}(k_x)$ is the spectral velocity derived from Eq. 4.8. It should be noted that structural damping is introduced in the stiffened plate by considering complex Young's modulus. In Section 4.2.1, the present numerical results will be verified against those obtained from an FE model. Since in the FE model, only the sound power from a finite length of the stiffened plate can be obtained, to be able to conduct the verification

study, the radiated sound power from a finite length of the plate should be defined. Similar to the mean quadratic velocity, the sound power (Π_L) can be calculated in the spatial domain considering a finite length of the plate as follows

$$\Pi_L = 1/2 \int_0^L \Re[p(x,\omega,0)v^*(x,\omega)]dx, \tag{4.20}$$

in which, v^* is the complex conjugate of the plate's velocity $v(x,\omega)$, and $\Re$ is the real part of the complex number. IDFTs are applied on the spectral responses of the semi-analytical model to obtain the velocity $v(x,\omega)$ and wall pressure $p(x,\omega,0)$ in the spatial domain.

4.1.2 Numerical calculation of the dynamic stiffness of the stiffeners

To account for the stiffeners contribution to the plate's dynamic behavior, we must determine their translational and rotational dynamic stiffnesses as delineated in Eqs. 4.2 and 4.3. Herein, an FE model of the stiffeners as illustrated in Fig. 4.2(a) is used to evaluate their dynamic stiffnesses. The FE model follows the mesh and element sizes described in Section 4.2.1, and is modeled using Solid Mechanics module in COMSOL Multiphysics™. Based on the initial assumption that the stiffeners have rigid connections with the plate, herein, the stiffeners are considered to have a Rigid Connector at the top edge where the force $F_s(\omega)$ and moment $M_s(\omega)$ are applied at the point B.

The schematic to obtain the translational and rotational dynamic stiffenesses is presented in Fig. 4.2(b). More precisely, the translational dynamic stiffeness $T_s(\omega)$ is obtained by the ratio between the force $F_s(\omega)$ applied at the point B and the resulting displacement $W_s(\omega)$. Similarly, the rotational dynamic stiffeness $R_s(\omega)$ can be obtained by the ratio between the moment $M_s(\omega)$ applied at point B and the rotational response θ.

As shown in Fig. 4.2, the ABH stiffener considered in the following sections utilizes damping layers to mitigate the reflected waves at the tip which mimics the ideal ABH as outlined in Ref. [43]. The correlation between the length of the ABH (L_{ABH}) and the local thickness (h_{ABH}) follows the power law curve expressed as $h_{\text{ABH}}(z_s) = \alpha z_s^2 + h_{\text{tip}}$, where α represents the power-law constant, h_{tip} is the tip thickness of the ABH, and z_s is the distance along L_{ABH} considering the local coordinate system (x_s, z_s).

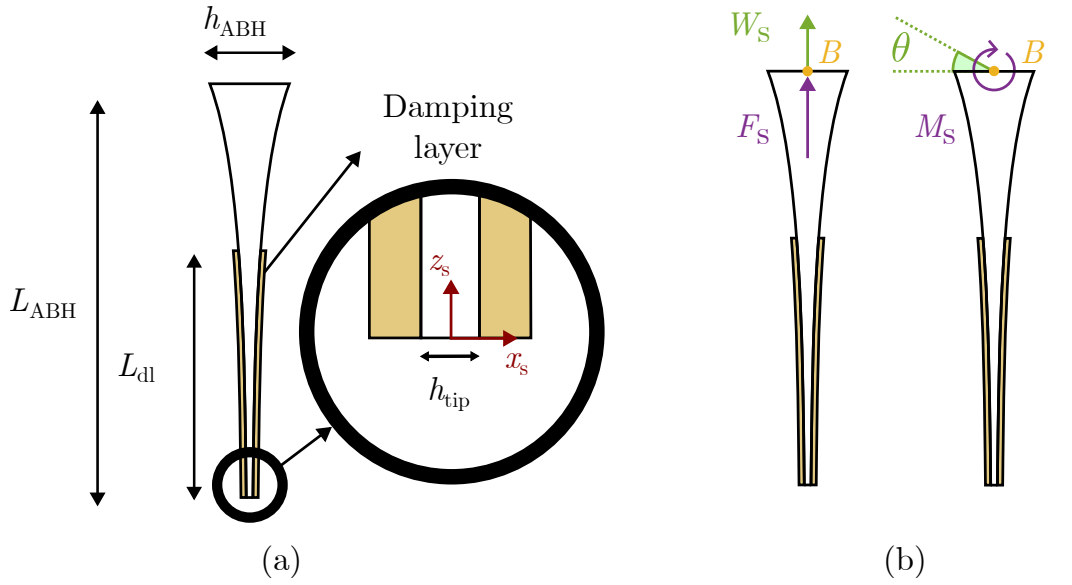

FIGURE 4.2: Schematics of (a) the ABH modeled by the FE and (b) the applied force and the moment to obtain the dynamic stiffness.

4.1.3 Bloch-Floquet propagating waves

In the introduction, it was established that the passbands of the BF waves are associated with high levels of vibroacoustic responses. Therefore it is relevant to determine the BF passbands of the analysed system, in order to study how different stiffeners can modify the wave propagation characteristics within these frequency ranges and influence the radiated noise. The BF propagating waves can be identified by finding the real roots k^{BF} of the dispersion equation, corresponding to the denominator of Γ when the system is supposed conservative (i.e. without dissipation). If the k^{BF} are real, it implies that the BF waves are able to travel across the plate without attenuation. The dispersion equation, is given by

$$\Delta\left(k^{\mathrm{BF}}\right) = \gamma_4\left(k^{\mathrm{BF}}\right) - \gamma_5\left(k^{\mathrm{BF}}\right) = 0. \tag{4.21}$$

Previous research [77] has shown that when accounting for fluid loading in the formulation, it is not possible to derive explicit expressions for k^{BF}. As accounted by other studies [65, 68], an algorithm can be used to compute the real values for k^{BF}, and hereby the procedure is presented by the flowchart in Fig. 4.3. The objective is to identify the roots of Δ within the first Brillouin zone (i.e. $[0, \pi/d]$). The Brillouin zone is the fundamental region in reciprocal space that contains all unique wavenumbers which describe

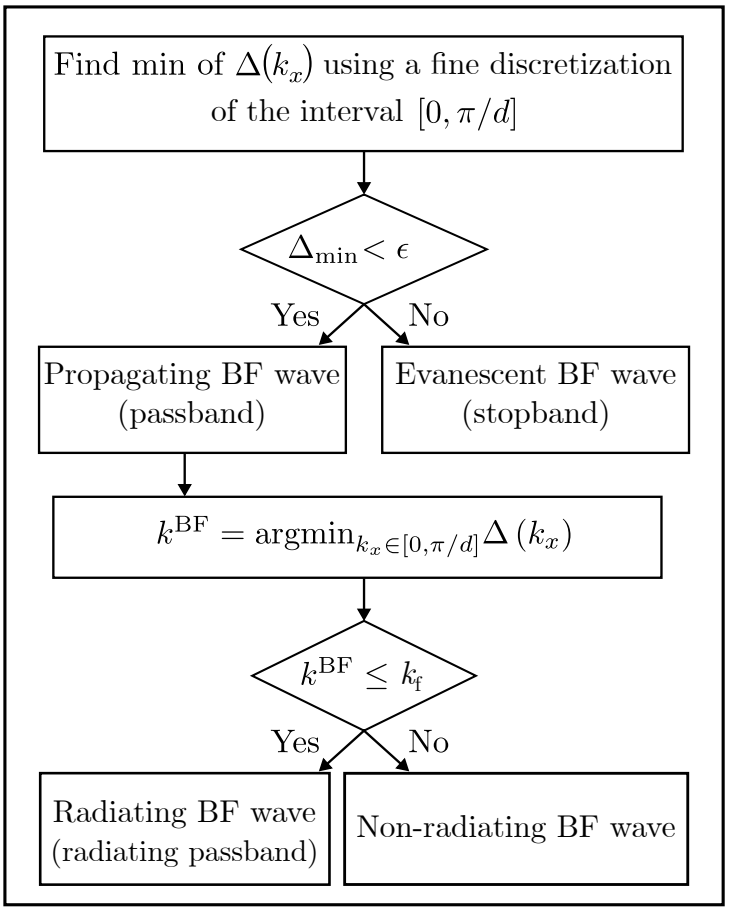

FIGURE 4.3: Algorithm to obtain the BF propagating waves considering a two-dimensional model.

the wave behavior in a periodic medium, hence in this case only the first Brillouin zone needs to be examined [10, 40]. The algorithm described in Fig. 4.3 is implemented as follows:

1. Find the real roots of the dispersion equation (Eq. 4.21) by discretising the wavenumber space $[0, \pi/d]$ with a fine resolution, and identifying where Δ falls below a given threshold, ϵ, for the considered wavenumbers.

2. If there is a real root k^{BF} for the given excitation frequency, the BF wave will propagate; otherwise, it will be an evanescent BF wave.

3. Compare the real root k^{BF} to the acoustic wavenumber to determine whether the BF wave is radiating ($k^{\mathrm{BF}} \leq k_{\mathrm{f}}$) or non-radiating ($k^{\mathrm{BF}} > k_{\mathrm{f}}$).

The process is applied using a threshold of $\epsilon = 0.05$ and a resolution of 0.0001 to discretise the wavenumber space $[0, \pi/d]$. After computing the passbands with the criterion $\Delta_{\min} <$

ϵ, the BF passbands are compared against the acoustic wavenumber k_f to determine if they are radiating ($k^\mathrm{BF} \leq k_\mathrm{f}$) or non-radiating ($k^\mathrm{BF} > k_\mathrm{f}$). It should be emphasized that Δ should be calculated for the conservative system. This means that the damping should be excluded from the system. Therefore, only the real parts of the Young's modulus and fluid loading term should be considered for computing passbands and stopbands. An example of the obtained k^BF is presented in Fig. B.1.

4.2 Results and discussion

In this section, we explore how the ABH stiffeners could be a substitute for the rectangular stiffeners to mitigate the vibroacoustic response. Let us assume that we have a fluid-loaded stiffened plate with periodic rectangular stiffeners each with an area of A and moment of inertia of I_0 at point of contact with the plate. We would like to replace the conventional rectangular stiffeners with equivalent ABH stiffeners that are designed to match the rectangular stiffener's area A and moment of inertia I_0 ensuring that both stiffeners have similar weight and static stiffness. Both rectangular and ABH stiffeners have identical material properties as the plate, as detailed in Table 4.1, their geometrical properties are also given in Table 4.2. Before we proceed with the investigation using the semi-analytical model, we will first verify its accuracy in predicting the vibroacoustic response of the infinite heavy fluid-loaded plate with ABH stiffeners.

TABLE 4.1: Material properties of the structure and damping layer.

Parameters	Plate and stiffeners	Damping Layer
Young's modulus ($E_\mathrm{p,dl}$)	$210 \times 10^9\,(1 + \mathrm{j}\eta_\mathrm{p})$ Pa	$0.25 \times 10^9\,(1 + \mathrm{j}\eta_\mathrm{dl})$ Pa
Mass density ($\rho_\mathrm{p,dl}$)	7800 kg/m^3	950 kg/m^3
Poisson's ratio (ν)	0.3	0.3
Loss factor ($\eta_\mathrm{p,dl}$)	0.005	0.5

TABLE 4.2: Geometrical properties of the stiffeners.

Parameters	Rectangular stiffener	ABH stiffener
Thickness ($h_\mathrm{r,ABH}$)	0.010 m	0.016 m
Length ($L_\mathrm{r,ABH}$)	0.100 m	0.164 m
Tip thickness (h_tip)	-	0.0005 m
Damping layer length (L_dl)	$0.7L_\mathrm{r}$	$0.7L_\mathrm{ABH}$
Damping layer thickness (h_dl)	0.003 m	0.003 m

4.2.1 Semi-analytical model verification

A MATLAB code was developed based on the formulation described in the previous section, and a corresponding 2D FE model was created, as depicted in the schematic shown in Fig. 4.4 using the commercial software COMSOL Multiphysics™. In the FE model, we utilised a perfectly matched layer (PML) to simulate the infinite plate. The PML serves as a synthetic absorbing layer, effectively dampening the waves as they propagate and minimising any reflections at the boundary. Both models were used to generate vibroacoustic results to verify the semi-analytical model, considering the geometrical and material properties in Tables 4.1 and 4.2. Due to the limitation of the FE model to account for the infinite domain, the plate length L is considered to be the distance covering the first 15 stiffeners ($L = 15d$). The system is considered to be excited by a point force $F_0 = 1$ N at $x = 0$ m, and has ABH-shaped stiffeners.

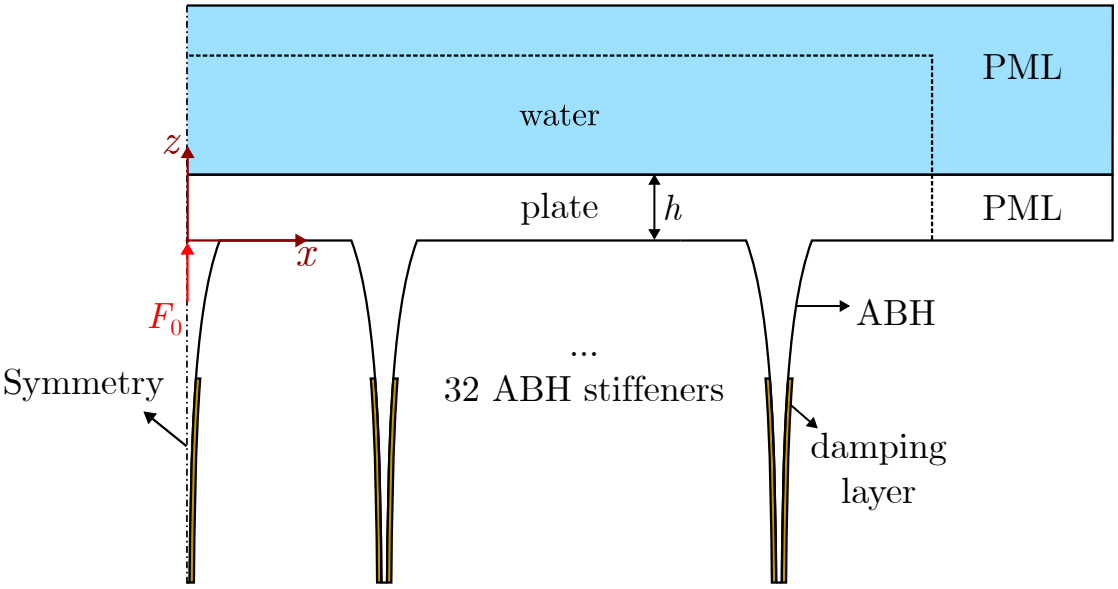

FIGURE 4.4: Schematic of the FE model of the infinite heavy fluid-loaded plate utilized in COMSOL Multiphysics™.

The mean quadratic velocity (Eq. 4.17) and sound power (Eq. 4.20) response obtained using the semi-analytical model are compared against the response computed for the full FE model of the stiffened-plate-fluid system in COMSOL Multiphysics™ as shown in Fig. 4.5. In the FE model, we utilised a mapped mesh with element size determined by considering the criterion of 12 elements per wavelength. In this context, the model with fluid loading has 272280 elements. This specification was based on the wavelength at the tip of the ABH stiffener, corresponding to the highest frequency of interest, 5000 Hz.

Based on a convergence study (results are not shown here), the PML size was set to 6 m, while the fluid layer above the structure was set to a height of 0.75 m. The vibration and acoustic responses are shown in Figs. 4.5(a) and (b), respectively. In both sets of results, multiple peaks are evident. These peaks originate from the BF waves and are associated with the passbands identified by the algorithm presented in Section 4.1.3. These results will be further discussed in the subsequent sections. As shown in Fig. 4.5, the results obtained by the semi-analytical model are in a good agreement with the response of the FE model, with a difference lower than 2 dB. Notably, the computational time required for the semi-analytical modelling to obtain the vibroacoustic response across the entire analysed frequency range was approximately three minutes (two minutes for running the MATLAB script and one minute to calculate the translational and rotational dynamic stiffnesses using COMSOL Multiphysics™). In contrast, the FE model required ten hours. This indicates that the computational time of the present approach was less than 1% of that required for the FE model. These are the computing times considering the a computer with 2x AMD EPYC 7532 2.40GHz 32 cores and 1 TB RAM. It is noteworthy that the mesh of the FE model was optimised based on the excitation frequency, ensuring a minimum of 12 elements per the smallest wavelength in the model.

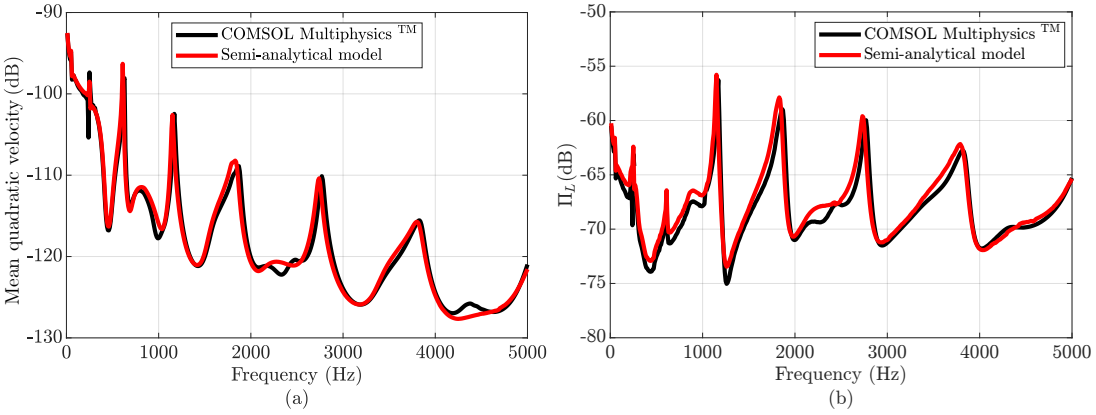

FIGURE 4.5: Comparison of the FE model using COMSOL Multiphysics™ (black line) and the semi-analytical formulation (red line) in terms of (a) mean quadratic velocity defined by Eq. 4.17 (dB, ref. 1 m^2 s^{-2}), and (b) radiated sound power defined by Eq. 4.19 (dB, ref. 1 W).

4.2.2 Vibration response

In order to verify if the ABH stiffeners could substitute the rectangular stiffeners to control the vibroacoustic response, let us investigate how the damping layers and the

ABH-shaped stiffener affect the vibratory response. It is well known that when designing an ABH, it is necessary to account for the ABH's cut-on frequency ($f_{\text{cut-on}}$). By definition, the cut-on frequency of ABH is a critical parameter that delineates the threshold at which the ABH begins to effectively propagate and absorb flexural waves, marking the commencement of its damping capabilities [87]. The cut-on frequency is dependent on the geometry and material properties, and for the ABH stiffener considered in this work is defined as follows [11],

$$f_{\text{cut-on}} = \frac{\pi h_{\text{ABH}}}{4L_{\text{ABH}}^2}\sqrt{\frac{E_{\text{s}}}{3\rho_{\text{s}}}}, \tag{4.22}$$

in which E_{s} is the Young's modulus of the stiffeners. Based on Eq. 4.22 and the ABH parameters outlined in Table 4.2, the cut-on frequency for this shape is identified at 1392 Hz.

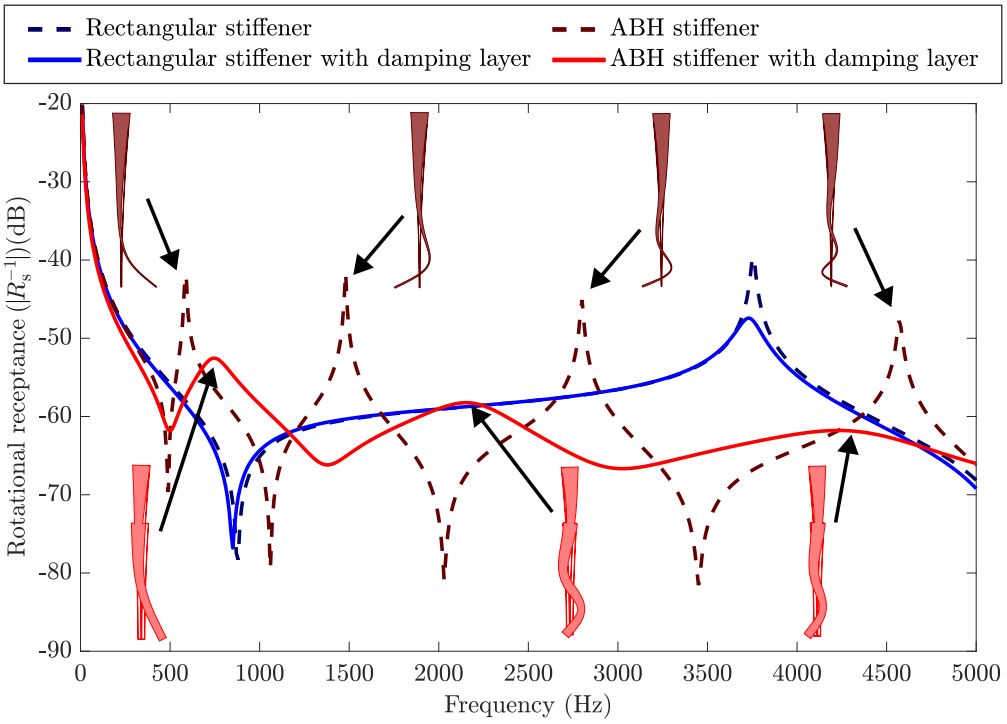

FIGURE 4.6: Comparison of the rotational receptance ($|R_s^{-1}|$) between rectangular and ABH stiffeners. Mode shapes of the ABH stiffener with damping layers are highlighted in red at their respective resonance frequencies. (dB, ref. 1 rad.N^{-1}.m^{-1}).

An initial analysis is made in relation to the addition of the damping layers to the two stiffener shapes. The stiffeners are modelled in COMSOL as described in Section 4.1.2. Fig. 4.6 shows the rotational receptance ($|R_s^{-1}|$) of the rectangular and ABH stiffeners

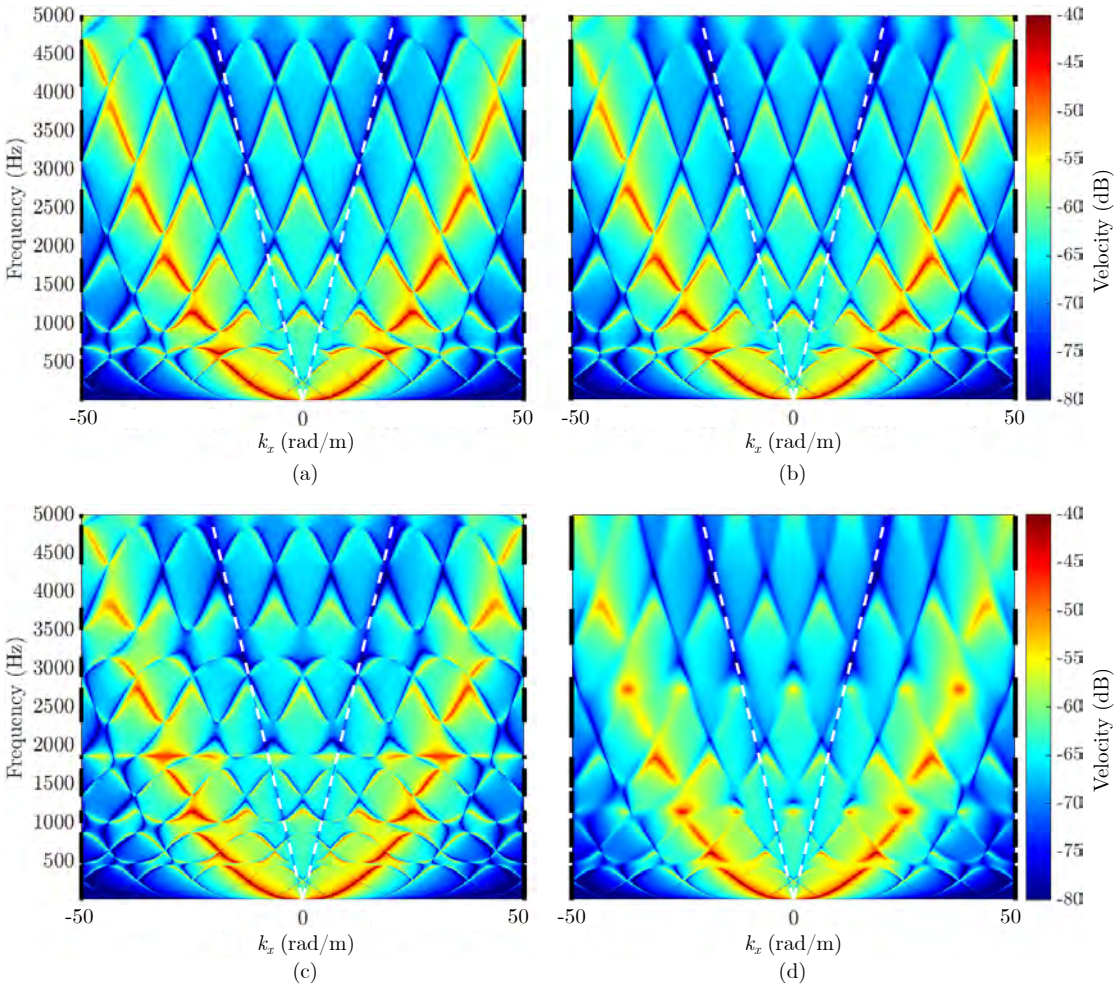

FIGURE 4.7: Wavenumber spectrum of the heavy fluid-loaded (water) plate's velocity (a) with rectangular stiffeners, (b) with rectangular stiffeners and damping layers, (c) with ABH stiffeners without damping layers and (d) with ABH stiffeners and damping layers. The acoustic wavenumber k_f is presented by the white dashed line. (dB, ref. 1 m.s^{-2}.N^{-1}).

with and without damping layers. Due to the identical static stiffness of both stiffeners, at low frequencies the rotational receptance is similar across all cases. For the rectangular stiffener, the addition of the damping layers causes a slight frequency shift around 790 Hz and a slight attenuation of the peak around 3700 Hz. In contrast, the ABH stiffener is greatly influenced by the damping layers addition. Specifically, the rotational receptance of the ABH stiffener with damping layers shows less pronounced resonance peaks and a shift to higher frequencies, despite the added mass from the damping layers. The damping layer not only adds inertia but also contributes to the stiffness of the ABH, especially when its thickness is significant compared to the ABH thickness at the tip. The ABH stiffener with damping layers has 3 resonance frequencies in the analysed spectrum

range, whilst the ABH stiffener without damping layers has 4 resonance frequencies in the same spectrum. The resonance frequencies and respective mode shapes are also shown in Fig. 4.6. The flexural natural frequency and mode shapes were obtained using COMSOL Multiphysics™ eigenfrequency analysis. The natural frequencies of the ABH stiffener with damping layers are 742 Hz, 2177 Hz, and 4310 Hz and they correspond to the resonance peaks in Fig. 4.6. Similarly, the natural frequencies of the ABH stiffener without damping layers are 585 Hz, 1479 Hz, 2798 Hz and 4572 Hz and they correspond to the resonance peaks in Fig. 4.6. One can note that, higher modes can be associated with a greater damping effect, leading to a dampened rotational receptance spectrum without prominent resonance peaks and shifted to higher frequencies. This effect is evident from the distinct attenuation pattern of the ABH stiffeners with damping layers, compared to the ABH stiffeners without damping layers.

The wavenumber spectrum of the heavy fluid-loaded (water) plate's velocity of four different cases are presented in Fig. 4.7. The four cases are the fluid-loaded plate with (a) rectangular stiffeners, (b) rectangular stiffeners and damping layers, (c) ABH stiffeners without damping layers and (d) ABH stiffeners and damping layers. The acoustic wavenumber is presented by the white dashed line, and the respective passbands are given by the black bars in the y-axis at both edges of the spectrum. It can be observed from Fig. 4.7(a) and (b) that adding damping layers into the rectangular stiffeners does not significantly alter the system's vibrational response up to 4000 Hz. Above 4000 Hz, a slight mitigation is noticeable in the wavenumber spectrum causing a "blurry" effect in the color gradient of the amplitude. When comparing Figs. 4.7(c) and (d), it is noticeable that the addition of damping layers led to a greater mitigation effect in the system's response. The same blurry effect in the color gradient that once occurred smoothly for the rectangular-stiffened plate, here for the ABH-stiffened plate has a greater effect. The velocity response inside the acoustic triangle (i.e., $|k_x| \leq k_\mathrm{f}$) has slightly lower amplitudes when the damping layers are added, this is visible by the change from yellow to green in the color gradient. Now considering the two cases with damping layers, Fig. 4.7(b) and (d), it is clear that the ABH stiffeners present a lower amplitude response within the acoustic triangle and a blurry effect for the response above 450 Hz. For all the subsequent calculations, we will only consider stiffeners with the damping layers.

Fig. 4.8 shows the vibration behaviour of the plate with rectangular stiffeners and ABH stiffeners in terms of mean quadratic velocity and transmissibility. The passbands of the

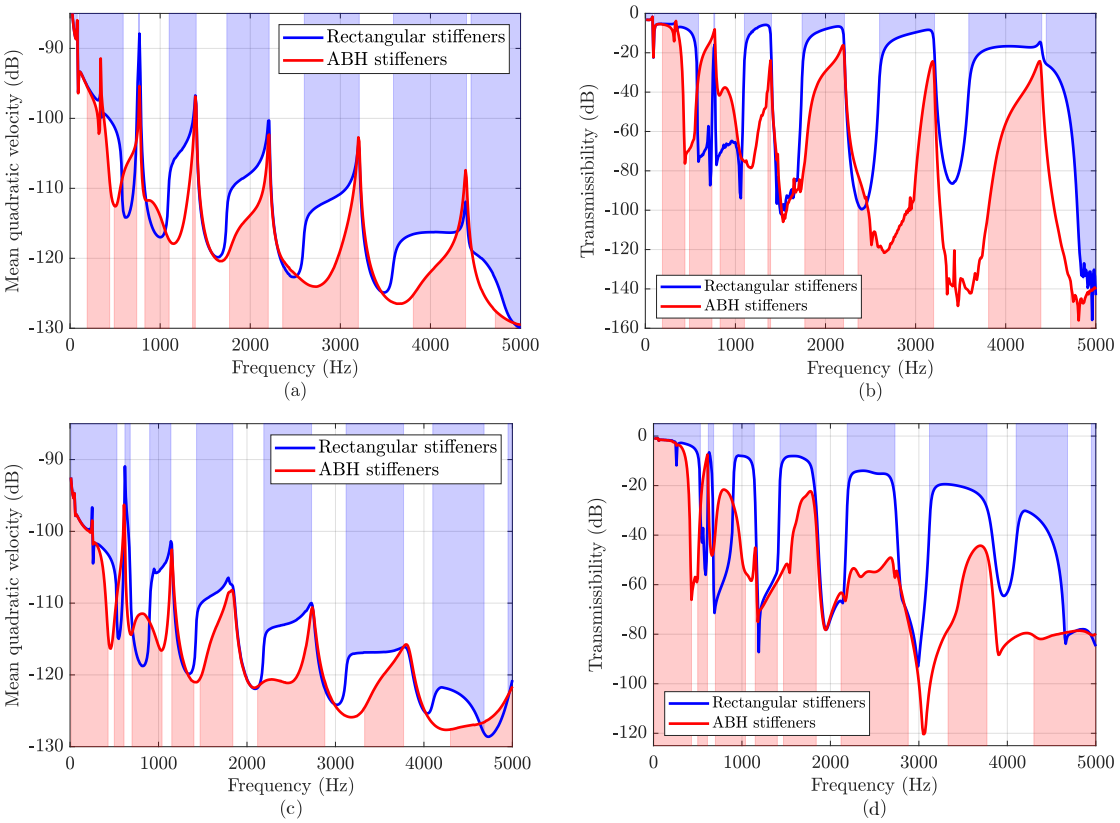

FIGURE 4.8: Comparison between the plate with rectangular stiffeners and ABH stiffeners in terms of (a) the mean quadratic velocity (dB, ref. 1 $m^2\ s^{-2}$) and (b) transmissibility between the first 15 stiffeners for the case in air. Comparison of the response considering the fluid to be water in terms of (c) the mean quadratic velocity (dB, ref. 1 $m^2\ s^{-2}$) and (d) transmissibility between the first 15 stiffeners.

BF propagating waves are highlighted by the blue-shaded and red-shaded areas for the system with rectangular stiffeners and ABH stiffeners, respectively. The passbands were obtained using the algorithm presented in Section 4.1.3 considering the respective system with rectangular or ABH stiffeners. It is visible that the high amplitude response peaks are associated with the BF passbands as already established in the literature [65, 68]. To analyze the influence of fluid loading on the response, two cases are considered: in air Figs. 4.8(a),(b) and in water Figs. 4.8(c),(d).

Figs. 4.8(a) and (c) show the mean quadratic velocity of the two analysed systems considering the case in air and in water, respectively. It can be seen that the system with ABH stiffeners presents a lower response amplitude in almost the entire analysed frequency range reaching up to 10 dB difference at 2720 Hz for the case in air Fig. 4.8(a) and 1500 Hz for the case in water Fig. 4.8(c). The ABH-stiffened plate was able to mitigate the plate's velocity at a wide frequency range within the passbands as observed

in four out of five passbands from 742 Hz to 4500 Hz. As frequencies approach the transition into stopbands, the velocity amplitude increases which indicates that the ABH is able to mitigate the propagation of the BF waves in the start of the passbands. However, its effectiveness diminishes at frequencies towards the end of the passbands. Interestingly, for the case in water as shown in Fig. 4.8(c), the mitigation in the response occurs systematically above 742 Hz which is the first flexural natural frequency of the ABH stiffener with damping layers and it is below the cut-on frequency. Considering the rectangular-stiffened plate, the noticeable vibration reduction begins above 4500 Hz caused by the damping layers as already shown in the wavenumber spectrum response (Fig. 4.7(d)). When both stiffened plates are inside a stopband the type of stiffeners has few influence in the mean quadratic velocity as observed in the stopbands around 1500 Hz and 1750 Hz for the case in air Fig. 4.8(a), and 2000 Hz and 3000 Hz for the case in water Fig. 4.8(c).

Similarly, Figs. 4.8(b) and (d) present the transmissibility of the two stiffened plates considering the cases in air and water, respectively. When observing the transmissibility comparison for both fluid-loading cases in Figs. 4.8(b) and (d), it is evident that the differences between the ABH-stiffened response and the rectangular-stiffened response are generally greater than those observed for the same cases in the mean quadratic velocity. This can be explained by the fact that the ABH stiffeners have minimal effect on the vibrations near the excitation point, where these vibrations are most significant, thereby having a stronger influence on the mean quadratic velocity. However, the effect of the ABH stiffeners is more pronounced on the transmissibility, as the propagating flexural waves are attenuated at each ABH stiffener between the excitation point and the receiving point. Both fluid-loading cases exhibit similar trends, showing a systematic reduction at the beginning of the third passband for the rectangular stiffener, which is consistent with the results of the mean quadratic velocity. In contrast to the latter, the passbands in the transmissibility response for the case in water do not display the same pattern of high response amplitude at each transition into stopbands. It is evident that the overall vibrational response levels in air are higher than those in water. This is observed by comparing the mean quadratic velocity and transmissibility for both cases, as shown in Figs. 4.8(a) and (c) and Figs. 4.8(b) and (d), respectively. Unlike the ABH-stiffened plate, the transmissibility from the rectangular-stiffened plate maintain the high amplitudes for all passbands, with a partial attenuation in its last passband which

is consistent with the results in the wavenumber domain (Fig. 4.7). The change in the fluid-loading from air to water for the rectangular-stiffened structure led to a shift of the passbands to lower frequencies, this is noticeable observing the third to the sixth passbands.

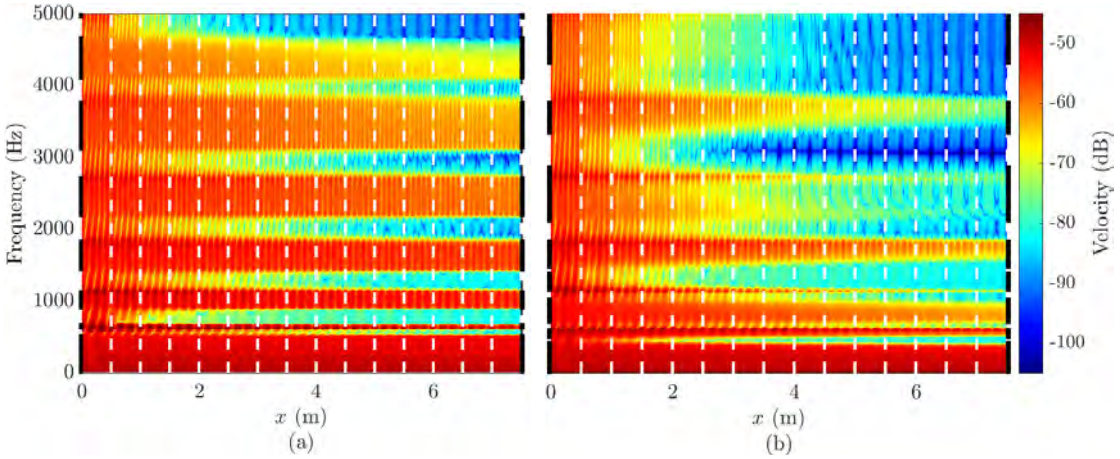

FIGURE 4.9: Spatio-spectra map of the plate's surface velocity (x, ω) considering the plate with (a) rectangular stiffeners and (b) ABH stiffeners. The stiffener's positions are presented by the white dashed lines and the passbands are presented by the black bars at the edge of each map. (dB, ref. 1 m.s^{-1}).

Fig. 4.9 shows the spatio-spectra map of the plate's surface velocity for the two stiffened plates considering a heavy-fluid loading. The stiffener's positions are presented by the vertical white dashed lines, and the respective passbands are presented by the black bars in the y-axis at each map's edge. Considering the spatio-spectra map of the surface velocity of the plate with rectangular stiffeners (Fig. 4.9(a)), the high amplitude within the passbands remains from the source at $x = 0$ m to the 15$^{\text{th}}$ stiffener at $x = 7.5$ m. In conformity with the previous results (Figs. 4.7 and 4.8) for the plate with rectangular stiffeners, the only passband that presents a high mitigation is the one above 4000 Hz, changing from orange to yellow-green, representing around 15 dB in difference. When observing Fig. 4.9(b) which presents the response of the plate with ABH stiffeners, the mitigation is greater in almost all the passbands. Considering the passbands from 2000 Hz to 5000 Hz, all three were lowered more than 20 dB after the 10^{th} stiffener, showing the strong mitigation capability of the ABH stiffener. This is observed by the high vibration decaying rate changing the color gradient from red to green/blue within the 2000 Hz - 5000 Hz frequency range. The passbands bellow 2000 Hz, were partially mitigated but a peak still remains after the 15 stiffeners, showing again that the effectiveness of the ABH stiffener diminishes at frequencies towards the end of the

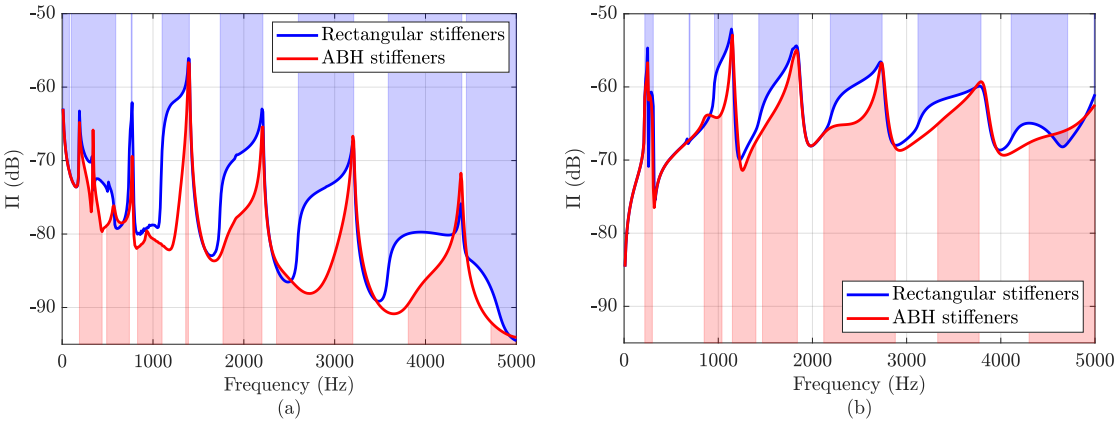

FIGURE 4.10: Radiated sound power of the rectangular-stiffened plate and the ABH-stiffened plate considering the case in (a) air and (b) water. The blue-shadded and red-shadded areas represent the radiating passbands of the propagating BF waves for the system with rectangular stiffeners and ABH-stiffeners, respectively. (dB, ref. 1 W).

passbands. The findings in this section confirm that the vibration response can be effectively mitigated by replacing common rectangular stiffeners with ABH stiffeners, leading us to investigate how the acoustic response is affected.

4.2.3 Radiated sound power

The radiated sound power of the infinite fluid-loaded plate with rectangular and ABH stiffeners are presented in Fig. 4.10, using Eq. 4.19 considering the cases in air Fig. 4.10(a) and water Fig. 4.10(b). The radiating passbands of the BF propagating waves are highlighted by the blue-shaded and red-shaded areas for the system with rectangular stiffeners and ABH stiffeners, respectively. Figs. 4.10(a) and (b) show that the highest amplitudes are within the BF passbands. Similarly to the vibration response, the sound power of the system with ABH stiffeners exhibits lower amplitude across nearly the entire frequency range compared to the system with rectangular stiffeners, in both cases (i.e., air or water). This similarity arises because the sound power equation is dependent from the spectral velocity and in the acoustic domain, Ω_a, as shown in Eq. 4.19. The ABH-stiffened plate presents reduced sound power amplitude for frequencies at the beginning of the third passband, which is consistent with the vibration results. This is observed when comparing the difference in amplitudes between the two response curves within the passbands for the results above 1050 Hz in air Fig. 4.10(a) and 742 Hz in water Fig. 4.10(b). The response from the ABH-stiffened plate presents a lower amplitude

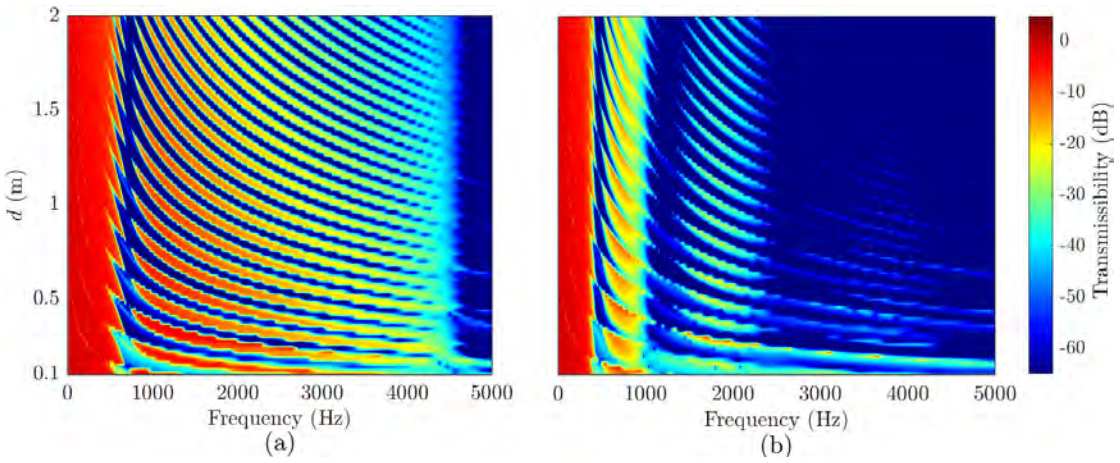

FIGURE 4.11: Transmissibility with respect to the stiffener spacing, considering a plate with (a) rectangular stiffeners and (b) ABH stiffeners.

up to 20 dB at 1200 Hz in air Fig. 4.10(a) and 7 dB at 2400 Hz in water Fig. 4.10(b). It is evident that the response amplitudes are higher at the end of almost all passbands, indicating partial mitigation of the radiated sound power, similar to the mean quadratic velocity results. It can be highlighted that the attenuation induced by the use of ABH stiffener instead of rectangular stiffener is less pronounced for the radiated sound power than that of the mean quadratic velocity for the case in water. However, this partial mitigation of the radiated sound power remain of interest for the practical applications. When comparing different fluid loadings, it is evident that the heavy fluid loading results in higher levels of radiated sound power due to its greater density this is consistent with Eq. 4.19.

4.2.4 Vibroacoustic response with respect to the stiffener spacing

To investigate the effect of the distance between stiffeners on the vibroacoustic response of the ABH stiffened plate in comparison to the rectangular stiffened one, this section considers the results for transmissibility and radiated sound power for various values of d considering heavy fluid loading. With a larger distance between stiffeners, additional passbands and consequently peaks are introduced to the vibration response. This can be visualised in Fig. 4.11, which presents transmissibility maps for (a) rectangular stiffeners and (b) ABH stiffeners with respect to the distance between stiffeners. The horizontal axis denotes the frequency range from 0 Hz to 5000 Hz, while the vertical axis represents

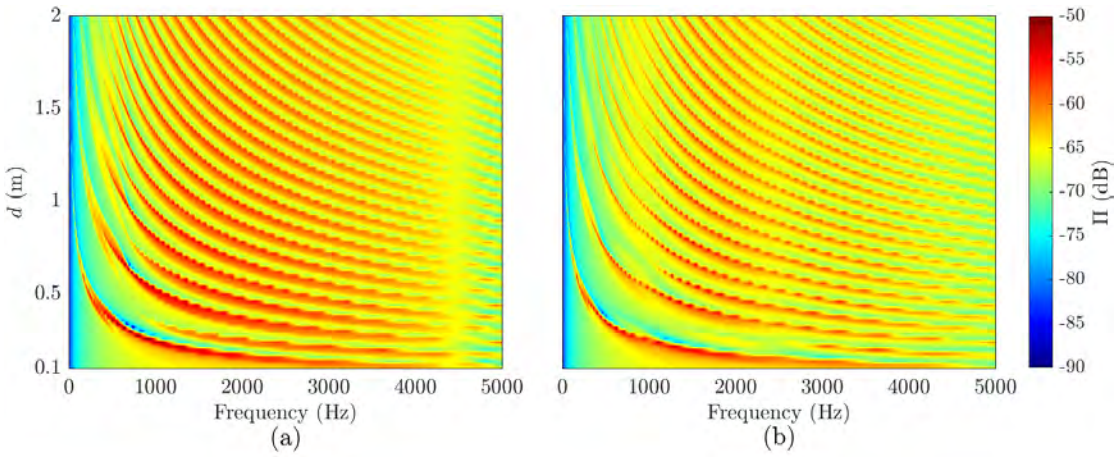

FIGURE 4.12: Radiated sound power with respect to the distance between stiffeners, considering a plate with (a) rectangular stiffeners and (b) ABH stiffeners. (dB, ref. 1 W).

the stiffener spacing denoted by d in meters. The colour gradient, quantifying transmissibility in decibels (dB), transitions from high (red) to low (blue) amplitude values. The transmissbility response from the system with rectangular stiffener shows that there is a wide frequency band (1000-4000) with a small mitigation of the vibration energy from the source to the 15^{th} stiffener. The results are consistent to the ones presented in the previous section, that shows the effect of damping layers for results above 4000 Hz. The transmissibility response for this system, is characterised by distinct, periodic bands of high transmissibility indicated by pronounced amplitude peaks. Conversely, the map presented in Fig. 4.11(b) depicts the system utilising ABH stiffeners, demonstrating a significant attenuation of transmissibility across the frequency spectrum. The ABH stiffeners exhibit an irregular pattern of reduced transmissibility, especially evident in the extended regions of low transmissibility (above 2000 Hz considering the distance d from 0.1 m to 1.5 m). The patterns are not regular as that in the rectangular-stiffened plate where we observe a clear pattern up to 4500 Hz. This behaviour could be due to the enhanced vibration damping capabilities of the ABH, acting as an intensifier of the damping layers effect since the rectangular-stiffened plate exhibits the same irregular pattern at the frequency bands where we observe the damping layers effect (above 4500 Hz). When comparing Fig. 4.11(a) and (b), the disparity between the two maps underscores the efficacy of ABH stiffeners in mitigating vibration transmission and highlights their potential vibration mitigation in stiffened structures.

Similarly to the transmissibility response, Fig. 4.12(a) presents the radiated sound power

response from a structure with rectangular stiffeners, where we observe pronounced periodic bands of high sound power, which become denser as the spacing between stiffeners increases denoting the same direct correlation between, stiffener spacing and the greater number of peaks. This configuration shows a similar pattern of high amplitudes as the transmissibility response (Fig. 4.11) and a distinct dampening effect around 4500 Hz for all the considered distances d. In contrast, Fig. 4.12(b) depicts the system with ABH stiffeners. Notably, the ABH stiffeners show a marked reduction in sound power levels across the examined frequency spectrum, demonstrated by fewer and less intense bands of high radiated sound power. This reduction in the response amplitude is visible across all considered d, thereby showcasing the ABH stiffeners' superior damping properties. The visual comparison between the two maps suggests the same partial reduction of the BF waves contribution (since it is directly associated with the high levels of vibroacoustic response). This is noted by the width of each peak (red curved area) that are less prominent in the response of the ABH-stiffened plate. These findings shows that even with a larger number of peaks (and larger distance between stiffeners) the ABH stiffeners are able to mitigate the vibroacoustic response.

4.3 Summary

In this chapter, a semi-analytical formulation for the vibroacoustic response of a 2D infinite fluid-loaded plate with ABH stiffeners was developed. The stiffeners' characteristics were defined by their translational and rotational dynamic stiffnesses obtained through an FE model. These dynamic stiffnesses were then coupled with an analytical model of the infinite fluid-loaded plate in the wavenumber domain, allowing a detailed examination of vibroacoustic response and identification of the associated passbands and radiating passbands of the propagating BF waves for given stiffened plates. The proposed method is an efficient computational tool for examining the vibroacoustic behaviour of different designs of fluid-loaded plates with complex stiffeners.

Using the developed formulation, the effectiveness of implementing ABH stiffeners as a passive approach for attenuating the vibroacoustic response of an infinite light/heavy fluid loaded plate subjected to a point force excitation was demonstrated. It was also shown that for a given rectangular stiffened plate under light/heavy fluid loading, an

equivalent ABH stiffened plate can be designed, which significantly mitigates the vibroacoustic response of the system. The equivalent ABH stiffeners were designed to have the same surface area and moment of inertia (at the contact point) as those of conventional rectangular stiffeners to maintain the same static stiffness. The ABH damping effect was observed below the so-called cut-on frequency given in the literature. Notably, the systematic mitigation effect in the passbands and radiating passbands occurred consistently above the first flexural natural frequency of the ABH stiffener. It was also shown that the vibroacoustic responses of the plate with ABH stiffeners were significantly lower than those of the plate with rectangular stiffeners at the beginning of each passband. However, the predicted responses become almost the same at the end of each passband (beginning of the next stopband) when focusing on the mean quadratic velocity results. This effect was also visualised by the spatial-spectra maps, where the vibration response was plotted along the plate for different frequencies.

The analysis also showed that ABH stiffeners significantly reduce the radiated sound power over a broad frequency spectrum inside the radiating passbands, particularly above the first flexural natural frequency of the ABH stiffeners. While the attenuation effect on the radiating sound power is less pronounced than on mean quadratic velocity, the mitigation remains valuable for practical applications. These findings underscore the advantages of using ABH stiffeners over rectangular stiffeners for noise reduction in fluid-loaded plates.

Chapter 5

Experimental and numerical vibration analysis of an ABH-stiffened beam

This chapter initially presents the experimental analysis of two finite stiffened beams, one with rectangular stiffeners and the other with equivalent ABH stiffeners. The experiment was conducted in air due to the difficulty of performing it in water. The equivalent ABH stiffeners are designed to match the rectangular stiffener's area A and moment of inertia I_0 ensuring that both stiffeners have similar mass and static stiffness. The study concentrates solely on the transmission of vibrational energy along the beams, without considering any radiation effects. Three different cases are considered. The stiffeners without damping layers, with viscoelastic layers (VLs) and with constrained viscoelastic layers (CVLs).

The experimental results are presented and discussed in Section 5.2. The effect of the damping layer addition to both type of stiffeners on the vibrational response is analysed. A comparative study between beams with ABH stiffeners and traditional rectangular stiffeners, in terms of accelerance frequency response function (FRF) and transmissibility is made. The results shows the effectiveness of replacing traditional rectangular stiffeners with ABH stiffeners to mitigate the vibrational response.

To further support these findings, numerical simulations are performed, offering deeper insights into the vibration attenuation mechanisms. The simulations are compared with

the experimental data and help identify potential discrepancies. In cases where differences between the experimental and numerical results occur, they assist in diagnosing experimental inaccuracies or revising the underlying assumptions in the numerical model.

5.1 Experimental model and setup

In this section, we experimentally evaluate the effectiveness of replacing traditional rectangular stiffeners with ABH stiffeners in mitigating the vibrational response of the beam. The proposed experimental models are presented in Fig. 5.1 shows the two beams with rectangular and ABH stiffeners. Three different cases are analysed, stiffeners without damping layer, with VLs, and with CVLs. All three cases are subjected to an impact force applied at two positions, at $x = 0$ m (on the stiffener) or $x = d/2$ (between two stiffeners). The distance between stiffeners d is 0.2 m. The vibrational response is measured by seven accelerometers placed on the beam right above the stiffeners and between the subsequent stiffeners as shown in Fig. 5.1. The accelerometers are equally spaced by $d/2$. The geometrical properties of both beams are detailed in Table 5.1.

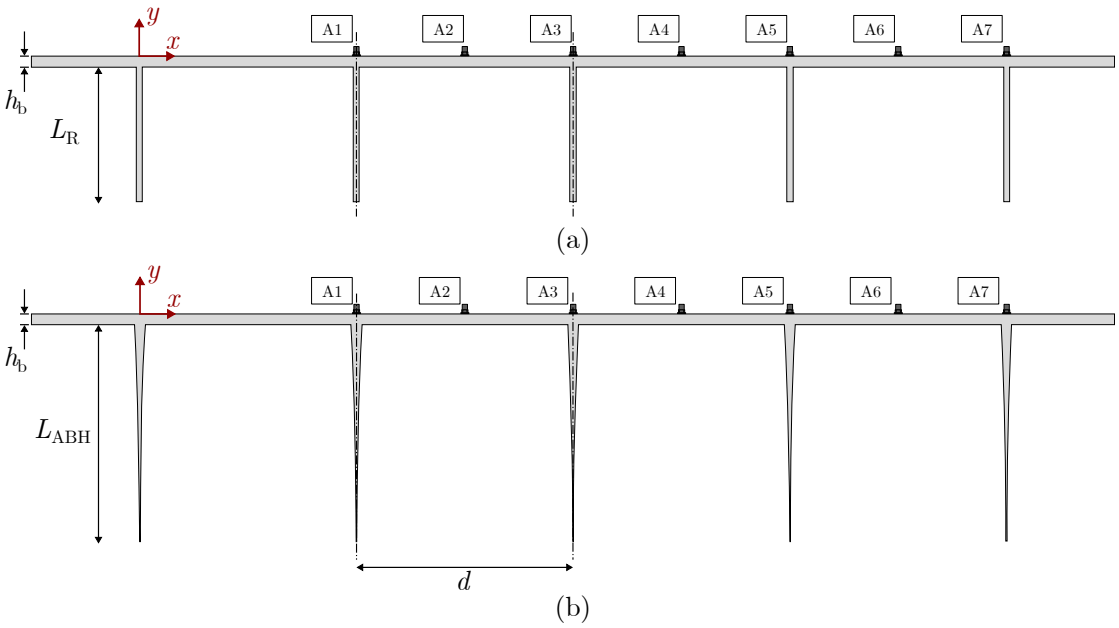

FIGURE 5.1: Schematic of the finite beams and respective accelerometer positions. (a) rectangular-stiffened beam and (b) ABH-stiffened beam.

The VL and CL have the same length in both stiffeners as shown in Fig. 5.2. The CVL is composed of the VL with an aluminium sheet as a constrained layer bonded to the

TABLE 5.1: Geometrical properties of the beam and stiffeners.

Parameters	Rectangular stiffener	ABH stiffener	Beam
Thickness ($h_{\mathrm{r,ABH,b}}$)	0.007 m	0.010 m	0.010 m
Length ($L_{\mathrm{r,ABH}}$)	0.124 m	0.200 m	1.000 m
Tip thickness (h_{tip})	-	0.006 m	-
Damping layer thickness (h_{dl})	0.004 m	0.004 m	-
Damping layer length (L_{dl})	0.124 m	0.124 m	-

VL to enhance the damping effect by constraining the deformation of the VL. Since the constrained layer is a stiff material, its thickness must be carefully considered to avoid interfering with the proposed ABH mechanism of a vibrating tip and dissipation through the damping layer.

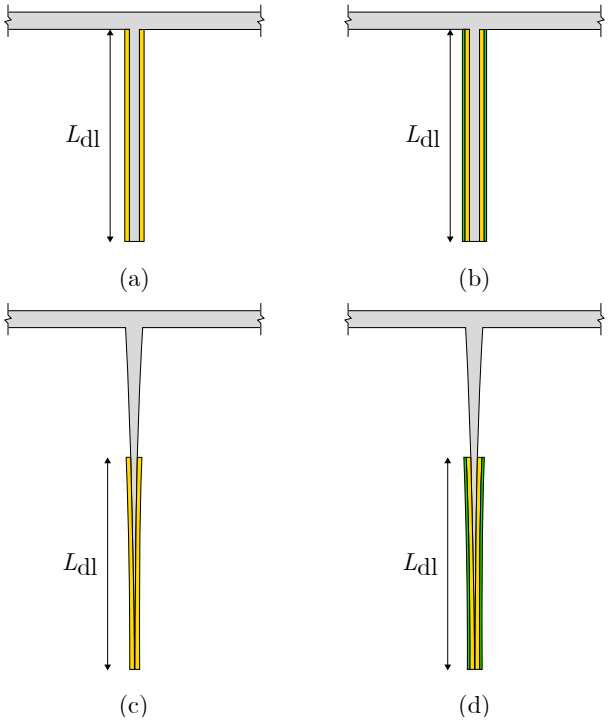

FIGURE 5.2: Schematic of the rectangular stiffeners with (a) VLs and (b) CVLs; schematic of the ABH stiffeners with (c) VLs and (d) CVLs. The viscoelastic material is represented by the yellow layer and the constrained material by the green layer.

Both stiffened beams were fabricated from a three-millimeter 316 stainless steel sheet by a OMAX 55100 Precision JetMachining Centre at University of Technology Sydney (UTS) Tech Lab shown in Fig. 5.3(a). The abrasive waterjet machine operates by pressurising water up to 50,000 psi, which is then mixed with abrasive particles like garnet to form a high-velocity jet capable of cutting through various materials as shown by Fig. 5.3(b). This jet is directed through a nozzle at the material placed on a support bed, following programmed paths for precise cuts (tolerance ±0.025 mm).

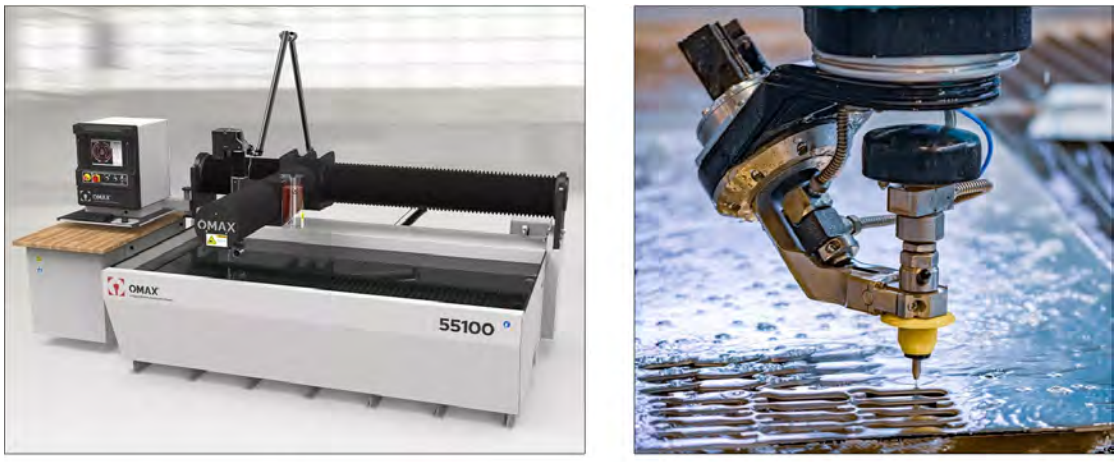

(a) (b)

FIGURE 5.3: (a) The OMAX 55100 JetMachining Center utilized to fabricate the beams with rectangular and ABH stiffeners at UTS Tech Lab, from Ref. [85] . (b) Waterjet machine in operation, from Ref. [1].

Fig. 5.4 shows both rectangular and ABH-stiffened beams. The viscoelastic material utilised in both VL and CVL, is butyl rubber with 4 mm thickness and has the same length as the rectangular stiffener as previously shown in Fig. 5.2. The constrained layer is made of an aluminium sheet of 0.1 mm.

The experimental setup is presented in Fig. 5.5. The beam was suspended by rubber strings at each end to mimic a free-free boundary condition, as highlighted by the white markers. Seven miniature accelerometers, Brüel & Kjær (B&K) 4397, were connected to the top part of the beam, and a Scalable Automatic Modal Hammer SAM1 from Polytec was utilised to excite the beam by an impact point force. The data acquisition (DAQ) hardware and signal post-processing module were used with the B&K LAN-XI DAQ hardware (type 3160) and the PULSE platform.

FIGURE 5.4: Fabricated stiffened beams. Top figure presents the rectangular-stiffened beam, and bottom figure presents the ABH-stiffened beam.

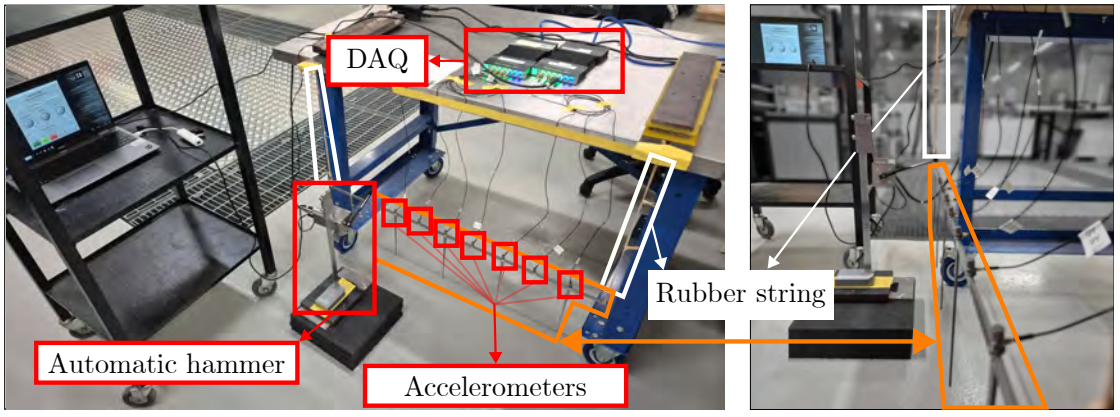

FIGURE 5.5: Experimental setup of the two finite stiffened beams, highlighting the automatic hammer, acceleromenters, DAQ and boundary contidions.

5.2 Experimental results

In order to obtain the results presented in the following subsections, an arithmetic mean of the accelerance FRF was calculated from 50 runs of the experiment for each case, subjected to the two points of excitation. The excitation was applied using an instrumented hammer equipped with a force transducer, enabling accurate measurement of the input signal. The measurements were conducted over 10 seconds with a resolution of 3.0518×10^{-5} seconds. The time domain acceleration signals were first preprocessed to remove any direct current offset, which is a constant component or bias that can shift the

signal vertically and distort the analysis. To minimise spectral leakage without significantly distorting the amplitude and decay characteristics inherent in impact-generated vibration responses, a Hamming window was applied to each signal prior to transforming them into the frequency domain using the Fast Fourier Transform (FFT). This choice ensures a balanced trade-off between reducing spectral leakage and maintaining accurate modal estimations, particularly given the complexity introduced by the ABH stiffeners and the favourable characteristics of the piezoelectric sensors used. As an example of the obtained results and the considered average, Fig. 5.6 shows the accelerance FRF and coherence between the impact hammer signal and accelerometers' signals of the ABH-stiffened beam subjected to the impact point force at $x = 0$ m. Results of all 50 runs are presented by black curves. The accelerance FRF mean result is presented by a red curve. The data from all 50 runs are clustered tightly around the mean value which is an indication of good stability and repeatability of the measurements for all 50 runs.

Fig. 5.6(a) shows the accelerance of the beam with ABH stiffeners without damping layers and the related coherence of signals. Coherence values close to 1 indicate a strong linear relationship between the impact force and the measured response, suggesting reliable data. The high coherence observed in most of the frequency range confirms the consistency of the measurements. However, the low values occur at frequencies where the correlation is weaker, possibly due to noise. It is noted that the low values of coherence occur at the same frequencies of anti-resonances shown in the accelerance FRF. Therefore, it does not affect the aim of the experimental analysis, which is to demonstrate the vibration mitigation of the beam using ABH stiffeners. Figs. 5.6(b) and (c) show the results for the cases with VLs and CVLs, respectively. It can be seen that for both cases, the accelerance FRF has less anti-resonances which led the coherence to be close to 1 in almost the entire analysed frequency range.

5.2.1 Damping layer effect

Fig. 5.7 presents a comparison of the rectangular-stiffened beam for three cases, without damping layers, with VLs and CVLs. Figs. 5.7(a) and (b) show the accelerance FRF of the stiffened beam from accelerometers A1 and A7 at positions $x = d$ and $x = 4d$, respectively. As highlighted in Chapter 4, the addition of damping layers led to greater mitigation of the vibrational response in the structure with ABH stiffeners than in

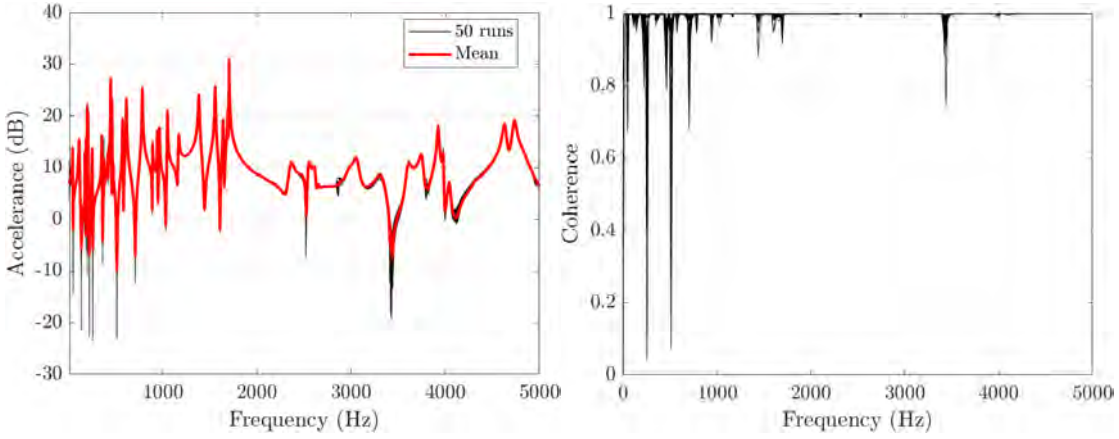

(a)

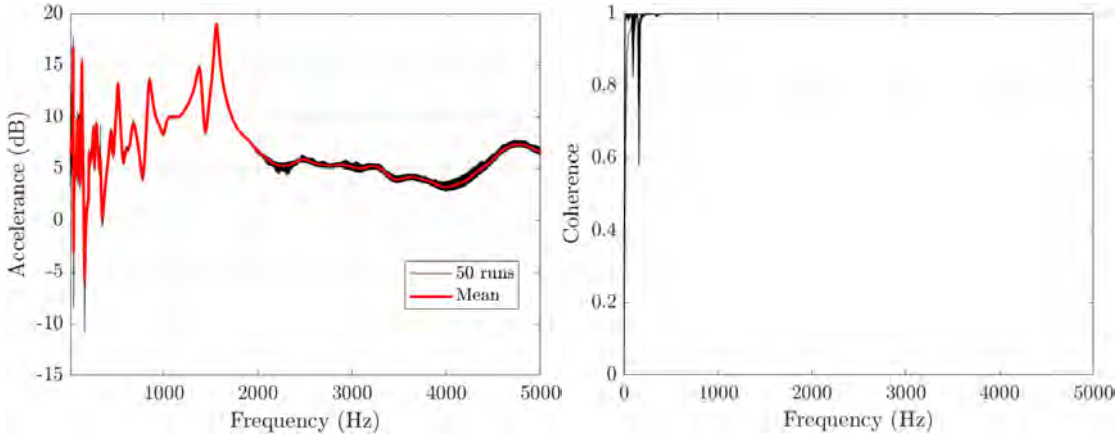

(b)

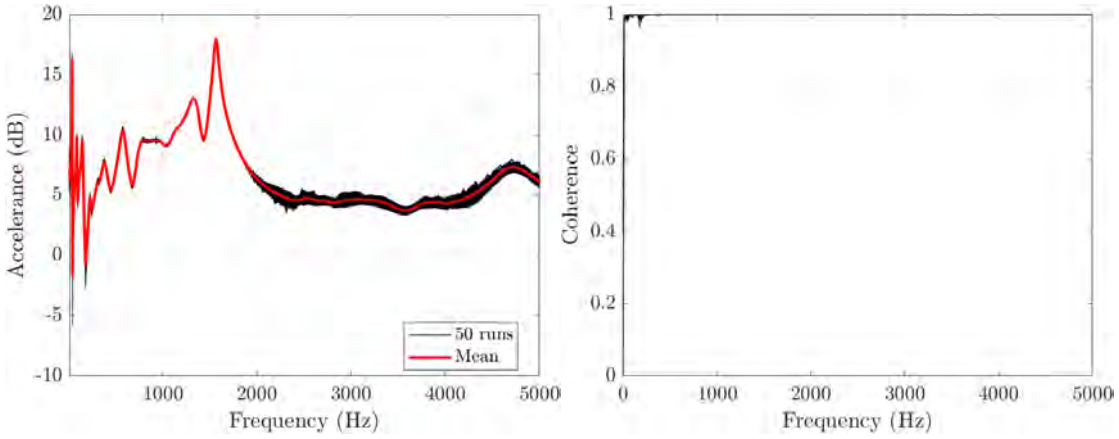

(c)

FIGURE 5.6: Accelerance FRF and coherence between the input force and accelerometer signals (A1) for ABH-stiffened beam (a) without damping layer, (b) with VLs and (c) with CVLs. The 50 runs are presented by the black curves and the accelerance mean result by the red curve. (dB, ref 1 $m.s^{-2}.N^{-1}$).

the structure with rectangular stiffeners. As shown in Section 4.2, for the rectangular-stiffened case the mitigation effect caused by damping layers was noticed only in the high frequency range (above 4000 Hz). This is consistent with the results shown in Fig. 5.7 in terms of accelerance considering the excitation point at $x = 0$ m. Figs. 5.7 also shows that the resonance peaks are shifted to the left compared to the case without damping layers, that is a result of the added mass of the VLs and CVLs. The system's dynamic response is slightly mitigated at the peaks up to 1500 Hz, and then the damping effect starts to increase resulting in a noticeable vibration reduction around 1900 Hz and 4200 Hz. Similarly, Figs. 5.7(c) and (d) show the accelerance results considering the beam with rectangular stiffeners excited by an impact force at $x = 0.5d$. Regarding the comparison of the VLs and CVLs, it is noted that the constrained layer is more effective in lowering the accelerance FRF, in comparison with VLs and the case without damping layers.

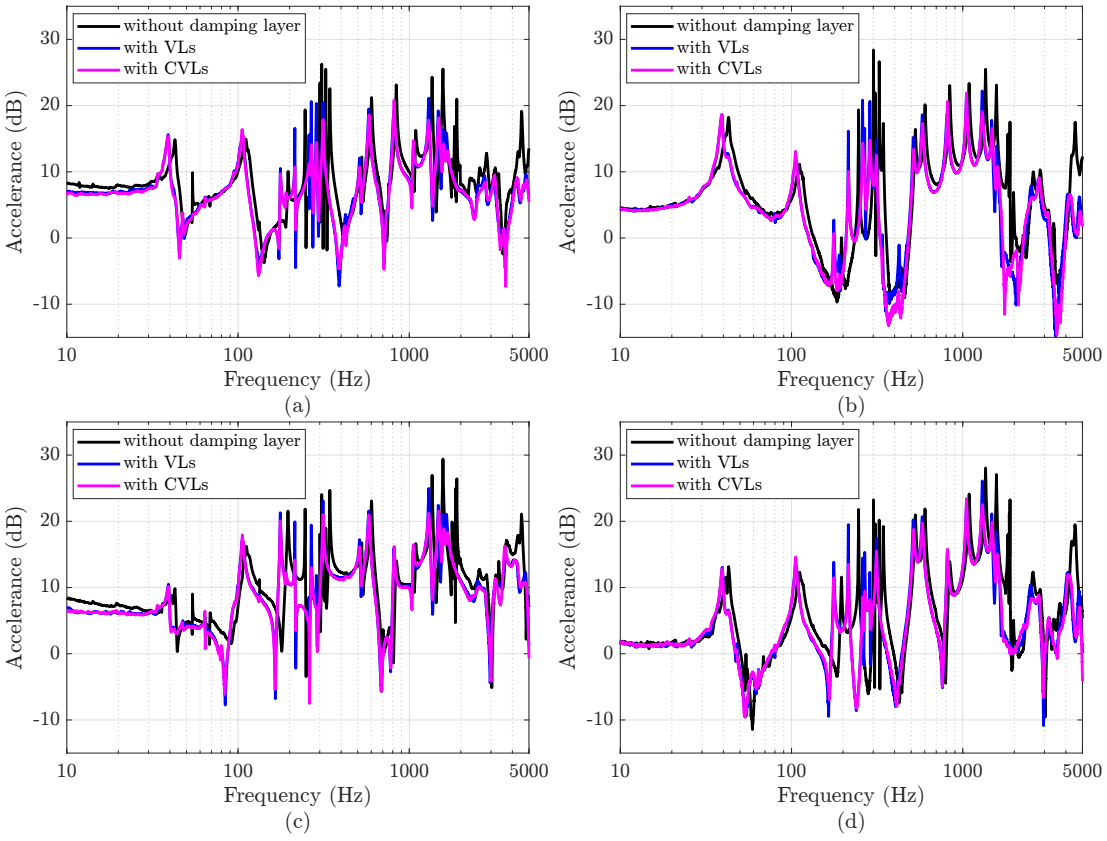

FIGURE 5.7: Accelerance FRF considering a beam with rectangular stiffeners excited by an impact force at $x = 0$ m for the (a) accelerometer A1 ($x = d$) and (b) accelerometer A7 ($x = 4d$). Accelerance FRF considering the impact force at $x = 0.5d$ for the (c) accelerometer A1 ($x = d$) and (d) accelerometer A7 ($x = 4d$). (dB, ref 1 m.s^{-2}.N^{-1}).

Similarly, Fig. 5.8 presents a comparison of the ABH-stiffened beam for three cases, without damping layers, with VLs, and with CVLs. Figs. 5.8(a) and (b) show the accelerance FRF of the stiffened beam from accelerometers A1 and A7 at positions $x = d$ and $x = 4d$, respectively. It can be noted that, the same frequency shift that occurred for the case with rectangular stiffeners (Fig. 5.7) when comparing the cases with VLs and CVLs with the case withouth damping layers is also present in the ABH-stiffened beam FRFs. Noticeably, the addition of damping results in a mitigation of the vibrational response for frequencies above 200 Hz. The resonance peaks are significantly damped in almost the entire frequency range, with a difference up to 29 dB at 460 Hz when comparing the case with CVLs and without damping layer in Fig. 5.8(b). This indicates that the constrained layer enhances the damping effect by restricting the deformation of the viscoelastic layer, leading to improved energy dissipation. Similarly, Figs. 5.8(c) and (d) show the accelerance FRFs considering the excitation at $x = 0.5d$ for the ABH-stiffened case. It is noted that the addition of VLs and CVLs was able to mitigate several resonance peaks across the analysed frequency range. These findings highlight that the addition of damping layers is significantly more effective in the ABH-stiffened system than in the rectangular-stiffened one.

5.2.2 Comparison of the vibrational responses between the rectangular-stiffened and ABH-stiffened beams

The comparison of the vibrational responses of the beams with rectangular and ABH stiffeners is divided into three cases: without damping layer, with VLs and CVLs. All cases consider both excitation positions at $x = 0$ m and $x = 0.5d$. The vibrational responses are analysed in terms of accelerance FRFs for the seven accelerometers and transmissibility between accelerometer A1 and A7.

5.2.2.1 Case 1: Stiffened beams without damping layers

Fig. 5.9 shows the accelerance FRFs of all seven accelerometers for the stiffeners without damping layers. Figs. 5.9(a) and (b) present the response considering the beam excited by an impact force at $x = 0$ m for the rectangular-stiffened and ABH-stiffened cases, respectively; and Figs. 5.9(c) and (d) present the response considering the beam excited by an impact force at $x = 0.5d$ m for the rectangular-stiffened and ABH-stiffened cases,

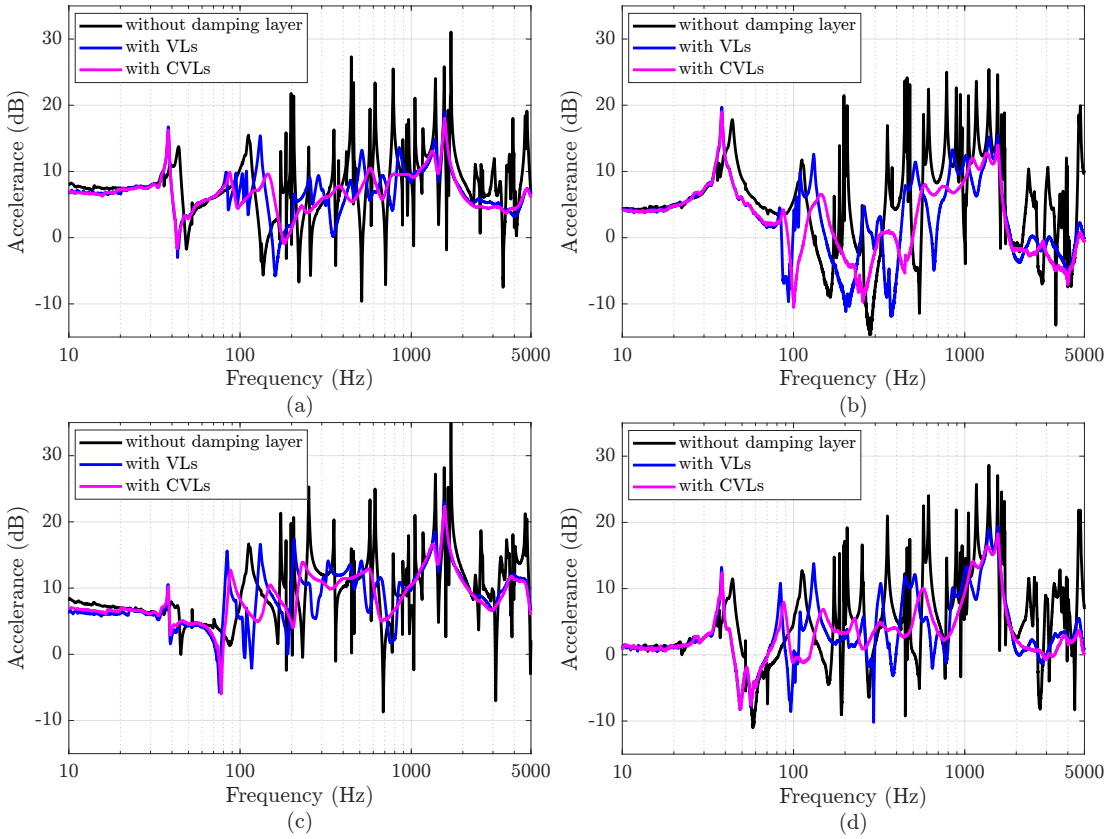

FIGURE 5.8: Accelerance FRF considering a beam with ABH stiffeners excited by an impact force at $x = 0$ m for the (a) accelerometer A1 ($x = d$) and (b) accelerometer A7 ($x = 4d$). Accelerance FRF considering the impact force at $x = 0.5d$ for the (c) accelerometer A1 ($x = d$) and (d) accelerometer A7 ($x = 4d$). (dB, ref 1 m.s^{-2}.N^{-1}).

respectively. Several resonance peaks can be seen in all four responses as the colour maps changes from green to red. As shown in Figs. 5.7 and 5.8 for the case without damping layers there are several peaks at low frequency specially bellow 2000 Hz. This cluster of peaks is easily observed in all responses shown in Fig. 5.9. One can note that responses of the ABH-stiffened beam ((b) and (c)) shows a higher number of peaks in the entire frequency range, and notably from 100 Hz to 1900 Hz. This is a result of the ABH thinner shape that induces a higher number of resonances. Since this is not an ideal ABH (i.e. it has a non-zero thickness at the tip), and neither has a mechanism to dissipate the energy at the tip (due to the lack of damping layers), higher levels of vibrations are concentrated at this region leading consequently to higher levels of accelerance for all seven accelerometers. It can be seen that the response for odd accelerometers numbers A1, A3, A5 and A7, have a lower response when compared to even numbered accelerometers. This is due to the fact that these accelerometers are located directly above the stiffeners, which is more rigid and less prone to vibration

location.

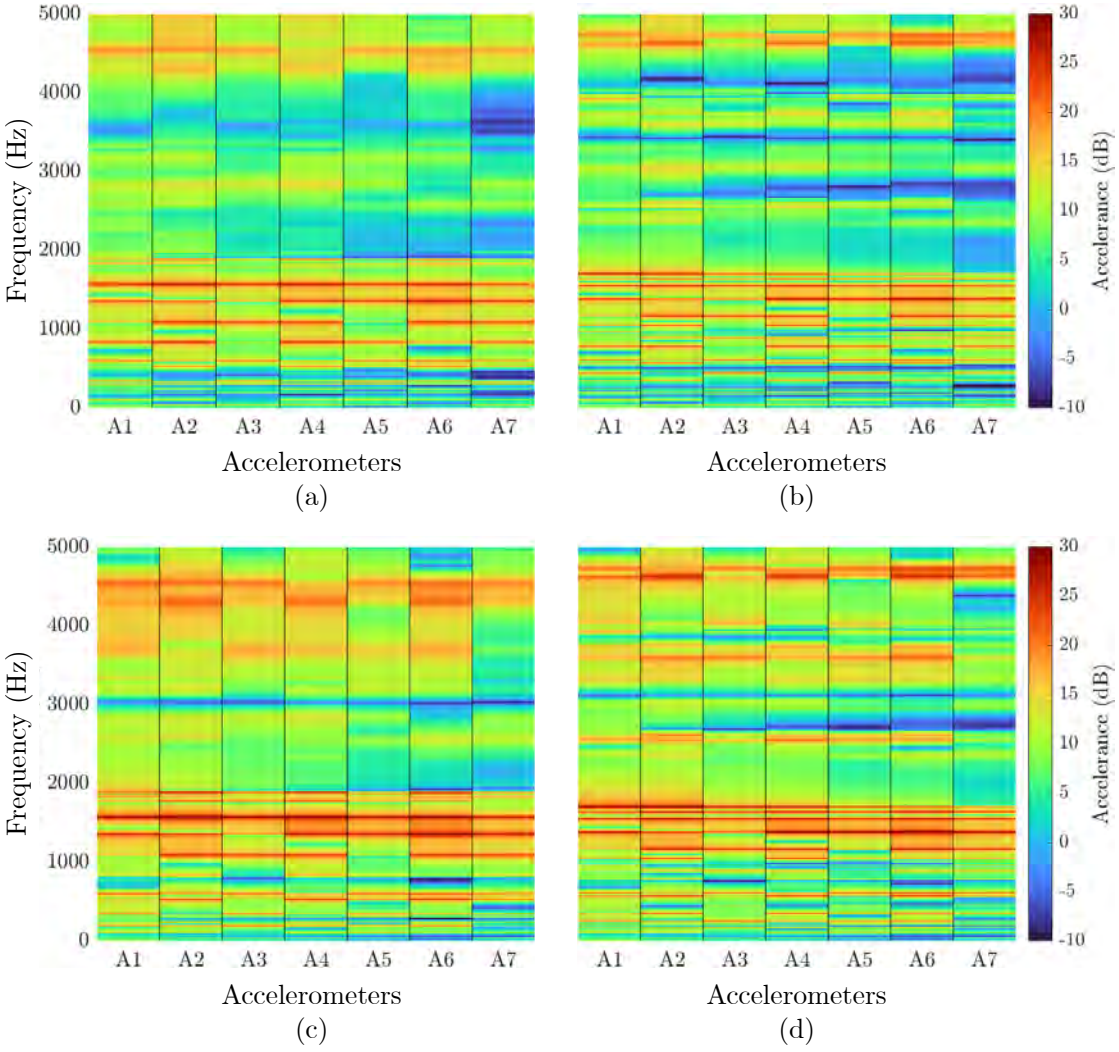

FIGURE 5.9: Accelerance FRF for each accelerometer considering a beam excited by an impact at $x = 0$ m and stiffened with (a) rectangular stiffeners without damping layers and (b) ABH stiffeners without damping layers. Accelerance FRF for each accelerometer considering a beam excited by an impact at $x = 0.5d$ m and stiffened with (c) rectangular stiffeners without damping layers and (d) ABH stiffeners without damping layers. (dB, ref 1 m.s^{-2}.N^{-1})

Fig. 5.10 shows the comparison between the beams with rectangular and ABH stiffeners without damping layers in terms of transmissibility. The transmissibility is calculated from the ratio of the squared accelerance responses for the accelerometers A1 and A7. Figs. 5.10(a) and (b) presents the transmissibility of both stiffened beams considering the excitation at $x = 0$ m and $x = 0.5d$, respectively. One can note that at low frequencies (bellow 170 Hz) both responses are similar, due to the same area and moment of inertia of both stiffeners, which result in a similar static stiffness and mass. Above

170 Hz, the beam with ABH stiffeners is characterised by an increased number of resonance peaks in comparison to the rectangular stiffened beam, as shown in Fig. 5.9 for the seven accelerometers. The transmissibilities of both beams for the two points of excitation present a similar trend and overall vibration levels. This similarities lead to easy visualisation of the increased number of resonance peaks in the ABH-stiffened beam response. This outcome was expected, as the vibration mitigation typically associated with the ABH effect was not activated due to the non-ideal nature of the ABH stiffener and the absence of damping layers. With the addition of damping layers, the expected ABH effect of mitigating the vibrational response, as described in the literature, occurs and will be investigated further in what follows.

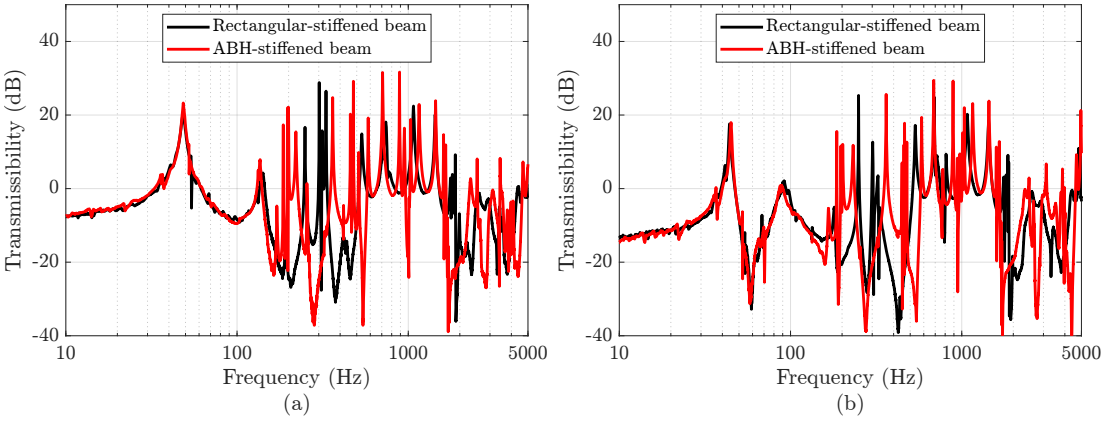

FIGURE 5.10: Comparison of transmissibility between accelerometers A1 and A7, considering the stiffened beam with stiffeners without damping layers excited at (a) $x = 0$ m and (b) $x = 0.5d$.

5.2.2.2 Case 2: Stiffened beams with VLs

Fig. 5.11 shows the accelerance FRFs of all seven accelerometers for the stiffeners with VLs. Figs. 5.11(a) and (b) present the response considering the stiffened beams excited by an impact force at $x = 0$ m for the rectangular-stiffened and ABH-stiffened cases, respectively; and Figs. 5.11(c) and (d) present the response considering the beam excited by an impact force at $x = 0.5d$ m for the rectangular-stiffened and ABH-stiffened cases, respectively. The accelerance FRFs of all cases have a lower amount of peaks when compared to the case without damping layers shown in Fig. 5.9. The clustering of peaks is clearly visible from 100 Hz to 1800 Hz, also highlighting the higher response levels for accelerometers located in between stiffeners (A2, A4 and A6). It is noted that the rectangular stiffened case exhibits a distinctively lower response around 3800 Hz considering

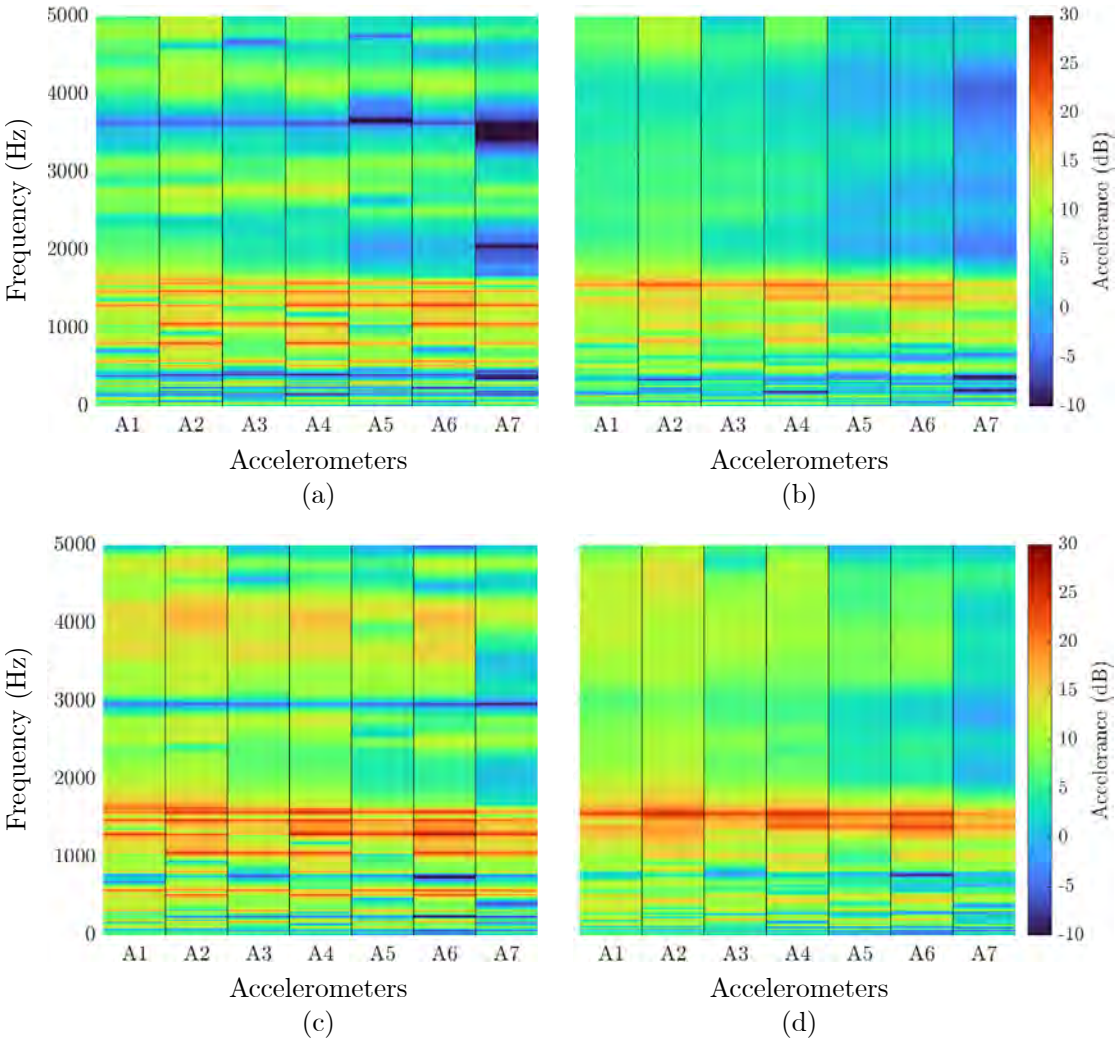

FIGURE 5.11: Accelerance FRF for each accelerometer considering a beam excited by an impact at $x = 0$ m and stiffened with (a) rectangular stiffeners with VLs and (b) ABH stiffeners with VLs. Accelerance FRF for each accelerometer considering a beam excited by an impact at $x = 0.5d$ m and stiffened with (c) rectangular stiffeners with VLs and (d) ABH stiffeners with VLs. (dB, ref 1 m.s^{-2}.N^{-1})

the case with excitation at $x = 0$ m (Figs. 5.11(a)) and around 3000 Hz for the case with the excitation at $x = 0.5d$ (Figs. 5.11(b)). Another two noticeable attenuation bands are visible considering the response for the accelerometer A7 in Figs. 5.11(a), approximately from 1800 Hz to 2200 Hz and from 3200 Hz to 3900 Hz.

The accelerance FRF response of the ABH-stiffened beam ((b) and (d)) shows that the addition of damping was able to mitigate a large number of resonance peaks in the entire frequency range. One can note that the ABH-stiffened beam response presents an overall lower response for all accelerometers when comparing all accelerance maps. It is also noted that the ABH-stiffened beam response is mitigated as the accelerometer is further

away from the source. This pattern is clearly visible in Figs. 5.11(c) and (d) with a transition from green to blue from accelerometer A1 to accelerometer A7 above 1800 Hz. This pattern of mitigation is not clearly visible considering the case with rectangular stiffeners (Figs. 5.11(c) and (d)). Similarly, considering results below 1800 Hz, a small mitigation pattern can be observed for the case with ABH stiffeners transitioning from dark red to orange/yellow. However, this pattern is interrupted by higher levels of vibration for the accelerometers located between stiffeners.

The transmissibilities of the stiffened beams with VLs excited by an impact force at $x = 0$ m and $x = 0.5d$ are shown in Figs. 5.12(a) and (b), respectively. Similarly, to the case without damping layers both stiffened beams present comparable results at low frequencies (bellow 90 Hz). Above 200 Hz, vibrational responses of the rectangular-stiffened and ABH-stiffened beams begin to differ and it is visible that above this frequency the ABH-stiffened beam mitigates the response. This mitigation occurs below the cut-on frequency ABH based on Eq. 4.22, $f_{\text{cut}} = 2264$ Hz. Similarly, in Chapter 4, the infinite heavy fluid-loaded plate with ABH stiffeners showed systematic mitigation when excited below the cut-on frequency, with the onset around the first flexural natural frequency of the stiffener. For the present case, the first flexural natural frequency of the ABH stiffener with VL is 230 Hz, obtained through eigenfrequency analysis using COMSOL Multiphysics™.

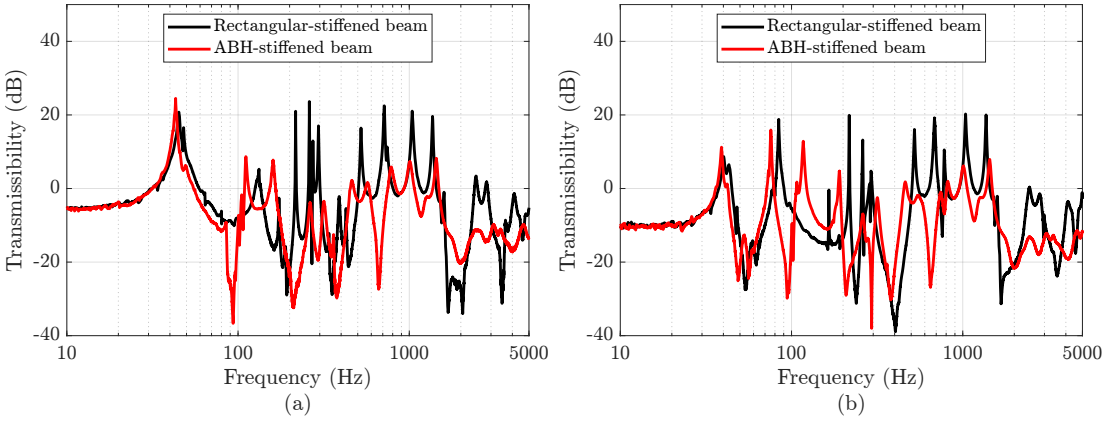

FIGURE 5.12: Comparison of transmissibility between accelerometers A1 and A7, considering the stiffened beam with stiffeners with VLs excited at (a) $x = 0$ m and (b) $x = 0.5d$.

Fig. 5.12 shows that the transmissibility levels for ABH-stiffened beam are mostly lower than that of the rectangular-stiffened beam. It is also noted that there are two wide frequency bands of attenuation from 200 Hz to 1600 Hz and 2000 Hz to 3000 Hz, reducing

the response by up to 23 dB at 660 Hz in Fig. 5.12(a) and 30 dB at 710 Hz in Fig. 5.12(a). These findings highlight the capabilities of the ABH stiffener in mitigating the vibrational response when compared to an equivalent rectangular stiffener, demonstrating that the addition of VLs is not as effective in mitigating the response of the beam with rectangular stiffeners as it is with the ABH-stiffened beam.

5.2.2.3 Case 3: Stiffened beams with CVLs

Considering the stiffeners with CVLs, Figs. 5.13(a) and (b) show the response considering the stiffened beams excited by an impact force at $x = 0$ m for the rectangular-stiffened and ABH-stiffened cases, respectively; and Figs. 5.13(c) and (d) present the response considering the beam excited by an impact force at $x = 0.5d$ m for the rectangular-stiffened and ABH-stiffened cases, respectively. Similarly to the addition of VLs, the accelerance FRFs of all cases have a lower amount of peaks when compared to the case without damping layers shown in Fig. 5.9. When comparing the accelerance maps shown in Fig. 5.11 to the present case, it can be noted that the frequency band from 100 Hz to 1800 Hz with several peaks was attenuated for all cases, and this attenuation is more pronounced in the ABH-stiffened cases ((b) and (d)). The ABH-stiffened cases at this frequency band, present a blurred colour map transitioning from green to red, a similar effect as presented in the previous Chapter in Fig. 4.7.

Fig. 5.14 shows the transmissibility considering both stiffeners with CVLs. The results of the stiffened beams excited by an impact force at $x = 0$ m and $x = 0.5d$ is shown in Figs. 5.14(a) and (b), respectively. The transmissibility results of both cases, are similar to the previous case (with VLs) which is consistent with the results shown in Figs. 5.7 and 5.8. As demonstrated in the previous results (for cases without damping layers and with VLs), the first resonance peak shows similar behaviour for both the rectangular-stiffened beam and the ABH-stiffened beam, whereas the second peak is significantly mitigated in the ABH-stiffened beam. This is observed in Fig. 5.14(a) which shows at 100 Hz an trough followed by a small peak (difference of 13 dB between the black and red curves).

The previously noted wide attenuation bands in the case with VLs are split into three frequency bands for the case with CVLs, from 200 Hz to 300 Hz, from 500 Hz to 1700 Hz, and from 2100 Hz to 3100 Hz. The addition of the constrained layer resulted in a

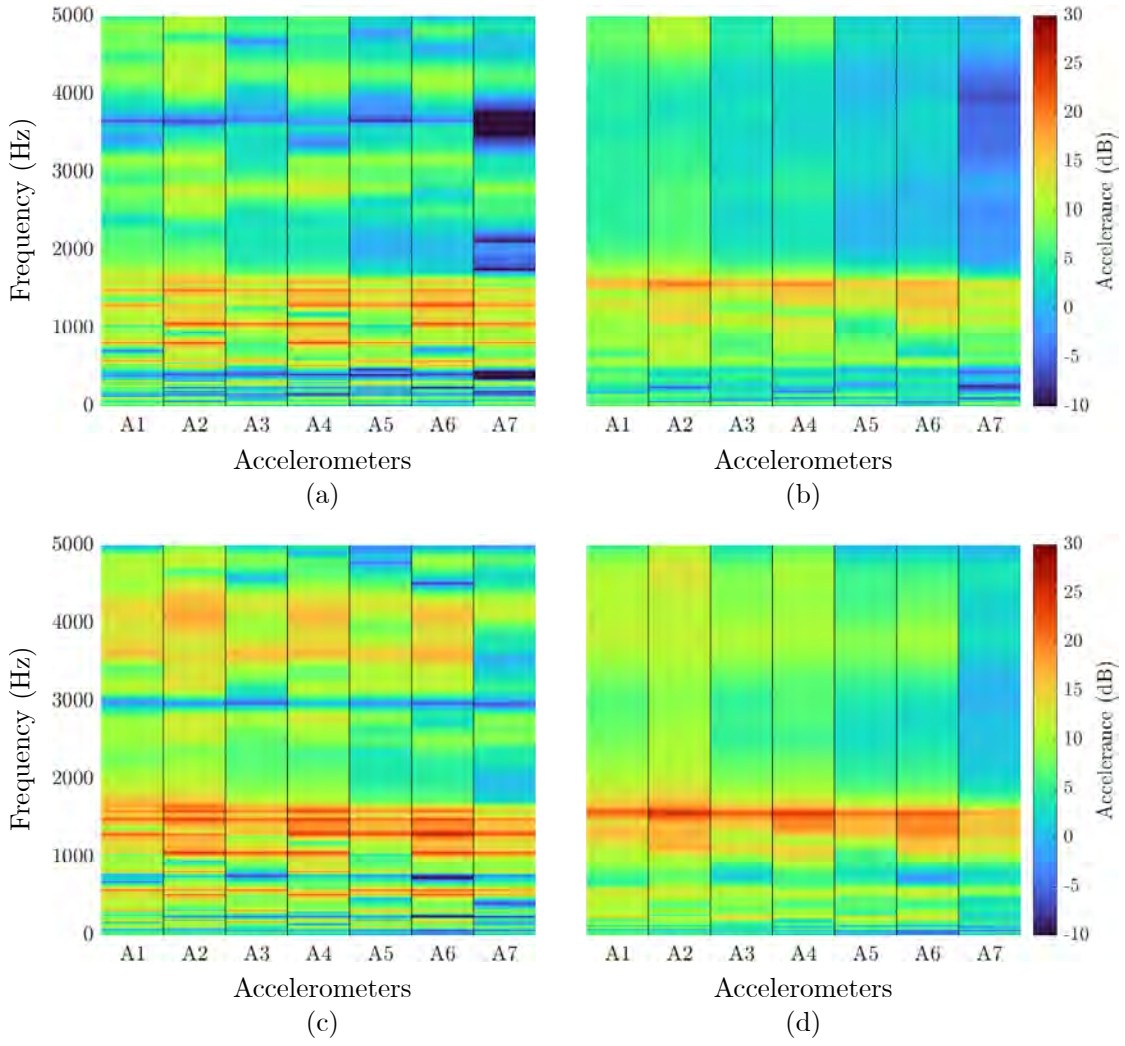

FIGURE 5.13: Accelerance FRF for each accelerometer considering a beam excited by an impact at $x = 0$ m and stiffened with (a) rectangular stiffeners with CVLs and (b) ABH stiffeners with CVLs. Accelerance FRF for each accelerometer considering a beam excited by an impact at $x = 0.5d$ m and stiffened with (c) rectangular stiffeners with CVLs and (d) ABH stiffeners with CVLs. (dB, ref 1 m.s^{-2}.N^{-1})

mitigation of the overall response for both cases; however, the beam with ABH stiffeners presented a lower vibrational response when compared against the rectangular-stiffened beam, reaching up to a 33 dB difference at 261 Hz. The results from the ABH-stiffened beam exhibit a lower vibrational response, demonstrating the effectiveness of the ABH stiffeners in mitigating vibration. It is noted that with the CVLs, the rectangular-stiffened beam shows deeper troughs in the vibrational response, but the overall response is higher than that of the ABH-stiffened beam.

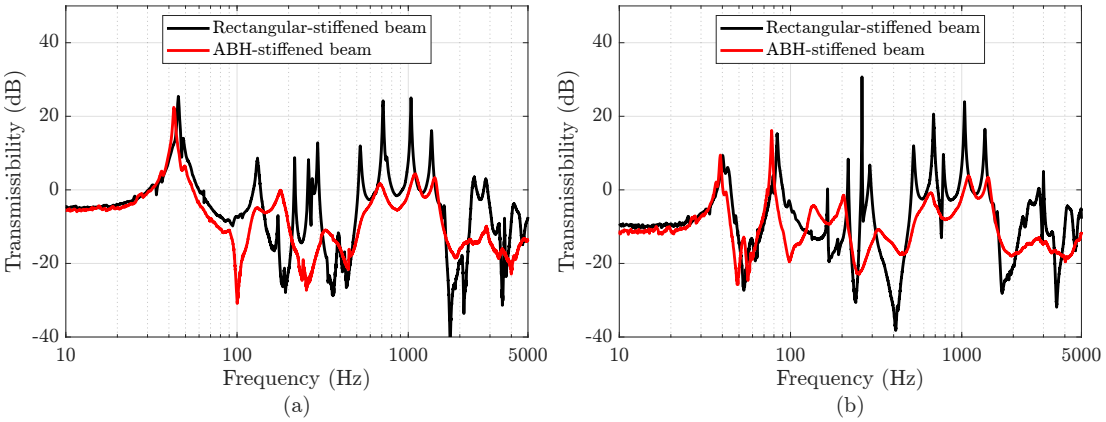

FIGURE 5.14: Comparison of transmissibility between accelerometers A1 and A7, considering the stiffened beam with stiffeners with VLs excited at (a) $x = 0$ m and (b) $x = 0.5d$.

5.3 Numerical Simulations

In this section, numerical models of the stiffened beams are developed using COMSOL Multiphysics™ to complement the physical testing. These simulations are employed to confirm the experimental data, and any discrepancies between the models and experiments can help identify potential errors in the experimental setup or assumptions within the numerical framework. Additionally, numerical models are crucial for performing parametric studies, allowing for the examination of how variations in material properties, boundary conditions, or geometry influence the system's vibrational behaviour, without the need for expensive and time-consuming experimental repetitions. The results from the numerical models are first compared with the experimental data, followed by a presentation of the mode shapes of the stiffened beams to gain a deeper understanding of the mechanisms by which the ABH and damping layers contribute to vibration mitigation.

The stiffened beams were modelled based on the schematic presented in Figs. 5.1 and 5.2 and using the geometrical properties of the beam and stiffeners presented in Table 4.2. The material properties used in the FE models are presented in Table 5.2. The damping loss factor was estimated based on the average of all peaks in the experimental FRF within the analysed frequency band. The mesh of the FE models were optimised based on the excitation frequency, ensuring a minimum of 10 elements per the smallest wavelength in the model. In the FE models, a spring force was applied at both ends of the beam to simulate the boundary conditions in the experiment, where the stiffened beam is

supported by two rubber strings at its ends. The spring force is defined as $F_{\text{spring}} = 50u_y$, where u_y represents the displacement in the y-direction, as per the coordinates in Fig. 5.1. Additionally, the weight of the accelerometers (2.5 g) was accounted for and applied on top of the beam at their respective positions. The stiffened beams for all cases are considered to be excited at $x = 0$ m.

Using the numerical model, the mode shapes for beams with rectangular and ABH stiffeners were obtained. In the next subsections, the mode shapes are represented in blue for the beam with rectangular stiffeners and in red for the beam with ABH stiffeners. The frequencies were selected based on resonance peaks in the low, mid, and high-frequency ranges that exhibit flexural deformation, as these could be linked to the FRFs, given that the accelerometers measure acceleration along the y-axis. The mode shapes observed for the rectangular-stiffened beam are consistent with those seen for the ABH-stiffened beam.

The following subsections present a comparison of the accelerance FRFs between the experimental data and the FEM simulations for all three cases. Additionally, the mode shapes of both stiffened beams are compared.

TABLE 5.2: Material properties of the stiffened beam, viscoelastic layer and constrained layer.

Parameter	**Beam**	**VLs**	**Constrained Layer**
Young's Modulus (Pa)	$185 \times 10^9\,(1 + 0.03\text{j})$	$0.8 \times 10^6\,(1 + 0.4\text{j})$	$69 \times 10^9\,(1 + 0.01\text{j})$
Mass Density (kg/m^3)	7800	1300	3000
Poisson's Ratio	0.3	0.45	0.33

5.3.1 Case 1: Stiffened beams without damping layers

Fig. 5.15 presents a comparison of accelerance FRFs between the experimental data and the results obtained using COMSOL Multiphysics™, considering the beam stiffened with rectangular (a,b) and ABH stiffeners (c,d). In both cases the stiffeners are assumed to have no damping layers. In both figures, the black curves represent the experimental data. The FEM results for the beam with rectangular stiffeners are shown in blue in Figs. 5.15(a) and (b) (for accelerometers A1 and A7, respectively), while the FEM results for the beam with ABH stiffeners are depicted in red in Figs. 5.15(c) and (d) (for accelerometers A1 and A7, respectively).

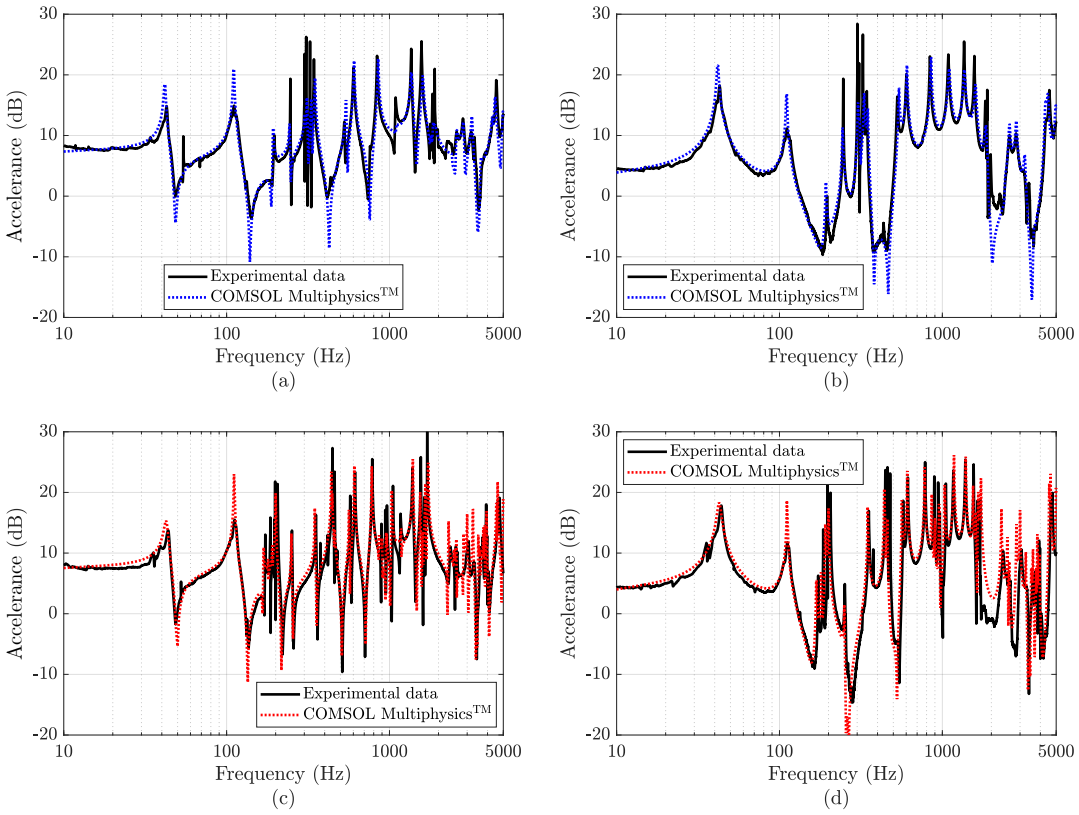

FIGURE 5.15: Comparison of accelerance FRFs between experimental data and FEM simulations for a rectangular stiffened beam without damping layers, measured at accelerometer positions (a) A1 and (b) A7. Results for the ABH-stiffened beam without damping layers are also shown for accelerometers (c) A1 and (d) A7. Both beams were excited at $x = 0$ m.

From Figs. 5.15(a) and (b) it can be noticed that the the FEM results exhibit good agreement with the experimental data in the low-frequency range (up to approximately 100 Hz), with both curves displaying consistent trends and magnitudes. In the mid-frequency range (100 Hz to 1000 Hz), the FEM model continues to align reasonably well with the experimental data, although minor deviations are noticeable, particularly in the magnitude of the resonance peaks. However, in the high-frequency range (above 1000 Hz), more significant discrepancies arise, showing that the numerical model may not fully capture the complex dynamics present at higher frequencies suggested by the difference between both curves. A similar trend to that in Figs. 5.15(a) and (b) is observed in Figs. 5.15(c) and (d). In the low-frequency range, the FEM model shows good agreement with the experimental data, accurately capturing the overall system dynamics. As the frequency increases to the mid-range, variations in magnitude of the resonance peaks can be noticed. These discrepancies become more prominent in

the high-frequency range, where the FEM model and experimental data show noticeable deviations. The FEM model demonstrates a smoother response compared to the sharper fluctuations exhibited by the experimental results, particularly around the troughs as shown around 2000 Hz in Fig. 5.15(d). The deviations observed in this frequency range are due to the difference between the experimental model and the FEM model. Overall, the FEM model was able to accurately describe the dynamic behaviour of the stiffened beams.

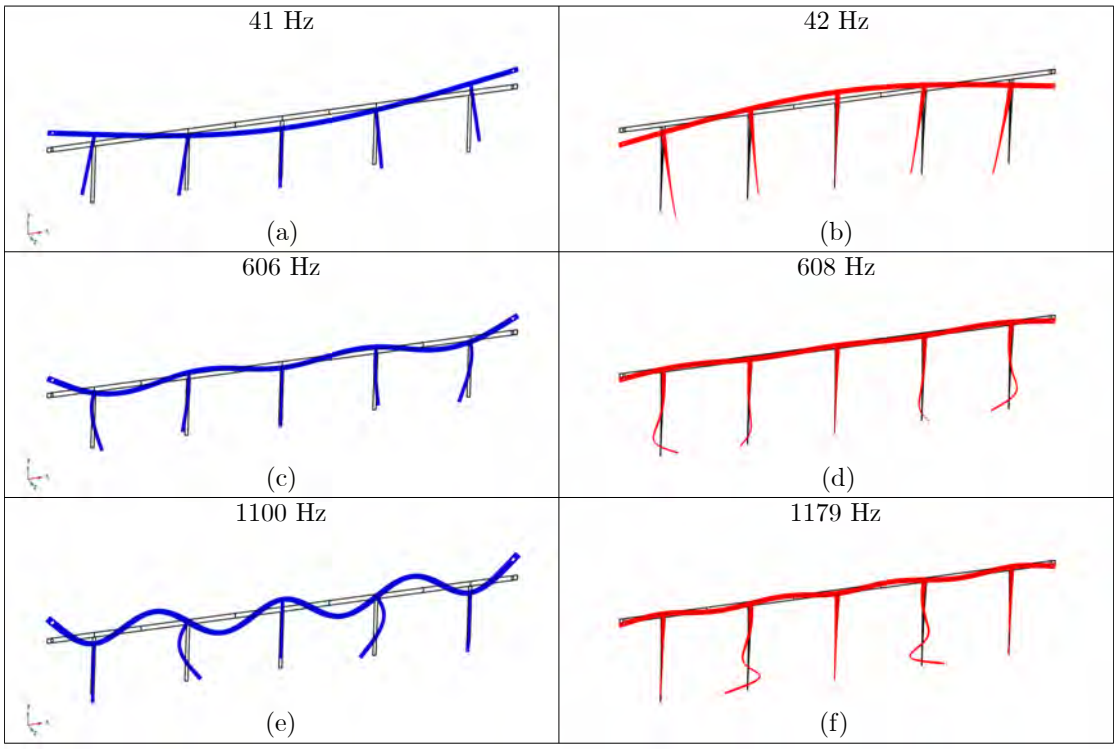

FIGURE 5.16: Mode shapes of the stiffened beam with rectangular stiffeners at (a) 41 Hz, (c) 606 Hz, and (e) 1100 Hz. Mode shapes of the stiffened beam with ABH stiffeners at (b) 42 Hz, (d) 608 Hz, and (f) 1179 Hz. Both beams are stiffened without damping layers.

The mode shapes depicted in Fig. 5.16 provide a comparison of the vibrational behaviour of beams stiffened with rectangular and ABH stiffeners without damping layers. In the low-frequency modes, 41 Hz and 42 Hz (Figs. 5.16(a) and (b)), both stiffened beams exhibit relatively uniform and symmetric vibrational modes, characteristic of standard flexural behaviour, where the vibrational energy is distributed along the length of the beam. This behaviour is also consistent with the accelerance FRF results shown in Fig. 5.15, where it can be observed that the first resonance peak occurs at these frequencies for both cases.

In the mid-frequency range, 606 Hz and 608 Hz, the difference between the two stiffened beams becomes evident. The rectangular stiffeners continue to produce mode shapes that distribute vibrational energy more evenly along the beam as observed in Fig. 5.16(c). By contrast, Fig. 5.16(d) shows the mode shape of the ABH-stiffened beam with a marked concentration of vibrational energy at the locations where the ABH profiles are applied. This concentration reflects the inherent design of ABH stiffeners, which are intended to trap the vibrational energy at the tip/edge, thereby reducing the overall amplitude of vibrations if there is a dissipation mechanism such as damping layers. In the high-frequency modes, Fig. 5.16(e) and (f), the divergence between the two stiffened beams becomes even more pronounced. The beam with rectangular stiffeners maintains its characteristic distributed deformation and nodes spread more uniformly across the beam. In contrast, the ABH-stiffened beam exhibits significant concentration of the deformation at the stiffeners.

5.3.2 Case 2: Stiffened beams with VLs

Fig. 5.17 presents the comparison of the accelerance FRFs between the experimental data and the results obtained using COMSOL Multiphysics™, for the beam stiffened with rectangular (a,b) and ABH stiffeners (c,d) with VLs. Figs. 5.17(a) and (b) present the results for the rectangular-stiffened beam at accelerometers A1 and A7, while Figs. 5.17(c) and (d) show the results for the ABH-stiffened beam at accelerometers A1 and A7.

Similar to the previous results for the case without damping layers, Figs. 5.17(a) and (b) shows the good agreement between the FEM model and the experimental data, particularly in the lower frequency range. Above 100 Hz, minor deviations between the FEM results and the experimental data become apparent, but the overall trend is well captured. This suggests that the damping layers and stiffener configuration are adequately modelled, although some discrepancies at higher frequencies may be attributed to limitations in modelling complex dynamic interactions. Fig. 5.17(c) and (d) presents a similar result for the case with ABH stiffeners, particularly showing a good agreement in the mid-frequency range.

The mode shapes presented in Fig. 5.18 compare the vibrational behaviour of beams stiffened with rectangular and ABH stiffeners, both with VLs. In the low-frequency modes, such as those around 40 Hz and 39 Hz (Figs. 5.18(a) and (b)), both beams exhibit

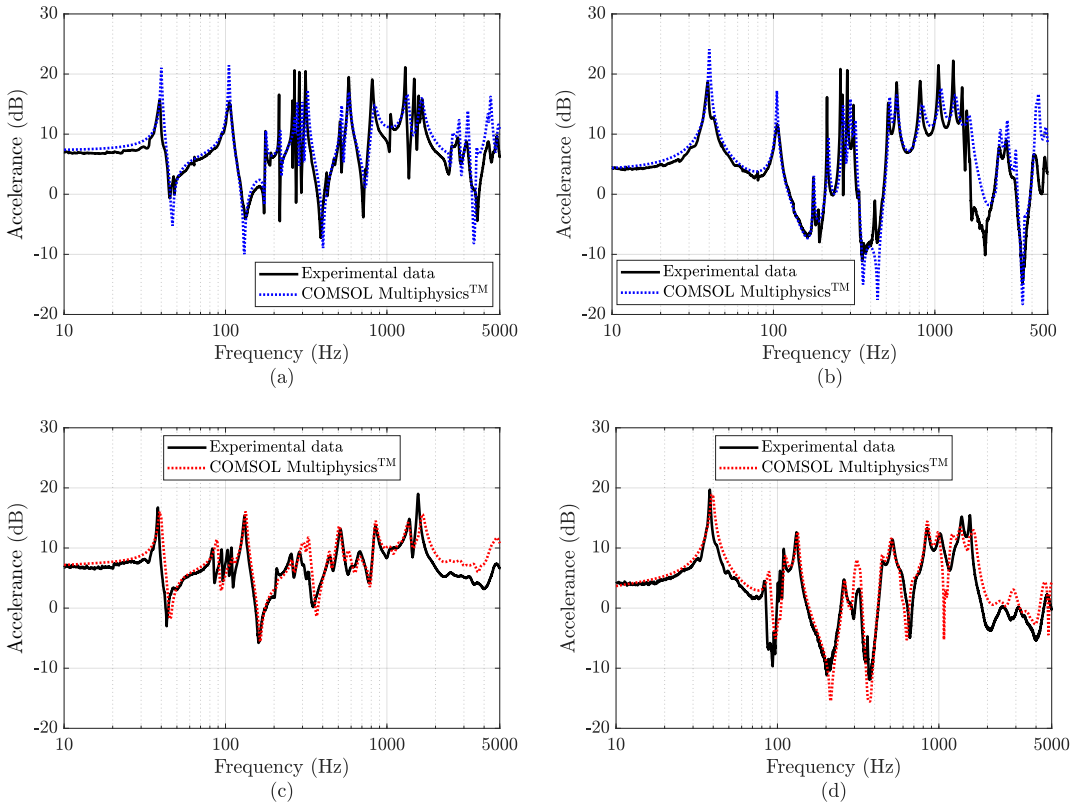

FIGURE 5.17: Comparison of accelerance FRFs between experimental data and FEM simulations for a rectangular stiffened beam with VLs, measured at accelerometer positions (a) A1 and (b) A7. Results for the ABH-stiffened beam with VLs are also shown for accelerometers (c) A1 and (d) A7. Both beams were excited at $x = 0$ m.

relatively symmetric vibrational modes similar to the case without damping layers. This is further confirmed by the first resonance peaks occurring at these frequencies for both cases in the accelerance FRFs results presented in Fig. 5.17.

As the frequency increases to the mid-frequency range, around 580 Hz (Figs. 5.18(c) and (d)), the differences between the two configurations become evident. The ABH stiffeners are able to concentrate the vibrational energy more effectively around the stiffener locations, allowing it to be dissipated by the VLs. This is demonstrated by the comparison of transmissibility between the two stiffened beams, as shown in Fig. 5.12. In contrast, the rectangular stiffeners result in a more distributed vibrational response along the length of the beam. This distinct localisation of vibrational energy at the ABH tip is consistent with its design purpose, which is to reduce vibration transmission and enhance damping performance by concentrating the energy at the tip or edge, as previously discussed. In the high-frequency modes, Figs. 5.18(e) and (f), the ABH-stiffened beam also exhibits

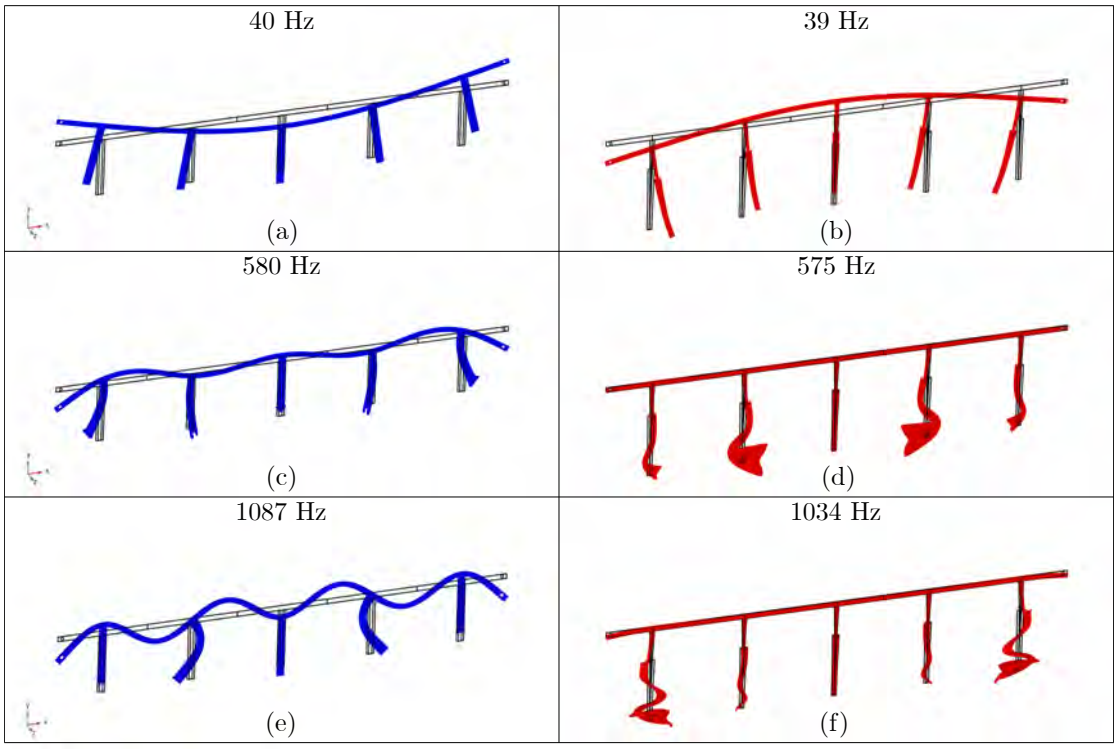

FIGURE 5.18: Mode shapes of the stiffened beam with rectangular stiffeners at (a) 40 Hz, (c) 580 Hz, and (e) 1087 Hz. Mode shapes of the stiffened beam with ABH stiffeners at (b) 39 Hz, (d) 575 Hz, and (f) 1034 Hz. Both stiffened-beams are considered to have VLs.

the energy highly localised near the ABH regions. The rectangular-stiffened beam, on the other hand, maintains a broader distribution of vibrational energy presenting a high deformation throughout the entire beam.

5.3.3 Case 3: Stiffened beams with CVLs

Fig. 5.19 presents the compararison of the accelerance FRFs between the experimental data and the results obtained using COMSOL Multiphysics™, for the beam stiffened with rectangular (a,b) and ABH stiffeners (c,d) with CVLs. Figs. 5.19(a) and (b) present the results for the rectangular-stiffened beam at accelerometers A1 and A7, while Figs. 5.19(c) and (d) show the results for the ABH-stiffened beam at accelerometers A1 and A7.

In Figs. 5.19(a) and (b), the FEM model for the beam with rectangular stiffeners presents a strong correlation with the experimental data, particularly in the lower frequency range. The model captures the primary resonance peaks, although minor deviations

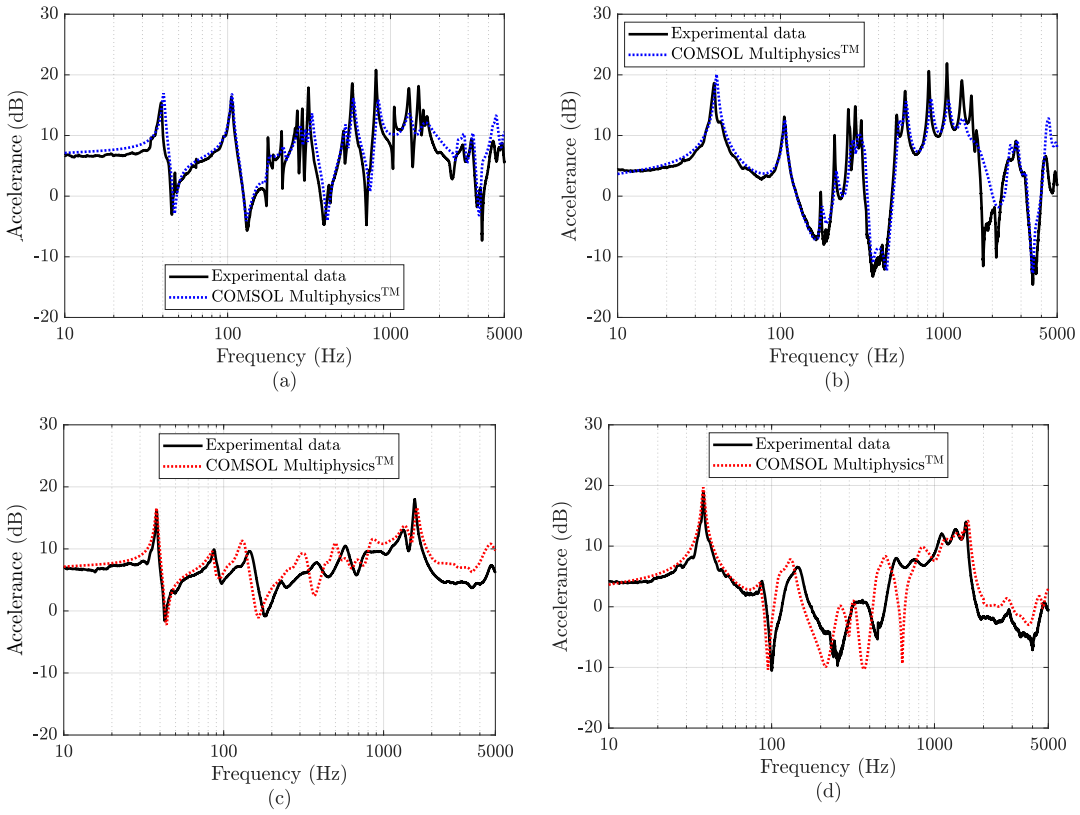

FIGURE 5.19: Comparison of accelerance FRFs between experimental data and FEM simulations for a rectangular stiffened beam with CVLs, measured at accelerometer positions (a) A1 and (b) A7. Results for the ABH-stiffened beam with VLs are also shown for accelerometers (c) A1 and (d) A7. Both beams were excited at $x = 0$ m.

emerge at higher frequencies (around 1080 Hz). These deviations may be attributed to the complexities introduced by the constrained viscoelastic layers, which introduce additional damping effects that the model may not fully capture at higher frequencies. In Figs. 5.19(c) and (d), the FEM model for the beam with ABH stiffeners also exhibits a good agreement with the experimental data in the lower frequency range. As the frequency increases, discrepancies between the FEM results and experimental data become more evident, particularly in the mid-frequency region where a shift in the resonance peaks can be observed. These differences may arise from the interaction between the viscoelastic layers and the ABH profile, which may introduce dynamic effects that are not fully accounted for in the current FEM model.

Overall, both FEM models are able to capture the primary dynamic characteristics of the beams with constrained viscoelastic damping layers. However, the minor discrepancies observed at higher frequencies suggest the need for further refinement of the FEM

models, particularly in accurately representing the complex damping mechanisms and interactions between the stiffeners and the viscoelastic layers at higher frequencies.

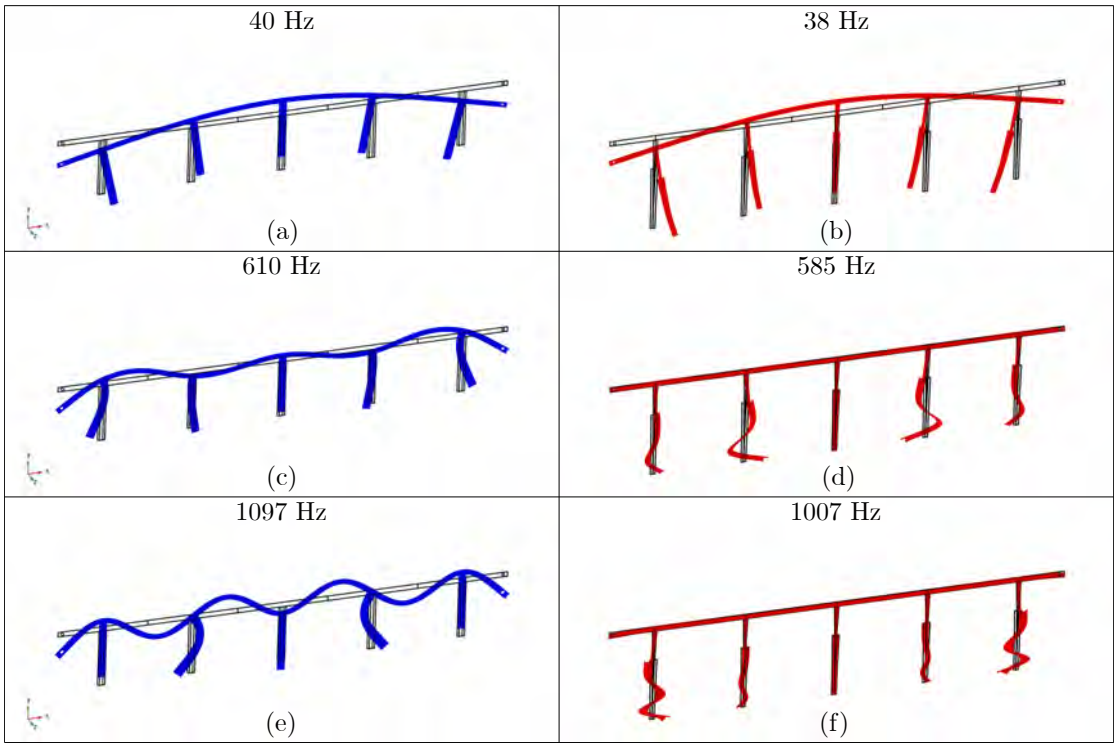

FIGURE 5.20: Mode shapes of the stiffened beam with rectangular stiffeners at (a) 40 Hz, (c) 610 Hz, and (e) 1097 Hz. Mode shapes of the stiffened beam with ABH stiffeners at (b) 38 Hz, (d) 585 Hz, and (f) 1007 Hz. Both stiffeners are considered to have CVLs.

The mode shapes presented in Fig. 5.20 compare the vibrational behaviour of beams stiffened with rectangular stiffeners and ABH stiffeners, both with CVLs. At lower frequencies, Figs. 5.20(a) and (b) (40 Hz and 38 Hz, respectively), both stiffened beams display relatively symmetric and uniform mode shapes, similar to the other cases (without damping layers and with VLs). The vibrational energy is distributed along the length of the beam, with no significant deformation localised in the stiffeners, as also observed by the same resonance peak present in the transmissibility response of both stiffened-beams as presented in Fig. 5.14.

As the frequency increases to the mid-range, Figs. 5.20(c) and (d) (610 Hz and 585 Hz, respectively), the distinction between the two configurations becomes more apparent. The ABH-stiffened beam concentrates the vibrational energy around the stiffener regions, which leads to improved attenuation by the CVLs as observed in Fig. 5.14. In contrast, the rectangular stiffeners exhibit a more uniform distribution of vibrational

energy along the beam without a localised deformation. This behaviour is reflected in the transmissibility results shown in Fig. 5.14. Similarly, in the high-frequency range, Figs. 5.20(e) and (f) (1097 Hz and 1007 Hz, respectively), the mode shapes of the ABH-stiffened beam demonstrate a clear concentration of energy at the stiffeners, whereas the rectangular-stiffened beam continues to exhibit distributed deformations across the beam and stiffeners. This is consistent with the results shown in Fig. 5.14, where it can be observed a lower transmissibility amplitude of the ABH-stiffened beam with CVLs.

5.4 Summary

This chapter initially presented the experimental analysis of two finite beams, one stiffened with conventional rectangular stiffeners and the other with ABH stiffeners. The ABH stiffeners were designed to match the area and moment of inertia at the contact point with the beam, ensuring that both stiffeners had the same mass and static stiffness as the rectangular stiffeners. The experiments were conducted to evaluate the effectiveness of ABH stiffeners in mitigating vibrations. Three configurations were analyzed: stiffeners without damping layers, with VLs, and with CVLs.

The experimental results showed that the addition of damping layers, particularly CVLs, significantly enhanced the mitigation of vibrations, with the ABH-stiffened beam exhibiting superior performance compared to the rectangular-stiffened beam. It was also observed that adding damping layers to the ABH stiffeners was very effective in reducing vibrations of the stiffened beam. The constrained layers improved energy dissipation by restricting the deformation of the viscoelastic material, leading to significant reductions in vibrational response.

Numerical simulations using the FEM in COMSOL Multiphysics™ were compared to the experimental findings. The simulations were in good agreement with the experimental data, particularly at low and mid frequencies, though some deviations were noted at higher frequencies. It was shown that at lower frequencies, both stiffened beams exhibit relatively symmetric and uniform mode shapes, consistent with the transmissibility results. At higher frequencies, the ABH-stiffened beam demonstrates its intended behaviour by concentrating vibrational energy at the tips of the stiffeners, highlighting the effectiveness of the ABH mechanism. This concentrated energy is dissipated

by the damping layers, as reflected in the transmissibility results. Overall, the study demonstrated that ABH stiffeners, particularly when combined with damping layers, offer significant advantages in vibration mitigation, providing a promising solution for vibration control in stiffened structures.

Chapter 6

Conclusions and Future Work

6.1 Conclusions

Theoretical and experimental studies on the prediction of vibroacoustic behaviour in periodically stiffened structures are of particular interest in a wide range of engineering applications, including aerospace, automotive, and marine industries. It has been reported in the literature that in these structures, BF waves are generated as a result of the interaction between flexural waves in the host structure and flexural/torsional waves in the stiffeners. These waves are a major source of unwanted noise and vibrations when the stiffened structure is subjected to external forces. Hence, a passive control method based on ABH was developed to manage the vibroacoustic behaviour of fluid-loaded stiffened plates. This was accomplished by integrating ABHs into the stiffeners and evaluating their impact on the propagation of BF waves.

In Chapter 3, an analytical formulation of NNI for an infinite, heavy fluid-loaded plate with periodic stiffeners was developed. This formulation was employed to identify the surface regions on the stiffened plate that contribute to the radiated sound power. The effects of stiffeners on both vibration and radiated sound were investigated, with the corresponding BF radiating frequencies identified. NNI maps revealed significant differences between stiffened and unstiffened plates under various excitations. Within the BF radiating bands, the intensity was broadly distributed across the plate, whereas outside these bands, it remained concentrated near the excitation point. Additionally, the vibrations responsible for far-field noise were found to propagate through the stiffeners,

resulting in greater radiated sound when excitation occurred between them. Structural damping was shown to effectively reduce the NNI distribution and radiated sound power at BF frequencies, though it had minimal impact outside these frequencies. This work demonstrated the effectiveness of NNI in identifying surface contributions to noise radiation and provided a computationally efficient tool for parametric analysis of stiffened panels.

In Chapter 4, a semi-analytical formulation for the vibroacoustic response of a 2D infinite fluid-loaded plate with ABH stiffeners was developed, utilising dynamic stiffnesses derived from FE modelling. This approach allowed for a detailed analysis of the vibroacoustic behaviour, identifying passbands and radiating passbands of BF waves. The study demonstrated that ABH stiffeners significantly mitigate the vibroacoustic response compared to conventional rectangular stiffeners, particularly above the first flexural natural frequency. Designed to match the surface area and moment of inertia of rectangular stiffeners, ABH stiffeners reduced radiated sound power over a broad frequency range, with a more pronounced attenuation effect on the mean quadratic velocity. These results highlight the advantages of ABH stiffeners for reducing noise in fluid-loaded plates.

Lastly, in Chapter 5, an experimental and numerical analysis was presented comparing two finite beams: one stiffened with conventional rectangular stiffeners and the other with ABH stiffeners, both designed to have the same mass and static stiffness. Three configurations were tested: stiffeners without damping layers, with VLs, and with CVLs. The results demonstrated that ABH stiffeners, particularly when combined with CVLs, presented a significantly lower vibrational response. It was shown that damping layers were more effective on ABH stiffeners, as they concentrated vibrational energy at the stiffener tips for dissipation. Numerical simulations supported the experimental findings, especially at low and mid frequencies. This study confirmed the vibration reduction capability caused by the replacement of rectangular stiffeners with ABH stiffeners, providing a promising solution for vibration mitigation in stiffened structures.

6.2 Future work

The work presented in this thesis focused on the vibroacoustic behaviour of stiffened structures, with particular attention to the control of vibration and propagation of BF

waves through the use of ABH stiffeners. An extension of this research could involve the development of more comprehensive vibroacoustic models tailored to real-world engineering applications. Four key areas of the system could be expanded upon to further advance the findings of this thesis:

1. Extension to a full 3D semi-analytical model

   Future research could focus on extending the semi-analytical model developed in Chapter 4 to a comprehensive 3D framework. In this extension, the contributions of the stiffeners would continue to be computed using the FEM, which would then be integrated with the analytical model of the 3D stiffened plate. This integration would significantly enhance the accuracy of the model in predicting real-world structural behaviour, particularly in engineering applications where complex interactions between the stiffeners and the base structure are prevalent.

   Additionally, future work could explore the development of a semi-analytical model for a finite plate, expanding the current infinite plate assumption. Such a model would allow for more accurate analysis of real-world structures with finite boundaries, providing insights into edge effects and other boundary condition influences. Furthermore, the inclusion of thick plate theory would extend the applicability of the model to structures where plate thickness cannot be neglected, particularly in cases where the thin plate assumption breaks down due to higher-order bending and shear deformations. Moreover, as proposed in Chapter 3, NNI maps could be obtained to study in detail how the plate radiates when the stiffeners have an ABH shape. This approach would allow for a comprehensive understanding of the radiation characteristics associated with the ABH stiffeners and provide valuable insights into their vibroacoustic behaviour in practical applications.

   Another important direction for future work would be the removal of the current assumption of symmetry in the stiffeners. By allowing for asymmetrical stiffener configurations, such as "L"-shaped profiles, the model could be adapted to more accurately reflect practical structural designs. This would provide a more robust and versatile analytical tool for predicting the vibrational and acoustic performance of stiffened plates under various boundary conditions. Such advancements are particularly relevant in industries where asymmetric stiffeners are commonplace, such

as aerospace and marine engineering. Overall, these developments would substantially improve the model's predictive capabilities and expand its applicability to a broader range of complex engineering structures.

2. Extension to stochastic excitation

   The model could be extended to account for stochastic excitation, such as that generated by a TBL or a diffuse acoustic field (DAF), instead of the current point force assumption. Stochastic excitations like TBL and DAF are commonly encountered in transportation systems, including aircraft, marine vessels, high-speed trains, and automobiles. These systems are often exposed to random, unpredictable excitations during operation, making it crucial for the model to reflect such realistic operating conditions. By shifting from point force excitation to stochastic excitation, the model would be better suited to capture the broad range of random pressure fluctuations and their effects on structural response. This extension would allow for more accurate predictions of the vibroacoustic behaviour, particularly under operational conditions where such excitations dominate. As a result, the model's applicability to real-world engineering scenarios, especially those involving transportation systems, would be significantly enhanced.

3. Extension to cylindrical shell structures

   A potential direction for future work involves extending the current model to cylindrical shell structures, which would broaden its applicability to various engineering systems, such as different aircraft fuselages and submarine hulls. To achieve this, the semi-analytical model could be transformed from the existing thin-plate formulation to a more appropriate shell theory, such as Flügge's shell model. This transition would allow for a more accurate representation of the structural mechanics relevant to cylindrical geometries commonly found in aerospace and marine applications. In addition, the periodic arrangement of stiffeners along the cylindrical shell should be explicitly considered in the extended model. Specifically, the stiffeners would be modelled as circumferential, or ring, stiffeners, and their effects on the dynamic and vibroacoustic response of the shell would be incorporated. Such improvements would significantly enhance the model's versatility and accuracy for real-world structural analysis.

4. Optimisation of the ABH stiffeners

   The use of optimisation algorithms could greatly enhance the design of ABH stiffeners for improved vibroacoustic mitigation. Key parameters, such as the shape, spacing, and material properties of the ABH stiffeners, could be optimised to minimise vibroacoustic response while preserving the necessary static stiffness of the structure. Different optimisation techniques, such as genetic algorithms or multi-objective optimisation frameworks, could be employed to achieve the vibroacoustic mitigation while maintaining the structural integrity. This approach would allow for the development of ABH stiffeners that effectively reduce vibrations and acoustic radiation while meeting the practical requirements of engineering applications. Furthermore, the optimisation framework could be extended to account for different types of excitations and boundary conditions, ensuring the robustness and versatility of the optimised designs across various operating environments.

5. Extension of the experiment and numerical model

   The experimentally validated FE models developed in Chapter 5, which accurately capture the structural dynamics including the mass loading effects of sensors, provide a robust foundation for future vibroacoustic predictions. A significant extension of the current work would be to leverage these validated structural models within a coupled fluid-structure interaction framework. By incorporating a surrounding fluid domain (air or water), potentially using coupled FE-FE or FE-BEM approaches, the acoustic radiation resulting from the stiffened plate vibrations could be predicted. This would allow for the quantification of the acoustic benefits, such as reductions in radiated sound power, changes in radiation efficiency achieved by substituting conventional stiffeners with the ABH-profiled designs under fluid-loaded conditions. Such analysis would directly address the practical implications of the observed vibration reductions, providing a more holistic assessment of the ABH stiffeners' vibroacoustic performance and bridging the gap between the structural analysis presented and the resulting acoustic signature.

Appendix A

Interactive plots of the 3D heavy fluid-loaded stiffened plate

A.1 Wavenumber spectrum of the plate velocity

This section contains an interactive figure showing the wavenumber spectrum of the plate velocity from 350 Hz to 850 Hz, considering the excitation on the stiffener. The wavenumber spectrum of the plate velocity with the excitation force on the stiffener is presented by the interactive Fig. A.1, showing the transition between the $\mathrm{BF}_{\mathrm{rad}}$ bands which are highlighted by the red border around the figure. The spectra considers a fixed color map amplitude range. The k_y passbands (i.e. case $\Delta(k_y^i) < \epsilon$ in Fig. 3.2) are highlighted on both sides on the y-axis in a white bar. The wavenumbers for the flexural and torsional motions of the stiffeners are presented by the horizontal white dashed and dashed-dot lines. The fluid-loaded plate natural flexural circle is shown by the white dotted line. It can be seen that for the frequencies inside the $\mathrm{BF}_{\mathrm{rad}}$ band there is a high amplitude inside the acoustic circle (represented by the solid white circle at the center of the spectrum).

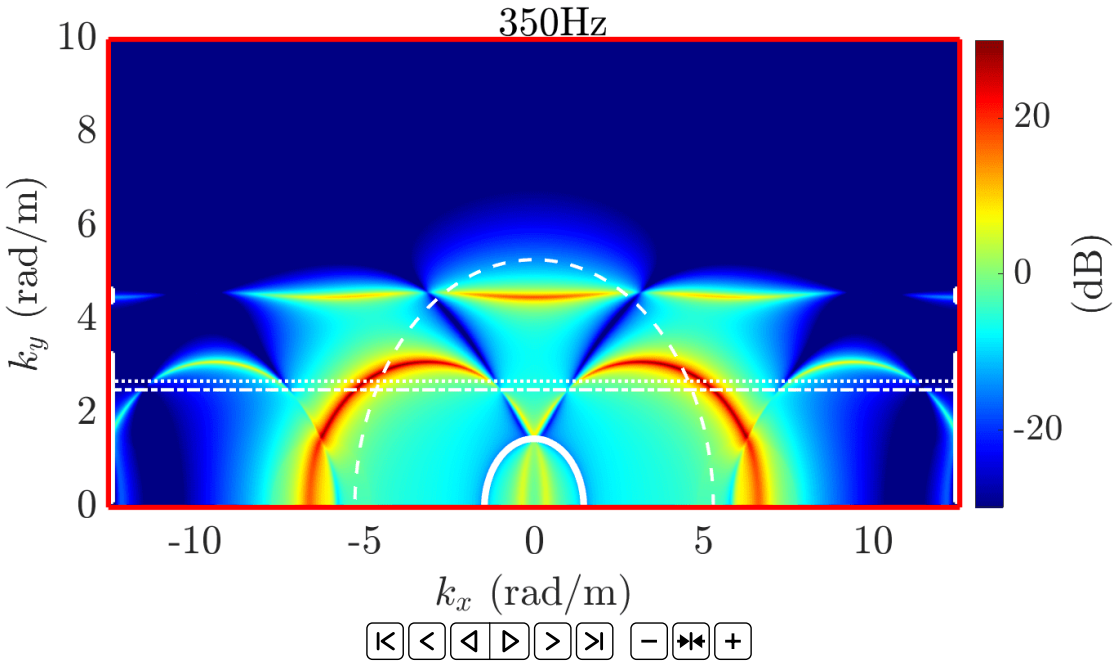

FIGURE A.1: Wavenumber spectrum of the plate velocity for frequency range from 350 Hz to 850 Hz, considering the excitation on the stiffener. Propagation zones are indicated by a white mark on the k_y-axis. Red square mark when the excitation frequency is inside the $\mathrm{BF}_{\mathrm{rad}}$ propagating band. (dB, ref 1 μm.s^{-1}).

A.2 Surface maps of particle velocity, acoustic pressure, active intensity and non-negative intensity

This section presents a direct comparison between the V, P, I_{act} and I^{N} for the same frequency range which comprises two passbands. Fig. A.2 shows the comparison between the four maps, highlighting the $\mathrm{BF}_{\mathrm{rad}}$ with a red square around the map. The interactive figure shows the pattern changes as the frequency increases, allowing to stop at specific frequencies to observe the maps with more attention. It can be seen that by looking at the velocity and pressure maps is not possible to locate the hot spots, the high amplitude over the entire surface makes difficult to locate the surface contribution to the velocity and pressure. The distinct behaviour of the NNI is noticed by focusing the transition from the $\mathrm{BF}_{\mathrm{rad}}$ bands to a non-radiating and again towards a $\mathrm{BF}_{\mathrm{rad}}$ band, with the I^{N} map showing the arc shape around the excitation source, and than following the stiffeners lines.

Similarly, Fig. A.3 shows the four maps for the case with excitation between stiffeners. With the interactive figure it can be seen that as the frequency increases the hot spot concentrates at the exact point of the force, and the pattern starts to change from

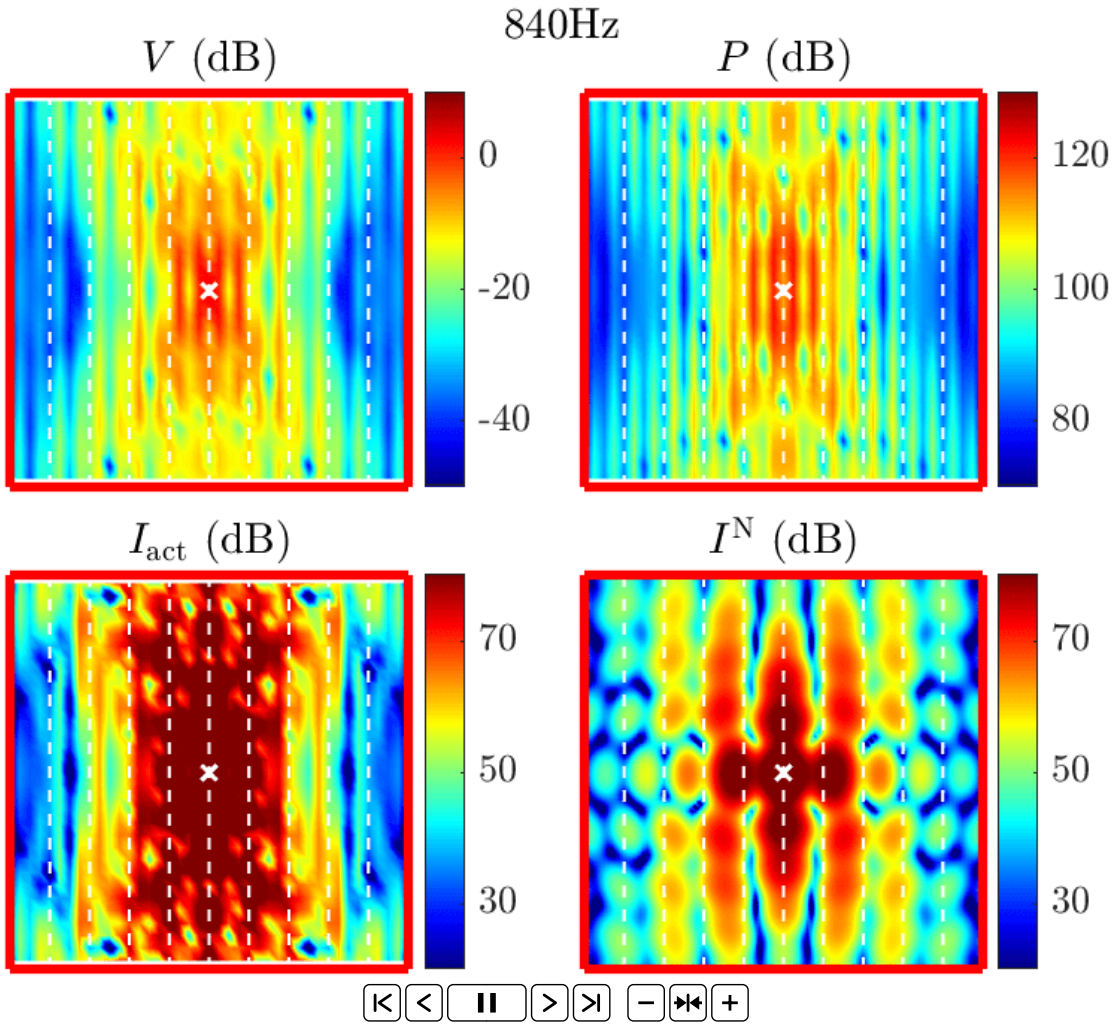

FIGURE A.2: Maps of V, P, I_{act} and I^{N} for 10 m $\times$10 m of the infinite stiffened structure excited by a point force on stiffener at $x_0 = 0$ m, for frequency range from 350 Hz to 850 Hz. Stiffener's lines and the point force position (x_0) are presented as white dashed lines and white x mark, respectively. Red square mark when the excitation frequency is inside the BF_{rad} band.

the circular shape when the frequency is inside the BF_{rad} band. The same pattern of the energy following the stiffener's lines that can be observed when the excitation is on stiffener, is not present when the excitation is between stiffeners in the analysed frequency range.

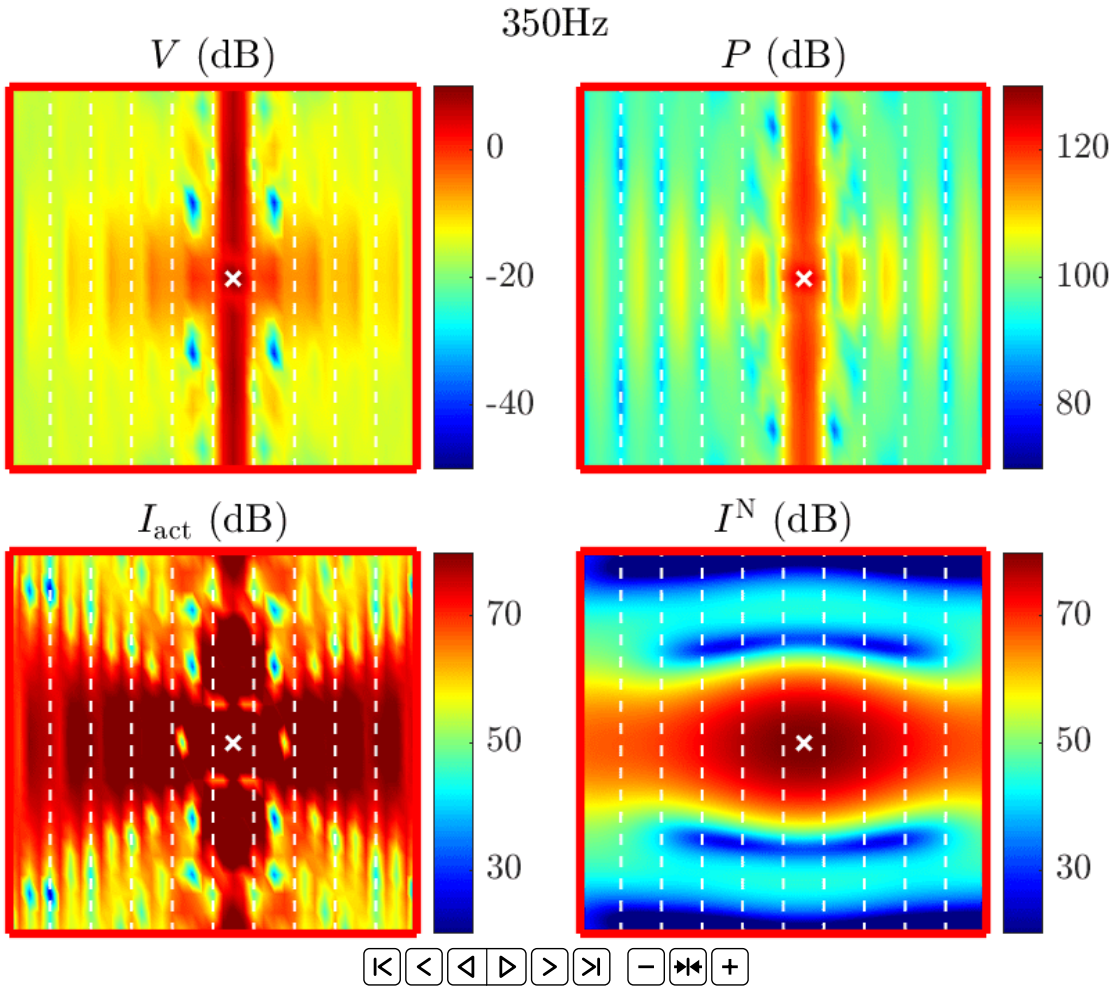

FIGURE A.3: Maps of V, P, I_{act} and I^{N} for 10 m $\times$10 m of the infinite stiffened structure excited by a point force between stiffeners, for frequency range from 350 Hz to 850 Hz. Stiffener's lines and the point force position (x_0) are presented as white dashed lines and white x mark, respectively. Red square mark when the excitation frequency is inside the BF_{rad} band.

A.3 Effect of the force position on the NNI

Fig. A.4 and A.5 shows the surface contribution in terms of NNI, and the vibroacoustic response in terms of sum of quadratic velocity, sound power and radiation efficiency, for frequencies 550 Hz and 750 Hz which are inside and outside of a $\mathrm{BF}_{\mathrm{rad}}$ band, respectively. The current x_0 position response is highlighted by a red mark in the AV^2, Π and $\log_{10}(\sigma)$ responses.

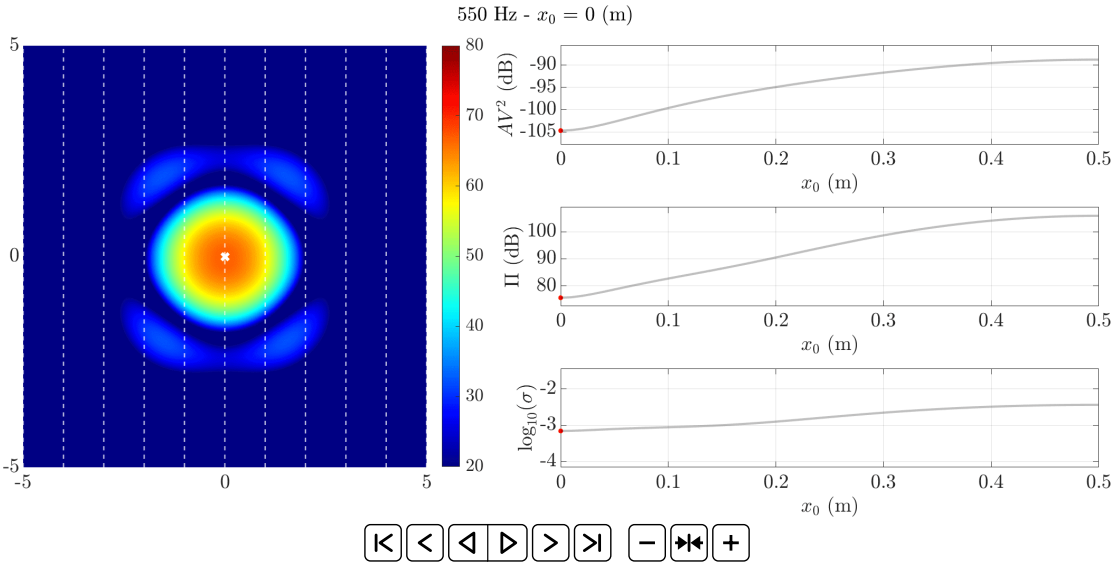

FIGURE A.4: Surface map of I^{N}, and vibroacoustic response from varying point force position in AV^2, Π and $\log_{10}(\sigma)$ for 550 Hz (outside a $\mathrm{BF}_{\mathrm{rad}}$ band). In the map, stiffener's lines and the point force position (x_0) are presented as white dashed lines and white x mark, respectively. Current response for given x_0 position is highlighted by a red mark.

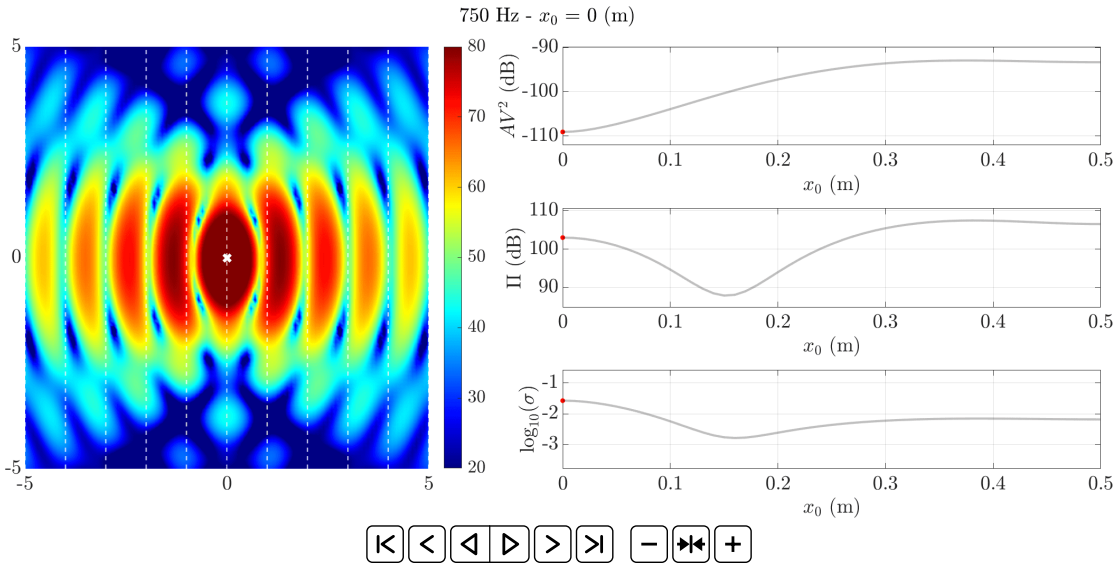

FIGURE A.5: Surface map of I^{N}, and vibroacoustic response from varying point force position in AV^2, Π and $\log_{10}(\sigma)$ for 750 Hz (in a $\mathrm{BF}_{\mathrm{rad}}$ band). In the map, stiffener's lines and the point force position (x_0) are presented as white dashed lines and white x mark, respectively. Current response for given x_0 position is highlighted by a red mark.

Appendix B

Bloch-Floquet propagating waves

Fig. B.1 illustrates the amplitude of the BF wavenumber as a function of frequency for the case in water, considering Fig. B.1(a) rectangular stiffeners and Fig. B.1(b) ABH stiffeners, both incorporating damping layers. The acoustic wavenumber is depicted by the blue line. The BF radiating frequency bands are highlighted by the blue-shaded areas for the rectangular-stiffened case and the red-shaded areas for the ABH-stiffened case. These BF radiating frequency bands correspond to frequencies where $k^{\mathrm{BF}} \leq k_{\mathrm{f}}$. It can be observed that not all frequencies produce propagative BF wavenumbers. For frequencies below 1500 Hz, propagating BF waves are present but do not radiate into the far field, as $k_{\mathrm{BF}} > k_{\mathrm{f}}$. Above this frequency, all propagating BF waves radiate, since $\pi/d \leq k_{\mathrm{f}}$.

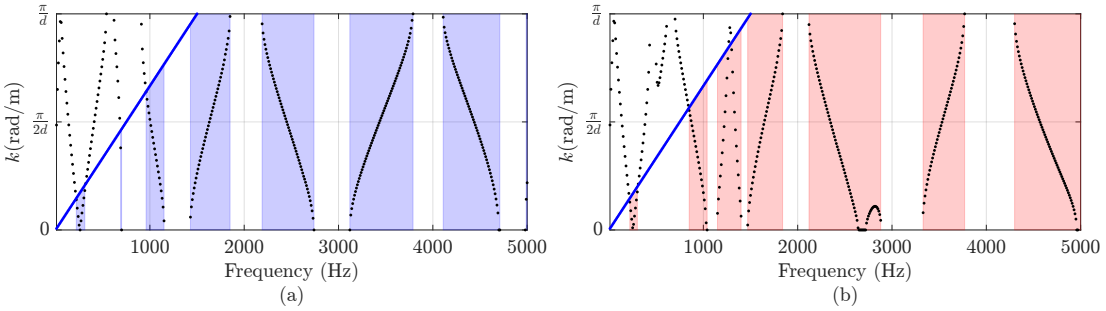

FIGURE B.1: Amplitude of the BF wavenumber k^{BF} in function of frequency (black dots), for the (a) rectangular-stiffened plate and (b) ABH-stiffened plate, both with damping layers and considering water as the fluid on the half-space Ω. Shaded areas are the BF radiating frequency bands corresponding to frequency such that $k^{\mathrm{BF}} \leq k_{\mathrm{f}}$, in which k_{f} is represented by the blue line.

References

[1] Autodesk Inc. Water jet cutting software. https://www.autodesk.com/solutions/water-jet-cutting-software, 2024. Accessed: 01-08-2024.

[2] Y. Bao, Z. Yao, Y. Zhang, X. Hu, X. Liu, Y. Shan, and T. He. Ultra-broadband gaps of a triple-gradient phononic acoustic black hole beam. *International Journal of Mechanical Sciences*, 265:108888, 2024.

[3] A. Baz. Active control of periodic structures. *Journal of Vibration and Acoustics*, 123(4):472–479, 2001.

[4] G. V. Borgiotti, A. Sarkissian, E. G. Williams, and L. Schuetz. Conformal generalized near-field acoustic holography for axisymmetric geometries. *The Journal of the Acoustical Society of America*, 88(1):199–209, 1990.

[5] E. Bowyer and V. V. Krylov. Experimental study of sound radiation by plates containing circular indentations of power-law profile. *Applied Acoustics*, 88:30–37, 2015.

[6] L. Brillouin. *Wave propagation in periodic structures: electric filters and crystal lattices*, volume 2. Dover publications, 1953.

[7] C. B. Burroughs. Acoustic radiation from fluid-loaded infinite circular cylinders with doubly periodic ring supports. *The Journal of the Acoustical Society of America*, 75(3):715–722, 1984.

[8] D. Chase. The character of the turbulent wall pressure spectrum at subconvective wavenumbers and a suggested comprehensive model. *Journal of Sound and Vibration*, 112(1):125–147, 1987.

[9] W. C. Chi, X. G. Sun, and Y. Q. Wang. Vibration control of piezoelectric beams with active constrained layer damping treatment using ladrc algorithm. In *Structures*, volume 62, page 106297. Elsevier, 2024.

[10] C. Claeys, E. Deckers, B. Pluymers, and W. Desmet. A lightweight vibro-acoustic metamaterial demonstrator: Numerical and experimental investigation. *Mechanical systems and signal processing*, 70:853–880, 2016.

[11] J. Deng, N. Gao, and X. Chen. Ultrawide attenuation bands in gradient metabeams with acoustic black hole pillars. *Thin-Walled Structures*, 184:110459, 2023.

[12] J. Deng, N. Gao, X. Chen, B. Han, and H. Ji. Evanescent waves in a metabeam attached with lossy acoustic black hole pillars. *Mechanical Systems and Signal Processing*, 191:110182, 2023.

[13] J. Deng, O. Guasch, L. Maxit, and L. Zheng. Reduction of bloch-floquet bending waves via annular acoustic black holes in periodically supported cylindrical shell structures. *Applied Acoustics*, 169:107424, 2020.

[14] L. H. Donnell. A new theory for the buckling of thin cylinders under axial compression and bending. *Transactions of the American Society of Mechanical Engineers*, 56(8):795–806, 1934.

[15] G. Eatwell and D. Butler. The response of a fluid-loaded, beam-stiffened plate. *Journal of Sound and Vibration*, 84(3):371–388, 1982.

[16] S. J. Elliott, P. Gardonio, T. C. Sors, and M. J. Brennan. Active vibroacoustic control with multiple local feedback loops. *The Journal of the Acoustical Society of America*, 111(2):908–915, 2002.

[17] S. J. Elliott and M. E. Johnson. Radiation modes and the active control of sound power. *The Journal of the Acoustical Society of America*, 94(4):2194–2204, 1993.

[18] F. Fahy. *Sound intensity*. CRC Press, 2017.

[19] E. Fernandez-Grande and F. Jacobsen. Conservation of power of the supersonic acoustic intensity. *The Journal of the acoustical society of America*, 136(2):461–465, 2014.

[20] E. Fernandez-Grande, F. Jacobsen, and Q. Leclere. Direct formulation of the supersonic acoustic intensity in space domain. *The journal of the acoustical society of America*, 131(1):186–193, 2012.

[21] V. Ferreira, R. Tenenbaum, F. Dias, and C. Corrêa Jr. Power operator dimensional reduction to obtain the useful intensity in rectangular plates with several boundary conditions. *Journal of Sound and Vibration*, 448:130–145, 2019.

[22] P. A. Feurtado and S. C. Conlon. Wavenumber transform analysis for acoustic black hole design. *The Journal of the Acoustical Society of America*, 140(1):718–727, 2016.

[23] A. Figueroa, M. Telenko Jr, L. Chen, and S. F. Wu. Determining structural damping and vibroacoustic characteristics of a non-symmetrical vibrating plate in free boundary conditions using the modified helmholtz equation least squares method. *Journal of Sound and Vibration*, 495:115903, 2021.

[24] S. P. Grace, H. M. Atassi, and W. K. Blake. Inverse aeroacoustic problem for a streamlined body. i-basic formulation. *AIAA Journal*, 34(11):2233–2240, 1996.

[25] P. Grootenhuis. The control of vibrations with viscoelastic materials. *Journal of Sound and Vibration*, 11(4):421–433, 1970.

[26] C. Hodges, J. Power, and J. Woodhouse. The low frequency vibration of a ribbed cylinder, part 2: Observations and interpretation. *Journal of Sound and Vibration*, 101(2):237–256, 1985.

[27] C. Hodges, J. Power, J. Woodhouse, et al. The low frequency vibration of a ribbed cylinder, part 1: Theory. *Journal of Sound and Vibration*, 101(2):219–235, 1985.

[28] K. Hook, J. Cheer, and S. Daley. A parametric study of an acoustic black hole on a beam. *The Journal of the Acoustical Society of America*, 145(6):3488–3498, 2019.

[29] H. Ji, Y. Liang, J. Qiu, L. Cheng, and Y. Wu. Enhancement of vibration based energy harvesting using compound acoustic black holes. *Mechanical Systems and Signal Processing*, 132:441–456, 2019.

[30] H. Ji, N. Wang, C. Zhang, X. Wang, L. Cheng, and J. Qiu. A vibration absorber based on two-dimensional acoustic black holes. *Journal of Sound and Vibration*, 500:116024, 2021.

[31] H. Ji, X. Zhao, N. Wang, W. Huang, J. Qiu, and L. Cheng. A circular eccentric vibration absorber with circumferentially graded acoustic black hole features. *Journal of Vibration and Acoustics*, 144(2):021014, 2022.

[32] F. Jiang, L. Li, W.-H. Liao, and D. Zhang. Vibration control of a rotating hub-plate with enhanced active constrained layer damping treatment. *Aerospace Science and Technology*, 118:107081, 2021.

[33] C. C. Junior and R. Tenenbaum. Useful intensity: A technique to identify radiating regions on arbitrarily shaped surfaces. *Journal of Sound and Vibration*, 332(6):1567–1584, 2013.

[34] M. Karimi, L. Maxit, V. Meyer, S. Marburg, and R. Kirby. Non-negative intensity for planar structures under stochastic excitation. *Journal of Sound and Vibration*, 488:115652, 2020.

[35] E. M. Kerwin Jr. Damping of flexural waves by a constrained viscoelastic layer. *The Journal of the Acoustical society of America*, 31(7):952–962, 1959.

[36] J. Kha, M. Karimi, L. Maxit, A. Skvortsov, and R. Kirby. An analytical approach for modelling the vibroacoustic behaviour of a heavy fluid-loaded plate near a free surface. *Journal of Sound and Vibration*, 538:117206, 2022.

[37] B. Khalfi and A. Ross. Transient response of a plate with partial constrained viscoelastic layer damping. *International Journal of Mechanical Sciences*, 68:304–312, 2013.

[38] B.-K. Kim and J.-G. Ih. On the reconstruction of the vibro-acoustic field over the surface enclosing an interior space using the boundary element method. *The Journal of the Acoustical Society of America*, 100(5):3003–3016, 1996.

[39] Y. Kim and P. Nelson. Optimal regularisation for acoustic source reconstruction by inverse methods. *Journal of Sound and Vibration*, 275(3-5):463–487, 2004.

[40] C. Kittel and P. McEuen. *Introduction to solid state physics*. John Wiley & Sons, 2018.

[41] V. Krylov and A. Shuvalov. Propagation of lo-calised flexural vibrations along plate edges described by a power law. *Proceed-ings of the Institute of Acoustics*, 22(2):263–270, 2000.

[42] V. Krylov and F. Tilman. Acoustic 'black holes' for flexural waves as effective vibration dampers. *Journal of sound and vibration*, 274(3-5):605–619, 2004.

[43] V. V. Krylov. New type of vibration dampers utilising the effect of acoustic'black holes'. *Acta Acustica united with Acustica*, 90(5):830–837, 2004.

[44] V. V. Krylov and R. Winward. Experimental investigation of the acoustic black hole effect for flexural waves in tapered plates. *Journal of Sound and Vibration*, 300(1-2):43–49, 2007.

[45] J.-H. Lee and J. Kim. Analysis of sound transmission through periodically stiffened panels by space-harmonic expansion method. *Journal of Sound and Vibration*, 251(2):349–366, Mar. 2002.

[46] H. Li, O. Doaré, C. Touzé, A. Pelat, and F. Gautier. Energy harvesting efficiency of unimorph piezoelectric acoustic black hole cantilever shunted by resistive and inductive circuits. *International Journal of Solids and Structures*, 238:111409, 2022.

[47] H. Li, P. O'donoughue, F. Masson, A. Pelat, F. Gautier, and C. Touzé. Broadband shock vibration absorber based on vibro-impacts and acoustic black hole effect. *International Journal of Non-Linear Mechanics*, 159:104620, 2024.

[48] H. Li, C. Touzé, F. Gautier, and A. Pelat. Linear and nonlinear dynamics of a plate with acoustic black hole, geometric and contact nonlinearity for vibration mitigation. *Journal of Sound and Vibration*, 508:116206, 2021.

[49] M. Li, J. Deng, L. Zheng, and S. Xiang. Vibration mitigation via integrated acoustic black holes. *Applied Acoustics*, 198:109001, 2022.

[50] X. Li and Q. Ding. Sound radiation of a beam with a wedge-shaped edge embedding acoustic black hole feature. *Journal of Sound and Vibration*, 439:287–299, 2019.

[51] D. Liu, Z. Havránek, S. Marburg, H. Peters, and N. Kessissoglou. Non-negative intensity and back-calculated non-negative intensity for analysis of directional structure-borne sound. *The Journal of the Acoustical Society of America*, 142(1):117–123, 2017.

[52] D. Liu, S. Marburg, C. Geweth, and N. Kessissoglou. Non-negative intensity for structures with inhomogeneous damping. *Journal of Theoretical and Computational Acoustics*, 27(01):1850050, 2019.

[53] D. Liu, H. Peters, S. Marburg, and N. Kessissoglou. Supersonic intensity and non-negative intensity for prediction of radiated sound. *The journal of the acoustical society of America*, 139(5):2797–2806, 2016.

[54] D. Liu, H. Peters, S. Marburg, and N. Kessissoglou. Surface contributions to scattered sound power using non-negative intensity. *The Journal of the Acoustical Society of America*, 140(2):1206–1217, 2016.

[55] G. Liu, X. Peng, K. Lam, and J. Tani. Vibration control simulation of laminated composite plates with integrated piezoelectrics. *Journal of Sound and Vibration*, 220(5):827–846, 1999.

[56] P. Liu, H. Huang, X. Wang, Q. Tang, X. Qi, S. Su, Z. Xiang, and J. Hu. Acoustic black hole profiles for high-performance ultrasonic tweezers. *Mechanical Systems and Signal Processing*, 188:109991, 2023.

[57] L. Ma and L. Cheng. Sound radiation and transonic boundaries of a plate with an acoustic black hole. *The Journal of the Acoustical Society of America*, 145(1):164–172, 2019.

[58] L. Ma and L. Cheng. Numerical and experimental benchmark solutions on vibration and sound radiation of an acoustic black hole plate. *Applied Acoustics*, 163:107223, 2020.

[59] B. Mace. Periodically stiffened fluid-loaded plates, I: Response to convected harmonic pressure and free wave propagation. *Journal of Sound and Vibration*, 73(4):473–486, 1980.

[60] B. Mace. Periodically stiffened fluid-loaded plates, II: response to line and point forces. *Journal of sound and Vibration*, 73(4):487–504, 1980.

[61] B. Mace. Sound radiation from a plate reinforced by two sets of parallel stiffeners. *Journal of Sound and Vibration*, 71(3):435–441, 1980.

[62] M. B. S. Magalhães and R. A. Tenenbaum. Supersonic acoustic intensity for arbitrarily shaped sources. *Acta acustica united with acustica*, 92(2):189–201, 2006.

[63] S. Marburg, E. Lösche, H. Peters, and N. Kessissoglou. Surface contributions to radiated sound power. *The journal of the acoustical society of America*, 133(6):3700–3705, 2013.

[64] D. Martins, M. Karimi, and L. Maxit. Semi-analytical formulation to predict the vibroacoustic response of a fluid-loaded plate with abh stiffeners. *Thin-Walled Structures*, page 112539, 2024.

[65] D. Martins, M. Karimi, L. Maxit, and R. Kirby. Non-negative intensity for a heavy fluid-loaded stiffened plate. *Journal of Sound and Vibration*, 566:117891, 2023.

[66] L. Maxit. Wavenumber space and physical space responses of a periodically ribbed plate to a point drive: A discrete approach. *Applied acoustics*, 70(4):563–578, 2009.

[67] L. Maxit. Scattering model of a cylindrical shell with internal axisymmetric frames by using the circumferential admittance approach. *Applied Acoustics*, 80:10–22, 2014.

[68] L. Maxit and V. Denis. Prediction of flow induced sound and vibration of periodically stiffened plates. *The Journal of the Acoustical Society of America*, 133(1):146–160, 2013.

[69] L. Maxit and J.-M. Ginoux. Prediction of the vibro-acoustic behavior of a submerged shell non periodically stiffened by internal frames. *The Journal of the Acoustical Society of America*, 128(1):137–151, 2010.

[70] J. D. Maynard, E. G. Williams, and Y. Lee. Nearfield acoustic holography: I. theory of generalized holography and the development of nah. *The Journal of the Acoustical Society of America*, 78(4):1395–1413, 1985.

[71] D. Mead. The effect of a damping compound on jet-efflux excited vibrations: An article in two parts presenting theory and results of experimental investigation part i the structural damping due to the compound. *Aircraft Engineering and Aerospace Technology*, 32(3):64–72, 1960.

[72] D. Mead. Wave propagation in continuous periodic structures: research contributions from southampton, 1964–1995. *Journal of Sound and Vibration*, 190(3):495–524, 1996.

[73] D. Mead and N. Bardell. Free vibration of a thin cylindrical shell with periodic circumferential stiffeners. *Journal of Sound and Vibration*, 115(3):499–520, 1987.

[74] D. Mead and S. Markus. The forced vibration of a three-layer, damped sandwich beam with arbitrary boundary conditions. *Journal of sound and vibration*, 10(2):163–175, 1969.

[75] D. Mead and K. Pujara. Space-harmonic analysis of periodically supported beams: response to convected random loading. *Journal of Sound and Vibration*, 14(4):525–541, 1971.

[76] D. J. Mead. Free wave propagation in periodically supported, infinite beams. *Journal of Sound and Vibration*, 11(2):181–197, 1970.

[77] D. J. Mead. Plates with regular stiffening in acoustic media: vibration and radiation. *The Journal of the Acoustical Society of America*, 88(1):391–401, 1990.

[78] T. Mentel. Viscoelastic boundary damping of beams and plates. *Journal of Applied Mechanics*, 31(1):61, 1964.

[79] V. Meyer, L. Maxit, J.-L. Guyader, and T. Leissing. Prediction of the vibroacoustic behavior of a submerged shell with non-axisymmetric internal substructures by a condensed transfer function method. *Journal of Sound and Vibration*, 360:260–276, 2016.

[80] M. Mironov. Propagation of a flexural wave in a plate whose thickness decreases smoothly to zero in a finite interval. *Sov. Phys. Acoust*, 34(3):318–319, 1988.

[81] D. Moore and W. Geyer. A review of hysteresis theories for elastomers. *Wear*, 30(1):1–34, 1974.

[82] A. Mukherjee, S. Joshi, and A. Ganguli. Active vibration control of piezolaminated stiffened plates. *Composite structures*, 55(4):435–443, 2002.

[83] V. Mukhopadhyay. Hybrid-wing-body pressurized fuselage modeling, analysis and design for weight reduction. In *53rd AIAA/ASME/ASCE/AHS/ASC Structures,*

Structural Dynamics and Materials Conference 20th AIAA/ASME/AHS Adaptive Structures Conference 14th AIAA, page 1999, 2012.

[84] A. Okazaki, A. Tatemichi, and S. Mirza. Damping properties of two-layered cylindrical shells with an unconstrained viscoelastic layer. *Journal of sound and vibration*, 176(2):145–161, 1994.

[85] OMAX Corporation. Omax 55100 precision jetmachining center. https://www.omax.com/en/us/omax-waterjet/55100, 2024. Accessed: 01-08-2024.

[86] S. Park, J. Y. Lee, and W. Jeon. Vibration damping of plates using waveguide absorbers based on spiral acoustic black holes. *Journal of Sound and Vibration*, 521:116685, 2022.

[87] A. Pelat, F. Gautier, S. C. Conlon, and F. Semperlotti. The acoustic black hole: A review of theory and applications. *Journal of Sound and Vibration*, 476:115316, 2020.

[88] M. K. Philen and K. Wang. Active stiffeners for vibration control of a circular plate structure: Analytical and experimental investigations. *Journal of Vibration and Acoustics*, 2005.

[89] R. Plunkett and C. Lee. Length optimization for constrained viscoelastic layer damping. *The Journal of the Acoustical Society of America*, 48(1B):150–161, 1970.

[90] Y. Qu, J. Su, H. Hua, and G. Meng. Structural vibration and acoustic radiation of coupled propeller-shafting and submarine hull system due to propeller forces. *Journal of Sound and Vibration*, 401:76–93, 2017.

[91] M. Rumerman. Vibration and wave propagation in ribbed plates. *The journal of the acoustical society of America*, 57(2):370–373, 1975.

[92] K. Saijyou and S. Yoshikawa. Reduction methods of the reconstruction error for large-scale implementation of near-field acoustical holography. *The Journal of the Acoustical Society of America*, 110(4):2007–2023, 2001.

[93] A. Sarkissian. Extension of measurement surface in near-field acoustic holography. *The Journal of the Acoustical Society of America*, 115(4):1593–1596, 2004.

[94] A. Sarkissian. Method of superposition applied to patch near-field acoustic holography. *The Journal of the Acoustical Society of America*, 118(2):671–678, 2005.

[95] Y. Tong, J. Fan, B. Wang, and W. Tang. Vibroacoustic behavior of an infinitely long cylindrical shell with periodic internal lengthwise ribs. *The Journal of the Acoustical Society of America*, 144(3):1528–1538, 2018.

[96] M. Tran-Van-Nhieu, G. Maze, and D. Décultot. Approximate solutions to acoustic scattering from a ribbed finite plate. *The Journal of the Acoustical Society of America*, 141(5):3091–3100, 2017.

[97] M. A. Trindade, A. Benjeddou, and R. Ohayon. Modeling of frequency-dependent viscoelastic materials for active-passive vibration damping. *J. Vib. Acoust.*, 122(2):169–174, 2000.

[98] N. P. Valdivia. Improved integral formulae for supersonic reconstruction of the acoustic field. *Inverse Problems in Science and Engineering*, 26(6):898–924, 2018.

[99] N. P. Valdivia. Integral formulas for supersonic reconstruction of the acoustic field. *Inverse Problems in Science and Engineering*, 26(3):376–397, 2018.

[100] N. P. Valdivia and E. G. Williams. Study of the comparison of the methods of equivalent sources and boundary element methods for near-field acoustic holography. *The Journal of the Acoustical Society of America*, 120(6):3694–3705, 2006.

[101] N. P. Valdivia, E. G. Williams, and P. C. Herdic. Equivalent sources method for supersonic intensity of arbitrarily shaped geometries. *Journal of Sound and Vibration*, 347:46–62, 2015.

[102] W. Veronesi and J. Maynard. Digital holographic reconstruction of sources with arbitrarily shaped surfaces. *The Journal of the Acoustical Society of America*, 85(2):588–598, 1989.

[103] Z. Wan, X. Zhu, T. Li, and J. Fu. A method for improving wave suppression ability of acoustic black hole plate in low-frequency range. *Thin-Walled Structures*, 182:110327, 2023.

[104] H. Wen, J. Jiang, H. Huang, J. Guo, and L. Ye. Acoustic characteristics of composite structures with 2d acoustic black holes and stiffened plates. *Applied Acoustics*, 216:109805, 2024.

[105] D. R. Wilkes, H. Peters, P. Croaker, S. Marburg, A. J. Duncan, and N. Kessissoglou. Non-negative intensity for coupled fluid–structure interaction problems using the fast multipole method. *The Journal of the Acoustical Society of America*, 141(6):4278–4288, 2017.

[106] E. G. Williams. Supersonic acoustic intensity. *The journal of the acoustical society of America*, 97(1):121–127, 1995.

[107] E. G. Williams. Supersonic acoustic intensity on planar sources. *The Journal of the Acoustical Society of America*, 104(5):2845–2850, 1998.

[108] E. G. Williams. *Fourier acoustics: sound radiation and nearfield acoustical holography*. Academic press, 1999.

[109] E. G. Williams. Regularization methods for near-field acoustical holography. *The Journal of the Acoustical Society of America*, 110(4):1976–1988, 2001.

[110] E. G. Williams. Convolution formulations for non-negative intensity. *The journal of the acoustical society of America*, 134(2):1055–1066, 2013.

[111] E. G. Williams, H. D. Dardy, and K. B. Washburn. Generalized nearfield acoustical holography for cylindrical geometry: Theory and experiment. *The Journal of the Acoustical Society of America*, 81(2):389–407, 1987.

[112] E. G. Williams, B. H. Houston, P. C. Herdic, S. Raveendra, and B. Gardner. Interior near-field acoustical holography in flight. *The Journal of the Acoustical Society of America*, 108(4):1451–1463, 2000.

[113] E. G. Williams and J. D. Maynard. Holographic imaging without the wavelength resolution limit. *Physical review letters*, 45(7):554, 1980.

[114] E. G. Williams, J. D. Maynard, and E. Skudrzyk. Sound source reconstructions using a microphone array. *The Journal of the Acoustical Society of America*, 68(1):340–344, 1980.

[115] Y. Xiao, W. Shen, H. Zhu, and Y. Du. An acoustic black hole absorber for rail vibration suppression: Simulation and full-scale experiment. *Engineering Structures*, 304:117647, 2024.

[116] J. Yan, T. Li, J. Liu, and X. Zhu. Space harmonic analysis of sound radiation from a submerged periodic ring-stiffened cylindrical shell. *Applied acoustics*, 67(8):743–755, 2006.

[117] J. Yan, T. Li, T. Liu, and J. Liu. Characteristics of the vibrational power flow propagation in a submerged periodic ring-stiffened cylindrical shell. *Applied acoustics*, 67(6):550–569, 2006.

[118] B. Yao, Y. Zhang, Q. Zhou, B. He, G. Wang, and X. Rui. Vibration isolator using graded reinforced double-leaf acoustic black holes-theory and experiment. *Journal of Sound and Vibration*, 570:118003, 2024.

[119] S. Zhang, Q. Cheng, Y. Ma, and Z. Deng. A symplectic analytical wave propagation model for forced vibration of thin plate with acoustic black hole indentation. *Thin-Walled Structures*, 195:111339, 2024.

[120] L. Zhao and F. Semperlotti. Embedded acoustic black holes for semi-passive broadband vibration attenuation in thin-walled structures. *Journal of Sound and Vibration*, 388:42–52, 2017.

[121] Y. Zhen, T. Gu, and Y. Tang. Aeroelastic analysis and active control of one-dimensional acoustic black hole structures in supersonic airflow. *Engineering Analysis with Boundary Elements*, 147:292–301, 2023.

[122] T. Zhou and L. Cheng. A resonant beam damper tailored with acoustic black hole features for broadband vibration reduction. *Journal of Sound and Vibration*, 430:174–184, 2018.

[123] X. Zhou. Vibration and stability of ring-stiffened thin-walled cylindrical shells conveying fluid. *Acta mechanica solida sinica*, 25(2):168–176, 2012.

[124] X. Zhou, D. Yu, X. Shao, S. Wang, and Y. Tian. Asymptotic analysis on flexural dynamic characteristics for a sandwich plate with periodically perforated viscoelastic damping material core. *Composite Structures*, 119:487–504, 2015.

[125] X. Zhou, D. Yu, X. Shao, S. Zhang, and S. Wang. Research and applications of viscoelastic vibration damping materials: A review. *Composite Structures*, 136:460–480, 2016.